PUBLICATIONS OF
THE UNIVERSITY OF EASTERN FINLAND

Dissertations in
Health Sciences

KARTHIK SAMPATH KUMAR CHARY

Advanced MRI approaches for characterization of tissue microstructural changes in experimental traumatic brain injury

ADVANCED MRI APPROACHES FOR CHARACTERIZATION OF TISSUE MICROSTRUCTURAL CHANGES IN EXPERIMENTAL TRAUMATIC BRAIN INJURY

Karthik Sampath Kumar Chary

ADVANCED MRI APPROACHES FOR CHARACTERIZATION OF TISSUE MICROSTRUCTURAL CHANGES IN EXPERIMENTAL TRAUMATIC BRAIN INJURY

To be presented by permission of the Faculty of Health Sciences,
University of Eastern Finland for public examination, on January 13th,
2023, at 12 o'clock

Publications of the University of Eastern Finland
Dissertations in Health Sciences
No 721

A.I. Virtanen Institute for Molecular Sciences
University of Eastern Finland, Kuopio
2023

Series Editors
Professor Tomi Laitinen, M.D., Ph.D.
Institute of Clinical Medicine, Clinical Physiology and Nuclear Medicine
Faculty of Health Sciences

Professor Ville Leinonen, M.D., Ph.D.
Institute of Clinical Medicine, Neurosurgery
Faculty of Health Sciences

Professor Tarja Malm, Ph.D.
A.I. Virtanen Institute for Molecular Sciences
Faculty of Health Sciences

Lecturer Veli-Pekka Ranta, Ph.D.
School of Pharmacy
Faculty of Health Sciences

Lecturer Tarja Välimäki, Ph.D.
Department of Nursing Science
Faculty of Health Sciences

PunaMusta Oy
Joensuu, 2022
Distributor: University of Eastern Finland
Kuopio Campus Library

ISBN: 978-952-61-4738-3 (print/nid.)
ISBN: 978-952-61-4739-0 (PDF)
ISSNL: 1798-5706
ISSN: 1798-5706
ISSN: 1798-5714 (PDF)

Author's address: A.I. Virtanen Institute for Molecular Sciences
University of Eastern Finland
KUOPIO
FINLAND

Doctoral programme: Doctoral programme in Molecular Medicine

Supervisors: Docent Alejandra Sierra López, Ph.D.
A.I. Virtanen Institute for Molecular Sciences
University of Eastern Finland
KUOPIO
FINLAND

Professor Olli Gröhn, Ph.D.
A.I. Virtanen Institute for Molecular Sciences
University of Eastern Finland
KUOPIO
FINLAND

Reviewers: Assistant Professor Ferdinand Schweser, Ph.D.
Department of Neurology, Radiology, and
Biomedical engineering
University at Buffalo, SUNY
BUFFALO
USA

Professor Elizabeth Hutchinson, Ph.D.
Department of Biomedical Engineering
University of Arizona
TUCSON
USA

Opponent: Associate Professor Tim Dyrby, Ph.D.
Department of Applied Mathematics and Computer Science
Technical University of Denmark
COPENHAGEN
DENMARK

Chary, Karthik Sampath Kumar
Advanced MRI approaches for characterization of tissue microstructural changes in experimental traumatic brain injury
Kuopio: University of Eastern Finland
Publications of the University of Eastern Finland
Dissertations in Health Sciences 721. 2023, 129 p.
ISBN: 978-952-61-4738-3 (print)
ISSNL: 1798-5706
ISSN: 1798-5706
ISBN: 978-952-61-4739-0 (PDF)
ISSN: 1798-5714 (PDF)

ABSTRACT

Traumatic brain injury (TBI) is a major cause of disability, morbidity, and death worldwide. The primary lesion from the initial injury following brain injury leads to a cascade of subtle secondary injury mechanisms. Currently used quantitative MRI approaches either lack sensitivity or specificity to detect the varying pathological features associated with these secondary tissue changes. The general aim of this thesis was to explore the potential of advanced quantitative MRI approaches for an improved characterization of the secondary tissue damage at the sub-acute and chronic stages using an experimental traumatic brain injury (TBI) model.

At the chronic phase post-severe TBI (study **I**), susceptibility variations in the damaged tissues were associated with myelin loss, iron deposition and calcifications, and also gliosis. Overall, quantitative susceptibility mapping (QSM) demonstrated more sensitivity to secondary damage-induced changes in regions rostral to the lesion site as compared to R_2*. Nonetheless, QSM and R_2* in combination provided complimentary information in unravelling tissue alterations resulting from iron presence, demyelination or calcifications.

When investigating the sub-acute phase post-mild injury (study **II**), whole-brain group analysis revealed higher-order diffusion modelling tools

such as fixel-based analysis (FBA) to be more sensitive in WM, while neurite orientation dispersion and density imaging (NODDI) was only sensitive to damage in areas close to the primary lesion. Diffusion tensor imaging (DTI) detected more changes in GM. Overall, changes detected in dMRI measures were related with axonal damage and gliosis, and showed good corroboration with quantitative histology measures in specific brain areas.

When assessing alterations in tissue microstructural complexity, at the chronic phase after severe TBI (study **III**), single-shell 3-tissue constrained spherical deconvolution (SS3T-CSD) and DTI measures exhibited sensitvity to changes in both WM and GM regions of the brain. Additionally, distinct variations in the diffusion signal profiles were revealed by the 3-tissue signal fractions in the damaged brain. Track-weighted imaging (TWI) measures detected morphological changes in the thalamocortical tract rostral to the primary lesion demonstrating the extent of tissue damage. Changes in the dMRI measures were attributed to axonal loss, and extensive gliosis.

Overall, the studies in this thesis facilitate a more comprehensive and precise understanding of tissue changes associated with the complex pathophysiology in a mildly- and severely injured brain. Together, these studies also disseminate the effectiveness and limitations of these quantitative MRI approaches in their sensitivity to detect secondary tissue mechanisms after TBI. This can potentially lead to future work towards an improved understanding of TBI-related pathological changes.

Keywords: 3-tissue signal fractions, Axonal damage, Calcifications, Constrained spherical deconvolution, dMRI, Dipole inversion, Fiber density, FODs, Gliosis, HARDI, Hemosiderin, Histology, Iron, Lateral fluid percussion injury, Microbleeds, Microstructural changes, Microstructural complexity, NODDI, Projection onto dipole fields, Quantitative susceptibility mapping, R_2*, SS3T-CSD, Tikhonov, Traumatic brain injury

Chary, Karthik Sampath Kumar
Kehittyneet MRI-lähestymistavat kudosten mikrorakenteen muutosten karakterisointiin kokeellisessa traumaattisessa aivovauriossa
Kuopio: Itä-Suomen yliopisto
Publications of the University of Eastern Finland
Dissertations in Health Sciences 721. 2023, 129 s.
ISBN: 978-952-61-4738-3 (nid.)
ISSNL: 1798-5706
ISSN: 1798-5706
ISBN: 978-952-61-4739-0 (PDF)
ISSN: 1798-5714 (PDF)

TIIVISTELMÄ

Traumaattinen aivovaurio (TBI) on merkittävä vamman, sairastuvuuden ja kuoleman aiheuttaja maailmanlaajuisesti. Aivovamman jälkeisen alkuperäisen vamman aiheuttama primaarinen vaurio johtaa hienovaraisten toissijaisten vauriomekanismien sarjaan. Nykyisin käytetyt kvantitatiiviset MRI-lähestymistavat joko eivät ole herkkiä tai spesifisiä havaitsemaan näihin sekundäärisiin kudosmuutoksiin liittyviä erilaisia patologisia piirteitä. Tämän opinnäytetyön yleisenä tavoitteena oli tutkia edistyneiden kvantitatiivisten MRI-lähestymistapojen mahdollisuuksia subakuutin ja kroonisen vaiheen sekundaaristen kudosvaurioiden karakterisoinnissa kokeellisen traumaattisen aivovaurion (TBI) mallin avulla.

Vaikean TBI:n jälkeisessä kroonisessa vaiheessa (tutkimus **I**) herkkyysvaihtelut vaurioituneissa kudoksissa liittyivät myeliinin menetykseen, raudan kertymiseen ja kalkkeutumiseen sekä glioosiin. Kaiken kaikkiaan kvantitatiivinen herkkyyskartoitus (QSM) osoitti enemmän herkkyyttä sekundaaristen vaurioiden aiheuttamille muutoksille leesiokohdan rostraalisilla alueilla kuin R_2*. Siitä huolimatta QSM ja R_2* yhdessä tarjosivat täydentävää tietoa raudan esiintymisestä,

demyelinaatiosta tai kalkkeutumisesta johtuvien kudosmuutosten selvittämisessä.

Kun tutkittiin subakuuttia vaihetta lievän vamman jälkeistä vaihetta (tutkimus **II**), kokoaivoryhmäanalyysi paljasti korkeamman asteen diffuusiomallinnustyökalut, kuten fikselipohjaisen analyysin (FBA), olevan herkempiä WM:ssä, kun taas neuriittien orientaatiodispersio ja tiheys kuvantaminen (NODDI) oli herkkä vaurioille vain primäärivaurion lähellä olevilla alueilla. Diffuusiotensorikuvaus (DTI) havaitsi enemmän muutoksia GM:ssä. Kaiken kaikkiaan dMRI-mittauksissa havaitut muutokset liittyivät aksonivaurioihin ja glioosiin, ja ne osoittivat hyvää vahvistusta kvantitatiivisten histologisten mittausten kanssa tietyillä aivoalueilla.

Arvioitaessa muutoksia kudosten mikrorakenteen monimutkaisuus, kroonisessa vaiheessa vaikean TBI:n jälkeen (tutkimus **III**), yksikuorinen 3-kudoksinen sidottu pallomainen dekonvoluutio (SS3T-CSD) ja DTI-mittaukset osoittivat herkkyyttä muutoksille sekä aivojen WM- että GM-alueilla. Lisäksi vaurioituneiden aivojen kolmen kudoksen signaalifraktiot paljastivat eroja diffuusiosignaaliprofiileissa. Track-weighted imaging (TWI) mittaa havaittuja morfologisia muutoksia talamokortikaalisessa kanavassa primaariseen leesoon nähden, mikä osoittaa kudosvaurion laajuuden. Muutokset dMRI-mittauksissa johtuivat aksonien katoamisesta ja laajasta glioosista.

Kaiken kaikkiaan tämän opinnäytetyön tutkimukset mahdollistavat kattavamman ja tarkemman ymmärryksen monimutkaiseen patofysiologiaan liittyvistä kudosmuutoksista lievästi ja vakavasti loukkaantuneissa aivoissa. Yhdessä nämä tutkimukset levittävät myös näiden kvantitatiivisten MRI-lähestymistapojen tehokkuutta ja rajoituksia niiden herkkyydessä havaita sekundäärisiä kudosmekanismeja TBI:n jälkeen. Tämä voi mahdollisesti johtaa tulevaan työhön TBI:hen liittyvien patologisten muutosten ymmärtämiseksi paremmin.

Avainsanat: 3-kudoksen signaalifraktiot, aksonivauriot, kalkkeutumat, rajoitettu pallomainen dekonvoluutio, dMRI, dipoliinversio, kuitutiheys, FOD:t, glioosi, HARDI, hemosideriini, histologia, rauta, lateraalinen nesteen

iskuvamma, mikroverenvuodot, mikrorakenteen muutokset, NODDI, mikrorakenteen muutokset, Projektio dipolikenttiin, kvantitatiivinen herkkyyskartoitus, R_2*, SS3T-CSD, Tikhonov, traumaattinen aivovaurio

ACKNOWLEDGEMENTS

This thesis was conducted at the A.I. Virtanen Institute for Molecular Sciences, Kuopio, Finland, and supported by the Academy of Finland and the Doctoral Program in Molecular Medicine.

First, I would like to acknowledge my primary supervisor, Docent Alejandra Sierra López, and secondary supervisor Professor Olli Gröhn for giving me the opportunity, continued support, and guidance throughout my PhD. Next, I would like to thank Assistant Professor Ferdinand Schweser from the University at Buffalo and Professor Elizabeth Hutchinson from the University of Arizona for being my preliminary examiners and providing their valuable scientific feedback for improving the thesis, and Professor Tim Dyrby from the University of Copenhagen for acting as my opponent.

To all my co-authors - I would like to express my gratitude for their persistence and valuable input in ensuring that the scientific manuscripts in this thesis reached fruition. I would specially like to thank Associate Professor Mikko Nissi and Dr. Olli Nykänen from the Department of Applied Physics, as well as Professor Karin Shmueli from the Department of Medical Physics and Biomedical Engineering at University College London, for sharing their expertise and knowledge in the QSM field. I also wish to thank our beloved technician Ms. Maarit Pulkkinen – first, for her help with the animal work and histology, which are a crucial part of the scientific findings in the thesis, and second, for being so jolly and positive in the lab.

To all the members of the BioNMR lab – many thanks for all the support and open-mindedness. I will definitely miss the coffee room, which was a rendezvous for “small talk”, and I will also cherish those memories playing Sähly, which helped to foster "team spirit”.

Finally, I would like to mention Professor Pete Thelwall from Newcastle University, and Professor Ferdia Gallagher and Dr. Joshua Kaggie from the University of Cambridge for their support in ensuring I complete my PhD.

I would like to dedicate this PhD to everyone that I have met during the course of my life, for everyone has taught me something valuable,

especially my family and close friends, who have been very supportive during my journey and reminded me that there is nothing more valuable in this world.

Cambridge, UK, November 2022
Karthik Sampath Kumar Chary

LIST OF ORIGINAL PUBLICATIONS

This dissertation is based on the following original publications:

I Chary, K., Nissi, M. J., Nykänen, O., Manninen, E., Rey, R. I., Shmueli, K., Sierra, A., & Gröhn, O. Quantitative susceptibility mapping of the rat brain after traumatic brain injury. NMR in Biomedicine, 34: e4438, 2020.

II Chary, K*., Narvaez, O*., Salo, R. A., San Martín Molina, I., Tohka, J., Aggarwal, M., Gröhn, O., & Sierra, A. Microstructural Tissue Changes in a Rat Model of Mild Traumatic Brain Injury. Frontiers in Neuroscience, 15: 746214, 2021.

III Chary, K., Manninen, E., Claessens, J., Ramirez-Manzanares, A., Gröhn, O., & Sierra, A. Diffusion MRI approaches for investigating microstructural complexity in a rat model of traumatic brain injury. Submitted.

*These authors contributed equally to this work.

CONTENTS

ABBREVIATIONS

3D	3-dimensional
ADC	Apparent diffusion coefficient
AFD	Apparent fiber density
AD	Alzheimer's disease
AD	Axial diffusivity
CCI	Controlled cortical impact
CSD	Constrained spherical deconvolution
CSF	Cerebrospinal fluid
CT	Computed tomography
DAI	Diffuse axonal injury
dMRI	Diffusion MRI
DTI	Diffusion tensor imaging
DWI	Diffuson-weighted imaging
TE	Echo time
FA	Fractional anisotropy
FBA	Fixel-based analysis
FDR	False discovery rate
FEW	Family-wise error
FD	Fiber bundle density
FDC	Fiber density and bundle cross-section
FC	Fiber bundle cross-section
FID	Free induction decay
fODF	Fiber orientation density function
FOD	Fiber orientation distribution
FPI	Fluid percussion injury
FWF	Free-water fraction
GM	Grey matter
GE	Gradient echo

iFOD2	second order integration over fiber orientation distributions
IWLS	iteratively weighted least squares
LFPI	Lateral fluid percussion injury
MD	Mean diffusivity
MGE	Multi-echo gradient-echo
MRI	Magnetic resonance imaging
MS	Multiple sclerosis
MSMT-CSD	Multi-shell multi-tissue CSD
mTBI	mild TBI
NDI	Neurite density index
NMR	Nuclear magnetic resonance
NODDI	Neurite orientation dispersion and density imaging
ODI	Orientation dispersion index
PBS	Phosphate-buffered saline
PD	Parkinson's disease
PDF	probability density function
PDF	Projection onto dipole fields
QSM	Quantitative susceptibility mapping
RD	Radial diffusivity
RF	Radiofrequency
ROI	Regions-of-interest
sTBI	Severe TBI
SNR	Signal-to-noise ratio
SS3T-CSD	Single-shell 3-tissue CSD
TBI	Traumatic brain injury
TE	Echo time
TWI	Track-weighted imaging

VBA Voxel-based analysis

VOI Volume-of-interest

WM White matter

1 INTRODUCTION

Historically, the localization of nuclear magnetic resonance (NMR) signals utilizing magnetic field gradients (Lauterbur, 1973; Mansfield & Grannell, 1973) laid the technical foundations of MRI that we know today. MRI enables characterization of brain structure and function in a non-invasive manner. Conventional structural MRI-based T_1- and T_2-weighted contrasts have become the core of virtually every neuro-MRI protocol in the clinics, reporting pathological processes based on their T_1, T_2 signal behavior, spatial location, and morphological features (Symms et al., 2004). However, they lack sensitivity to detect the subtle tissue changes observed in neurodegenerative diseases, especially in the very acute and chronic phases (Blamire, 2018; Collorone et al., 2021; Enzinger et al., 2015; Smith et al., 2019; Symms et al., 2004).

Contrast mechanisms underlying phase (Bradley, 1993) and diffusion MRI (dMRI) (Wesbey et al., 1984) can probe changes in tissue susceptibility and microstructure (Tong et al., 2003), and offer a valuable alternative to conventional structural MRI methods. In this context, a recently developed technique such as susceptibility-weighted imaging, which utilizes the susceptibility differences of compounds has been progressively used for the diagnosis of various neurological disorders (Haacke et al., 2009; Mittal et al., 2009), where conventional T_2* weighted gradient-echo (GE) sequences fail (Babikian et al., 2005; Shoamanesh et al., 2011; Tong et al., 2004). Along similar lines, diffusion tensor imaging (DTI) has been very commonly used to investigate changes in WM *in vivo* by allowing robust estimation of parameters (Pierpaoli et al., 2001) sensitive to tissue microstructure (Beaulieu, 2013). However, inherent limitations of these quantitative MRI techniques restrict their specificity for assessing pathological changes in the brain (Bourke et al., 2021; Jones et al., 2013; Shmueli et al., 2009). Advancements in image acquisition and post-processing approaches has thereby, led to further developments in this regard and offer new avenues in assessing pathological tissue (Alexander et al., 2019; Shmueli et al., 2009; Wang & Liu, 2015).

Traumatic brain injury (TBI) is a serious source of disability, morbidity, and death worldwide (Dewan et al., 2019), as well an overwhelming health and economic burden in our society. Particularly, subtle secondary tissue changes after the initial trauma renders TBI to be a complex pathology and is a crucial factor affecting the quality of life of a patient (Stocchetti & Zanier, 2016). More so, changes due to secondary damage can persist months to several years post-injury, as the secondary damage may also progress to connected brain areas (Bramlett & Dietrich, 2015; Johnson et al., 2013; Lehto et al., 2012; Nisenbaum et al., 2014). Improved non-invasive imaging markers to detect TBI-related pathological changes can lead to a significant improvement in this regard.

Therefore, in this thesis, we focused on imaging of severe and mild TBI-related brain pathology using more advanced susceptibility and dMRI-based approaches as compared to conventionally used R_2* and DTI for characterizing secondary tissue alterations in an experimental TBI model. Using high-resolution *ex vivo* MRI, we performed quantitative mapping to assess local variations in tissue susceptibility (study **I**) and applied higher-order diffusion modelling approaches to investigate alterations in tissue microstructure (study **II**) and tissue microstructural complexity (study **III**). The sub-acute and chronic phase after TBI is associated with several pathological processes, therefore we combined our MRI findings with histological corroboration as ground truth. To fully examine the extent of the secondary damage, we also assessed areas spatially extending from the primary injury site and compared the MRI findings with more conventional MRI techniques. We hypothesized this approach would provide a deeper understanding of the biophysical origins of these advanced quantitative methods, and limitations in their applicability.

2 REVIEW OF THE LITERATURE

2.1 MAGNETIC RESONANCE IMAGING

2.1.1 Physics of nuclear magnetic resonance

Rabi et al., 1938 initially described the NMR phenomenon as a method for measuring magnetic properties of atomic nuclei. Microscopically, magnetism in materials can result from the orbital motion of electrons, the intrinsic electron moments (electron spins), and the intrinsic moments of atomic nuclei (nuclear spins). All particles having an inherent angular momentum or spin S also have a corresponding magnetic moment μ. The interaction of a particle with an externally applied magnetic field B is expressed in terms of a vector quantity, known as magnetic moment. Equation (2.1) gives the relation between μ and S,

$$\mu = \gamma \hbar S \tag{2.1}$$

where γ represents the gyromagnetic ratio for a given nucleus in Hz, $\hbar$ is the Planck's constant. Without any field source externally, the spins are randomly oriented, and S is degenerate. When magnetism is induced by a certain magnetic field strength, the spin angular momentum is quantized and can have 2S+1 possible values. Only nuclei associated with non-zero spin remain MRI active. Spin-1/2 nuclei such as hydrogen ^{1}H, therefore, can only have two spin states of ±1/2 (Levitt, 2002). These states can be termed as being parallel (+1/2) and anti-parallel (-1/2) to B. The magnetic energy level of each state (ε) given by Equation (2.2),

$$\varepsilon = -\mu \cdot B = -\gamma \hbar S \cdot B_0 \tag{2.2}$$

where B_0 is the external magnetic field set in the z-direction. The negative sign in Equation (2.2) indicates that the magnetic moment of spins aligned

in parallel have the lowest energy. The difference in energy between the two nuclear spin states is represented by Equation (2.3),

$$\Delta\varepsilon = \left(\frac{1}{2} - -\frac{1}{2}\right) - \gamma\hbar B = -\gamma\hbar B_{o} \tag{2.3}$$

And the relative ratio of spins between these 2 states is given by Equation (2.4) (Boltzmann's distribution),

$$\frac{n(+)}{n(-)} = e^{\frac{\Delta\epsilon}{K_B T}} \tag{2.4}$$

where $\Delta\varepsilon$ is the energy difference, K_B is the Boltzmann's constant (1.38066×10^{-23} JK^{-1}), T is the temperature in SI units (Kelvin). From Equations (2.3) and (2.4), we can see that the energy difference is directly proportionate to the B_o magnitude applied and inversely proportional to the temperature.

2.1.2 Spin precession

The spin polarization axes are randomly oriented in the absence of any B_o. As a result, the net magnetic moment is almost zero, with roughly the same number of spins aligned towards and against it. In the presence of B_o, the spin polarization vectors perform a steady precession around B_o with a frequency given by Equation (2.5),

$$\omega o = -\gamma Bo \tag{2.5}$$

where ω_0 denotes the Larmor frequency in Hz. In addition to precession, the spins also undergo rapid microscopic field fluctuations due to thermal wandering motion of the environment. The finite temperature of the environment, however, makes the spins to be more inclined in orientating towards the lower magnetic energy state. This causes a slight bias towards spin orientations with magnetic moments along B_o. The resulting anisotropic distribution of spin polarizations along B_o, known as the thermal equilibrium, causes a net magnetic moment in the longitudinal direction M. The thermal equilibrium is stable on the macroscopic scale.

However, on the microscopic scale, the individual spins precess with ω_0 and wander continuously (Levitt, 2002).

The thermal equilibrium is disturbed to receive a detectable NMR signal, by applying a radiofrequency (RF) pulse of appropriate frequency and duration perpendicular to B_o. For maximum excitation, the RF field should oscillate at the same frequency as ω_0 of the nucleus, so called on-resonance condition. The applied RF pulse has a rotating magnetic field B_1, with a much smaller magnitude perpendicular to B_0, but providing enough energy to induce transitions between the nuclear spin energy states. As a result, the remaining magnetization M in the z-direction is rotated into the xy-plane. The magnetic moments of the nuclear spins are in phase and continue to precess around B_0 as long as B_1 is switched on. The transverse component of magnetization in the xy-plane M_{xy} generates an electric current in a receiver coil tuned to the precessing frequency and placed perpendicularly to the principal magnetic field. The resulting NMR signal called the free induction decay (FID).

2.1.3 MRI relaxation mechanisms

2.1.3.1 Longitudinal relaxation

Once the B_1 field switches off, the nuclear spins re-establish equilibrium through relaxation. As explained previously, spin-1/2 nuclei experience thermal wandering motion and, relaxation occurs through the microscopic field fluctuations, resulting in energy exchange between the nuclear spins and surrounding structures (mostly due to dipole-dipole interactions). This recovery of the longitudinal component of the net magnetization M_z signifies the longitudinal relaxation. The time constant T_1 describes the exponential recovery of the longitudinal magnetization to the original state M_o, given by Equation (2.6),

$$M_z = M_0 \left(1 - e^{\frac{-t}{T_1}}\right) \tag{2.6}$$

2.1.3.2 Transverse relaxation

The decay of the transverse component of the net magnetization M_{xy} is known as transverse relaxation. As the microscopic magnetic fields fluctuate slightly, different nuclear spins experience slightly different local magnetic fields. As a result, they also precess with frequencies slightly different from ω_0 causing the magnetic moments to become slowly out of phase with each other. The time constant T_2 describes exponential decay of the transverse magnetization given by Equation (2.7),

$$M_{xy} = M_0 \left(e \frac{-t}{T_2} \right) \tag{2.7}$$

The decay of transverse magnetization can also occur from contributions other than the rotational motion of molecules such as magnetic field inhomogeneities. These can be both macroscopic and microscopic (Chavhan et al., 2009). Macroscopic static field inhomogeneities result in susceptibility differences mainly from imperfections in the main magnetic field, and other sources such as air-tissue interfaces, and also in the presence of metallic implants. Microscopic sources of susceptibility include paramagnetic contrast agents, blood products and pathology related iron deposits (Chavhan et al., 2009). These static field inhomogeneities cause a rapid decay in M_{xy} is known as T_2* shown in Equation (2.8),

$$\frac{1}{T_2^*} = \frac{1}{T_2} + \frac{1}{T_2'} \tag{2.8}$$

where $\frac{1}{T_2'} = \frac{1}{\gamma \Delta B_{inhom}}$, ΔB_{inhom} is the static field inhomogeneity across a voxel. T_2* reflects the observed T_2. Equation (2.8) shows that both T_2* and T_2 will be equal, in the absence of ΔB_{inhom}.

2.1.4 Spectral density function

The Bloembergen-Purcell-Pound theory of relaxation explains the interaction between protons and their environment due to the random

fluctuating fields arising from a range of molecular motion. The spectral density function *J(ω)* characterizes the range of motional frequencies of the molecules given by Equation (2.9),

$$J(\omega) = \frac{\tau_c}{1+ \omega_c^2 \tau_c^2} \tag{2.9}$$

where τ_c is the correlation time, ω_c is the angular frequency. *J(ω)* differs for substances with varying τ_c. The molecules in solids are densely packed and move slowly, resulting in longer τ_c, while gases and liquids have shorter τ_c as molecules are further apart and more mobile.

For a fluctuating random field, Equation (2.10) gives M_{xy} around the transverse plane as time constant T_1,

$$T_1^{-1} \propto M_{xy}^2 \frac{\tau_c}{1+ \omega_0^2 \tau_c^2} \tag{2.10}$$

Equation (2.10) shows that T_1 is most efficient for spins tumbling at Larmor frequency, and therefore, depends on the magnetic field strength. Molecules in bulk liquids such as cerebrospinal fluid (CSF), tumble over a wide range of frequencies, while tumbling of molecules bound to other larger macromolecules is restricted due to binding. More structured molecules with intermediate binding such as myelin, tumble at the Larmor frequencies and have long T_1*'s* as compared to free and bound molecules.

Similarly, for a fluctuating field, Equation (2.11) gives B_z around the longitudinal plane as time constant T_2,

$$T_2^{-1} \propto B_z^2 \tau_c^2 \tag{2.11}$$

Equation (2.11) shows that T_2 is most efficient when τ_c is 0 i.e., when molecules are immobile. T_2*'s* are shortest in bound molecules, longest in bulk fluids, and medium in molecules with intermediate binding. Free molecules with very short τ_c will experience rapidly fluctuating local magnetic fields that will average effect out effectively. This results in a more homogenous local magnetic field and very small dephasing. Reciprocally,

molecules bound to larger macromolecules with much longer τ_c tend to experience more static local magnetic field inhomogeneity's, and more dephasing effectively.

2.1.5 Spin-echo and gradient-echo

The FID signal created by applying a pulse sequence uses a sequence of RF pulses in conjunction with/without magnetic field gradients in a synchronized manner. The two most commonly used pulse sequences are the spin-echo (SE) and GE, shown in simplified forms in **Figure 1A** and **1B**.

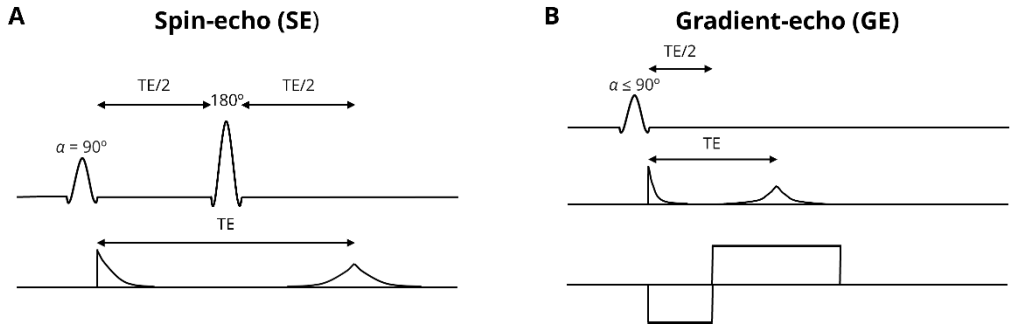

Figure 1. Conventionally used MRI pulse sequences. A) spin-echo, and B) gradient-echo. In the GE sequence, static field inhomogeneities result in rapid decay of the transverse magnetization (B), as compared to the SE sequence (A).

In the GE sequence (Haase et al., 1986), a negative gradient lobe is applied after the RF excitation pulse (α) resulting in rapid dephasing of the transverse magnetization. The subsequent application of a positive or rephasing gradient lobe, reverses the effects of the previous dephasing. The spins are shortly in phase after some time known as echo time (*TE*). As the GE sequence lacks a 180° refocusing pulse, the dephasing effects from the static field inhomogeneity's explained previously in 2.1.3.2 are preserved (Chavhan et al., 2009). Equation (2.12) gives the signal equation for a GE sequence,

$$S = k\,PD\,\frac{\sin\alpha\left(1-e^{\left(-\frac{TR}{T_1}\right)}\right)}{\left(1-(\cos\alpha)e^{\left(-\frac{TR}{T_1}\right)}\right)}e^{\left(-\frac{TE}{T_2^*}\right)} \quad (2.12)$$

where *k* is the instrument scaling factor, PD is the spin density, *α* is the flip angle used. Equation (2.12) assumes perfect steady state and absence of any residual transverse magnetization. From Equation (2.12), we can see that using a short *α or long TR* removes the T_1 effects and the measured GE signal decays with time constant T_2*.

The effects of T_2' can be reversed by using a SE sequence (Hahn, 1950). A spin-echo sequence uses a 180° RF pulse for refocusing the transverse magnetization instead of a gradient lobe. The implication of using a refocusing pulse results in rephasing of the phase shifts experienced by the spins due to static magnetic field inhomogeneity's. The SE sequence assumes the absence of any significant motion within the imaging volume, for which the spins experience the same static field inhomogeneity's before and after the refocusing pulse. Equation (2.13) gives the signal equation for a SE sequence,

$$S = k\,PD\,(1 - e^{\left(-\frac{TR}{T_1}\right)}e^{\left(-\frac{TE}{T_2}\right)}) \quad (2.13)$$

When using a $TR >> T_1$, the measured SE signal decays with time constant T_2. Besides the conventional longitudinal and transverse relaxation time constants, several other phenomena can induce contrasts in MRI. I will discuss some of these in the next section.

2.2 MAGNETIC SUSCEPTIBILITY

The induced magnetic moment (μ) by applying an external magnetic field B_0 is given by Equation (2.14),

$$\mu_{induced} = \mu_0^{-1} V \chi B_0 \quad (2.14)$$

where $\mu_0 = 4\pi \times 10^{-7}\mathrm{Hm}^{-1}$ is the permeability or vacuum constant, V is the material volume, χ is the volume magnetic susceptibility. Magnetic susceptibility (χ) is a fundamental material property (Schenck, 1996), describing the material's measure to become magnetized (M) in the presence of an applied magnetic field. For linear materials, there is a direct link between the magnetization vector and the exerted magnetic field given by Equation (2.15),

$$M = \chi B_0 \tag{2.15}$$

Depending on the molecule's electronic configuration, (χ) can be positive or negative.

Microscopically, magnetism arises from 3 sources namely 1) the intrinsic angular momentum of the spins described previously, 2) the intrinsic orbital angular momentum of the electrons, and 3) the resulting circulation of electric currents. The contributions from the electron orbital and spin angular momentum-induced magnetic moments create a positive magnetic moment or paramagnetic susceptibility ($\chi > 0$). Whereas the orbital motion of electrons along the direction of the applied field induces electron orbital currents in the direction opposite to the field, producing a slight negative magnetic moment or diamagnetic susceptibility ($\chi < 0$). Majority of the materials are diamagnetic and have χ much smaller in magnitude as compared to paramagnetic materials (Levitt, 2002). For example, for pure water $\chi = -9.05 \times 10^{-6}$. Ferromagnetic materials have permanent magnetic moments with very high susceptibility ($\chi >> 1$) and remain magnetized even when B_0 is removed. In MRI, susceptibility variations of the order of even few parts per million (ppm) can result in severe image artefacts. The most common manifestation of these artefacts is at the air-tissue interfaces of the brain, where susceptibility variations manifesting amidst air and brain tissue results in signal voids and/or image distortions. Biological tissues such as brain, muscle, liver and heart possess small (χ) values (Klohs & Hirt, 2021), usually ±20% of water, resulting only in very subtle variations in susceptibility, which can be exploited to form unique MRI contrasts.

2.2.1 Phase shift in magnetic field

Every material in the presence of an external magnetic field B_0 produces a perturbation of the field, known as a demagnetization field (Schweser et al., 2016). Differences in processional frequencies at the time of signal acquisition will lead to phase-shifts experienced over time. The phase-shift experienced by a proton is directly correlated to the gyromagnetic ratio, echo time and perturbation of the magnetic field given by Equation (2.16),

$$\delta\phi(\vec{r}) = -\gamma\, TE\, \delta B(\vec{r}) \tag{2.16}$$

where $\delta\phi(\vec{r})$ is the phase shift, $\delta B(\vec{r})$ is the field perturbation.

As explained in 2.1.5, GE phase images exhibit non-local phase changes due to induced frequency shifts and the resulting susceptibility can be calculated either from the phase $\phi(\vec{r})$ or frequency $\Delta f(\vec{r})$ maps. In this regard, acquiring multiple echoes permits a more reliable estimation of the field perturbations, with more accurate mapping of the temporal phase evolution and effectively distinguishing phase offsets by other constant sources.

2.2.2 Susceptibility contrast in biological tissues

In general, biological tissues are imaged in bulk due to the finite resolution of MR images. As such, measurements of magnetic susceptibility with MRI are directly proportional to the underlying tissue composition (Shmueli et al., 2009). In human brain tissues, the relatively weak diamagnetic susceptibility is dominated by the large presence of water (χ = -9.05 ppm) (Liu et al., 2015). In a healthy brain, the susceptibility values vary from (χ = -9.2 to -8.8 ppm) across WM to GM. This variation in (χ) results from the myelin and iron presence that differ in both concentration and susceptiblity values, as compared to water (Liu et al., 2015). In the brain WM, which is mainly composed of myelinated axons (**Figure 3A**), the phospholipids, which are slighlty more diamagnetic than water are the dominant source of diamagnetic susceptibility (χ = -9.68 ppm) (Liu et al., 2015). (Liu et al., 2011) demonstrated almost complete reduction of WM-

GM susceptibility contrast in shiverer mice, indicating myelin is the primary source of contrast between WM and subcortical GM in the brain. Iron in brain tissue can either represent storage iron such as ferritin (non-heme iron) or heme protein bound such as haemoglobin (heme iron) (Haacke et al., 2005; Schenck, 1996). In subcortical GM, ferritin is the dominant source of paramagnetic susceptibility, and deoxyhemoglin in blood. A wider range of (χ) values can be observed in pathological tissues. For example, iron deposition resulting from neurodegeneration or microbleeds exhibit larger (χ) values, rendering them strongly paramagnetic (**Figure 3B-E**) (Duyn & Schenck, 2017; Wang & Liu, 2015). Pathological tissues also exhibit calcifications, in the form of hyrdoxapatite with (χ = -14.82 ppm), rendering them slighlty more diamagnetic than water (**Figure 3C-E**) (Duyn & Schenck, 2017).

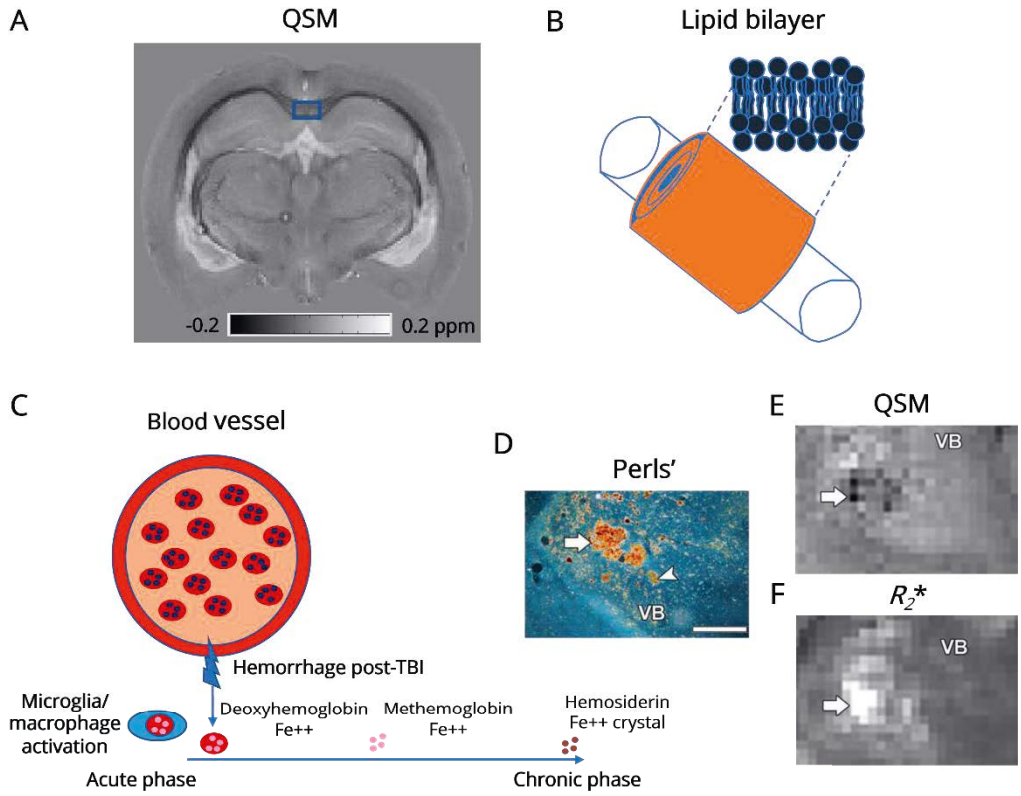

Figure 3. Myelin and iron are the main contributors to the susceptibility contrast in the brain. A) In the QSM map, the corpus callosum (indicated by blue box) is diamagnetic due to myelin that B) contains numerous layers of lipid. C) Iron in red blood cells is weakly paramagnetic. Following hemorrhage, a small fraction of red blood cells, may get endocytosed by activation of microglia/macrophages, while the remaining majority of red blood cells undergo breakdown and degradation to eventually take the form of hemosiderin, which is strongly paramagnetic. (D, E, and F) Iron deposition in the form of hemosiderin can be observed in the ventrobasal complex at the chronic phase post-severe injury (indicated by the white arrowhead in D), and the QSM and R_2* maps (E and F). In addition to iron, calcifications (indicated by the white arrows in D, E, and F), are also observed at the chronic phase, and can be differentiated from paramagnetic iron in QSM (E) as compared to R_2* (F) maps. Scale bar: 400 µm. Adapted with permission from (Wang & Liu, 2015), *Magn Reson Med, 73*(1):82-101.

In general, it is assumed that the observed differences in MRI phase contrast originate solely from differences in magnetic susceptibility. In a post-mortem study, (Langkammer et al., 2013) showed good correlation of the measured bulk susceptibility with iron burden in subcortical GM. However, the association of measured iron content in WM regions was suboptimal and suggesting the presence of other confounding phase contrast mechanisms. In addition to bulk magnetic susceptibility, chemical exchange amongst water and macromolecular protons could induce local resonance frequency shifts. However, chemical shift effects are significant only when imaging tissues with large amounts of fat and their effects can be neglected when imaging brain. Moreover, chemical exchange between water and macromolecules was found to be negligible as compared to susceptibility effects in the brain in several studies (Leutritz et al., 2013; Shmueli et al., 2011; Zhong et al., 2008).

2.3 QUANTITATIVE SUSCEPTIBILITY MAPPING (QSM)

2.3.1 Field perturbation and susceptibility (χ)

If the magnetization induced by susceptibility sources is considered as a magnetic dipole, the field perturbation from a distribution of known susceptibility sources is obtained by a convolution of the isotropic susceptibility distribution by the unit dipole kernel (**Figure 4**).
This computation corresponds to a multiplication, which is point-wise in k-space as shown in Equation (2.18), which forms the basis for QSM (Wang & Liu, 2015).

$$\Delta B_z(k) = B_0 \left(\frac{1}{3} - \frac{k_z^2}{|k^2|}\right) \chi(k) \qquad (2.18)$$

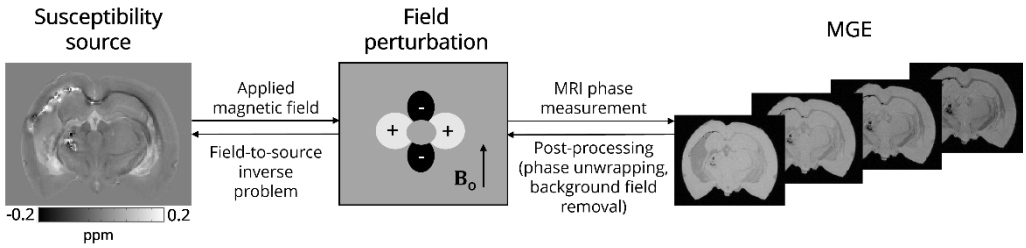

Figure 4. QSM relies on quantifying susceptibility distribution from a known source by applying a magnetic field and solving an inverse problem.

Where, k and k_z are the k-space vectors, and its z-component; $\Delta B_z(k)$ and $\chi(k)$ are the Fourier transforms of the field perturbation corresponding to the z-component, and the magnetic susceptibility distribution. The Fourier transform of the field perturbation can be obtained from the phase shifts using multi-echo gradient-echo (MGE) phase images and the susceptibility map can be subsequently obtained by an inversion. However, prior to the inversion process, processing of the GE phase maps is required to accurately map the local tissue susceptibilities.

2.3.2 Mapping local tissue susceptibility (χ)

The phase values in MRI are only detected in the range of -π to π, instead of the full phase evolution. There will be aliasing if the phase eclipses ±π resulting in abrupt phase jumps of 2π seen as sharp edges in the raw phase images. These are known as phase warps, and the warped phase $[\phi_w(\vec{r})]$ masks out the true phase evolution $[\phi(\vec{r})]$ which needs to be accounted for by appending multiples of 2π as shown in Equation (2.19),

$$\phi(\vec{r}) = \phi_w(\vec{r}) + n(\vec{r}) \cdot 2\pi \tag{2.19}$$

where, $n(\vec{r})$ denotes the integer number for a specific pixel location. There are several approaches for phase unwrapping either in the spatial or temporal domain, which impose continuity or smoothness on the phase jumps in unwrapping the phase effectively (Wang & Liu, 2015). Following which, a simple division of the unwrapped phase with the term $\gamma.TE$ yields the field perturbation. However, the field perturbation is not restricted to its origin spatially and extends throughout all space. Therefore, for a given volume-of-interest (VOI), it also contains susceptibility distributions from sources outside the VOI.

These so-called background sources of susceptibility can result from air-tissue interfaces exhibiting large differences in susceptibility such as the bone, paranasal sinuses, as well as susceptibility variations from the inhomogeneity's in the main magnetic field and shimming fields. Compared to the internal field contributions, the background field contributions are considered as slow varying and an order or two of magnitude stronger (tissue susceptibilities $|\chi| \ll 1$).

One of the simplest approaches to discard the background field contributions, therefore, is to use high-pass filtering such as homodyne filtering (Noll et al., 1991) by dividing complex data by a smoother version of the same data. Although, successfully applied in susceptibility-weighted imaging (SWI), homodyne filtering can also erroneously remove some of the tissue-related low frequency contributions and fails to filter out background contributions due to stronger field fluctuations. However,

several other advanced approaches enable more efficient background field removal (Schweser et al., 2011) required for susceptibility quantification which has been utilized in this thesis.

2.3.3 Dipole inversion

In order to retrieve the susceptibility map from the local field tissue map shown in Equation (2.18), a deconvolution needs to be performed between the field map and the unit dipole kernel. Such a deconvolution corresponds to a division in k-space, which is point-wise. The recovery of the susceptibility map from the local field tissue map, however, has many challenges from the presence of zeroes in the dipole kernel on two conical regions at the magic angle of 54° or 108° wrt B_0. In these two conical regions, the inverse kernel is undefined (Wang & Liu, 2015). The QSM map, therefore, must be computed by some conditioning of the ill-posed inversion process. A time-efficient and computationally least intensive approach is based on masking the dipole kernel by thresholding to replace regions that are undefined (Wharton et al., 2010). However, as data is irretrievably lost, this approach also incorporates masking to remove regions associated with severe streaking artefacts, mainly around those with large susceptibilities such as veins. Effective reduction of streaking artefacts and noise amplification was reported by (Shmueli et al., 2009) using modifying/truncating the dipole kernel with a constant value. However, the use of highly excessive truncation values may lead to undervaluation of the Fourier coefficients in the susceptibility map, which has to be addressed by an appropriate correction factor (Schweser et al., 2013).

A more reliable dipole inversion can be achieved by replacing the missing k-space data near the conical surfaces by minimizing the variability between the computed magnetic field, and the one obtained by convolving the dipole response and the susceptibility distribution. These regularization-based approaches utilize either an L1-norm minimization (least absolute error) or L2-norm minimization (least squares error) for optimizing the solution to the inverse problem. The morphology enabled dipole inversion (Liu et al., 2012) is another method which uses prior

spatial information from a GE magnitude image to define edges in the susceptibility map and further, imposes this information using L1 regularization to obtain the susceptibility distribution. These dipole inversion algorithms are based on a single orientation GE acquisition, which lead to under sampling of the k-space in regions near the conical surfaces. This under sampling can be avoided by collecting the data in multiple orientations wrt B_0 and sampling the entire k-space (Liu et al., 2009).

2.4 DIFFUSION MRI

Diffusion MRI (dMRI) is sensitive to the diffusive properties of water molecules and is an MRI technique that provides microstructural tissue information non-invasively.

2.4.1 Physics of diffusion

Molecular diffusion results from the translational movement of water molecules via random thermal motion, called Brownian motion. Equation (2.20) represents the mathematical basis for molecular mobility based on Brownian motion,

$$< X^2 > = 2 \cdot D.T_d \tag{2.20}$$

where $< X^2 >$ is the average diffusion distance (mm), D is the diffusion co-efficient (mm^2/s) and T_d represents diffusion time in seconds. Equation (2.21) describes the Stokes-Einstein relation describes D for a spherical particle as,

$$D = \frac{k_B T_d}{6\pi n R} \tag{2.21}$$

where k_B denotes the Boltzmann's constant, R is the particle radius, n represents medium viscosity. For example, freely diffusing water molecules at 37°C have a diffusion coefficient of around 3×10^{-3} mm^2/s.

For such unconstrained motion, as observed in large fluid filled cavities deep within the brain such as the ventricles, diffusion is considered isotropic. The Gaussian distribution Equation (2.22) describes the water molecular displacement under isotropic diffusion as,

$$f(x) = \frac{1}{\sigma\sqrt{2\pi}} e^{-x^2/2\sigma^2} \tag{2.22}$$

where the term $\frac{1}{\sigma\sqrt{2\pi}}$ denotes the scaling factor for normalizing the area under the curve to 1, *x* refers to the axis along which the population of water molecules have been displaced, and σ regulates the width of the curve (Mori & Tournier, 2013). Using Equation (2.22), the parameter *σ* can be substituted to $\sqrt{2DT_d}$ to estimate the average distance travelled by a population of water molecules along one dimension (x) in each time interval (t) as,

$$P_{(x,t)} = \frac{1}{\sqrt{4\pi Dt}} e^{-x^2/4Dt} \tag{2.23}$$

Equation (2.23) is a function of *t* (distribution becomes wider with increasing time), x (the direction of the applied diffusion gradient) and *D* (higher diffusion coefficients corresponds to a wider distribution, for fixed *t*). In the three-dimensional (3D) space, a single value of *D* in all three directions characterizes isotropic diffusion, without any preferentiality.

2.4.2 Diffusion sensitization with MRI

(Carr & Purcell, 1954) first described the effects of diffusion on spin relaxation mechanisms. As such, nearly any MRI sequence can achieve sensitization to diffusion by applying a dephasing-rephasing gradient. For immobile spins, the accumulated phase during the dephasing gradient is inverted by the application of the rephasing gradient. However, for mobile spins along the direction of the applied gradients, there will be residual phase accumulation. The resulting phase difference of these spins will cause signal attenuation in the MR measurements (le Bihan et al., 2006).

The diffusion gradient scheme applied, however, results in considerable signal loss to T_2* decay, between the duration of the dephasing-rephasing gradients. A more practical approach was introduced by (Stejskal & Tanner, 1965), which incorporated diffusion sensitizing gradients in a SE sequence to refocus the T_2* related signal loss. This is called the pulsed gradient spin-echo (PGSE) method (**Figure 5A**). For immobile spins, the rephasing gradient will compensate the effects of the initially applied dephasing gradient. If the displacement of spins is isotropic, the signal attenuation will be same irrespective of the gradient direction. However, spins displacing along the gradient axis due to certain anisotropy will lead to much stronger signal attenuation. Equation (2.24) describes the signal attenuation at an echo time along the direction of the applied gradient (Stejskal & Tanner, 1965),

$$\begin{aligned} A(TE) &= exp\left(-\gamma^2 G^2 \delta^2 \left[\Delta - {}^{\delta}/_{3}\right] D\right) \\ &= exp(-\gamma^2 G^2 \delta^2 D),\ \delta \ll \Delta \end{aligned} \tag{2.24}$$

where G is the strength of the diffusion gradients in mT/m, δ is the duration of the diffusion gradients in ms. Equation (2.25) can be rewritten by combining the contributions of the diffusion and imaging gradients in a single term as,

$$A(TE) = e^{-bD} \tag{2.25}$$

where the term b denotes the b-value in s/mm^2 that regulates the diffusion weighting contrast in the sequence (le Bihan et al., 1986).

The rapid on-off switching of the gradients in the PGSE method is highly susceptible to eddy current distortions therefore, most sequences utilize a using a pair of bipolar gradient lobes for diffusion sensitization (**Figure 5B**).

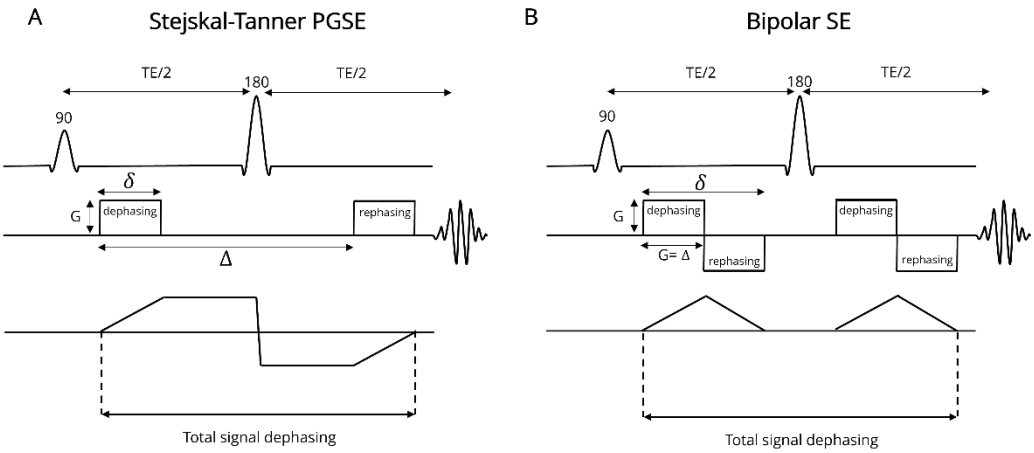

Figure 5. Diffusion MRI SE sequences using, A) conventional unipolar PGSE, and B) bipolar diffusion gradient lobes.

2.4.3 Diffusion contrast in the brain

In biological tissues which exhibit a more ordered microstructure compared to fluid-filled cavities such as the ventricles, the measured diffusion coefficient has a directional dependence on the applied diffusion encoding. This directional dependence of water molecular diffusion is called diffusion anisotropy. In the brain, this is predominantly observed in the WM, also in the GM (Jespersen et al., 2012; Palombo et al., 2020; Zhang et al., 2012), while the CSF can be thought of being isotropic (Cercignani & Horsfield, 2001). Diffusion in WM is strongly dictated by the axonal membranes that permit diffusion along its direction (D_{axial}) while hindering diffusion radially (D_{radial}).

Other cellular components such as myelin, neurofilaments and neurotubules also influence anisotropy by hindering the diffusion of water molecules in the radial direction (Beaulieu, 2002). In rodents, diffusion anisotropy is also observed in GM structures, which exhibit laminar organization, such as the cortex and hippocampus (Assaf, 2019). The average diffusion distance is on the order of 4-15 μm in the timescale of typical diffusion experiments (around 10-100 ms), and the neuronal structures being typically smaller than this range impart anisotropy to the diffusion process (Mori & Tournier, 2013). dMRI aims to exploit this

phenomenon by applying a set of diffusion gradients to generate a unique contrast, reflecting the tissue microstructure (Mori & Zhang, 2006), not observed in conventional MRI techniques.

2.4.4 Apparent diffusion coefficient and diffusion tensor imaging

The fundamental principles of the apparent diffusion coefficient (ADC) were laid in the 1980s (Wesbey et al., 1984). The calculation of diffusion coefficients was first reported by (le Bihan et al., 1986) by comparing the signal amplitudes of an image acquired with diffusion weighting and a T_2-weighted image without diffusion weighting.

The first TBI-related studies aimed to characterize diffusivity in experimental models of focal contusion showed both decreases (Alsop et al., 1996; Stroop et al., 1998; Unterberg et al., 1997) and increases (Hanstock et al., 1994) in diffusivity in the initial few hours post-injury. Specifically, cellular damage processes such as metabolic disruption, beading, and cytotoxic oedema have been suggested for observed decreases in diffusivity, whereas, vasogenic oedema has been associated with increases in diffusivity. This underlined the potential of DWI in distinguishing divergent pathophysiological features of TBI (D. H. Smith et al., 1995), and predicting patient outcome (Galloway et al., 2008; Hou et al., 2007).

However, under anisotropic circumstances, a scalar ADC value alone is insufficient in providing a comprehensive description of the diffusion process. Complete characterization of the underlying diffusion process can be obtained by means of a 3x3 matrix known as a 'tensor' (Basser et al., 1994). This enables measurement of the diffusion process based on a Gaussian assumption in 3D space. The diffusion tensor is symmetric and solving it requires a minimum of six distinct diffusion directions and one without any diffusion weighting. By matrix diagonalization, three pairs of eigen values ($\lambda_1, \lambda_2, \lambda_3$) and eigen vectors ($v_1, v_2, v_3$) are computed for every tensor. The derived tensor components can be represented in the form of an ellipsoid, which represents the 3D diffusion distance of the molecules with a given diffusion time. The Eigen vectors describe the orientation of the

axes and Eigen values describe the diffusivities along these axes. Together, they determine the size and shape of the ellipsoid.

Interpretation of the diffusion indices in biological tissues are facilitated by scalar maps, which are rotationally invariant, and represent the magnitude of diffusion or the degree of anisotropy (Pierpaoli & Basser, 1996). Some of the most used scalar maps are mean diffusivity (MD), axial diffusivity (AD), radial diffusivity (RD), and fractional anisotropy (FA).

MD represented by Equation (2.26) is the average of the diffusion tensor's Eigen values. AD represented by Equation (2.27) is a measure of diffusivity along the principal direction of the diffusion ellipsoid. RD as shown in Equation (2.28) is a measure of diffusivity perpendicular to the principal diffusion direction. FA is the normalized variance of the diffusion tensor's Eigen values as shown in Equation (2.29) and measures the fraction of diffusion which is anisotropic.

$$MD = \frac{\lambda_1 + \lambda_2 + \lambda_3}{3} \tag{2.26}$$

$$AD = \lambda_1 \tag{2.27}$$

$$RD = \frac{\lambda_2 + \lambda_3}{2} \tag{2.28}$$

$$FA = \sqrt{1/2}\,\frac{\sqrt{(\lambda_1 - \lambda_2)^2 + (\lambda_2 - \lambda_3)^2 + (\lambda_3 - \lambda_1)^2}}{\sqrt{({\lambda_1}^2 + {\lambda_2}^2 + {\lambda_3}^2)}} \tag{2.29}$$

In addition to the Eigen values, the orientation information from the major Eigen vectors can be also visualized in the form of directionally encoded color maps by modulating the FA map with the major eigen vector v_1.

2.5 HIGH-ANGULAR RESOLUTION DIFFUSION IMAGING

Despite the relative simplicity, DTI has shown to provide sensitivity in detecting a myriad of cellular alterations in several neurological disorders (Tae et al., 2018). However, the diffusion tensor model also suffers from

numerous limitations in probing biological tissues most notably, the non-Gaussian nature of diffusion and the 'the crossing fiber problem'. Briefly, in biological tissues, water molecular diffusion is non-Gaussian, as there exists numerous barriers to the diffusion process such as axonal membranes, myelin sheaths and the presence of intra- and extracellular compartments. These result in a non-monoexponential signal behaviour when measuring diffusion at multiple b-values (Jensen & Helpern, 2010). Although misleading, the crossing fiber problem basically refers to the existence of numerous fiber-bundle populations in the same voxel that may cross, brush each other or exhibit have a fanning geometry (Tournier et al., 2011). Such scenarios limit the Gaussian-based tensor models ability in characterizing the fiber orientations, as being discrete. This results in gross-underestimation of the underlying diffusion signal and anisotropy. Crossing fibers have been observed pronouncedly in the WM (Behrens et al., 2007), while more than 90% of the voxels in WM in human brains show the presence of multiple fiber bundle populations (Jeurissen et al., 2010). As a result, the changes detected by tensor-based metrics are voxel-averaged. Although, measures, such as the mean ADC remain largely unaltered, other measures such as the axial and radial diffusivities are affected (Wheeler-Kingshott & Cercignani, 2009). Although, it is important to note that the crossing fiber problem is less problematic in rodents given their simplistic WM neuroanatomy, the effect of voxel-averaging is persistent in both human and rodent brains. This effect becomes more prominent in areas with low anisotropy such as GM voxels, and voxels in WM exhibiting partial volume effects (Wheeler-Kingshott & Cercignani, 2009). The presence of such complex microstructural environments requires dense sampling for a better estimation of the angular features of the diffusion signal. One of the approaches is high angular resolution diffusion imaging (HARDI) (Tuch et al., 2002); an extension of the basic DTI protocol, which sensitizes diffusion along a larger number of directions than required for conventional DTI, thereby adding more specificity to the dMRI measurements. Such diffusion sensitization, uniformly distributed over a half-sphere prevents any bias amongst structures oriented along different directions. Moreover, the angular frequency of the DW signal

depends on the b-value, with several studies demonstrating that the use of higher b-values improves the angular contrast and thereby, more effectively resolves the crossing fibers (Tournier et al., 2013). Therefore, to ensure robust estimation of the multiple fiber populations, an optimal HARDI acquisition scheme should incorporate a sufficiently high b-value in combination with a minimum number of diffusion directions sampled per each b-value.

2.5.1 Higher-order models for diffusion MRI

Over the last decade, there has been a high prevalence of higher-order approaches for modelling dMRI data to estimate within voxel tissue microstructure. These models can be generally classified into 'parametric' and 'non-parametric' approaches. Parametric approaches rely on conditioning the dMRI signal using discrete models to estimate a fixed number of biologically pertinent quantitative measures, such as volume fractions of neurites (Zhang et al., 2012). These approaches are also known as biophysical models. In addition, parametric approaches also include higher-order physical models such as diffusion kurtosis imaging that parameterizes the non-Gaussian signal behaviour (Jensen & Helpern, 2010) and mean apparent propagator that estimates the diffusion propagator (Özarslan et al., 2013). Non-parametric approaches estimate the continous distribtution of fiber orientations in a voxel, such as fiber orientation distribution functions (fODFs). Non-parametric approaches are based on either q-space such as q-ball imaging (Aganj et al., 2010; Descoteaux et al., 2007; Tuch et al., 2002), and spherical deconvolution (Tournier et al., 2007) and it's associated methods (Dell'Acqua & Tournier, 2019; Jeurissen et al., 2019; J. D. Tournier et al., 2007).

Spherical deconvolution (SD) used in studies **II** and **III** is a mixture model-based approach. It estimates the continuous distribution of fiber orientations within a voxel or the fiber orientation distribution (FOD) (Tournier et al., 2004) (**Figure 6**). The model assumes the diffusion signal profiles from a single WM fiber population also known as the response function to be similar throughout the brain, except for differences in

orientation. Although, this assumption might sound unrealistic given the variations in axonal diameters and densities in WM, degree of myelination and other potential confounders such as membrane permeability, intra-axonal spacing (Beaulieu, 2002), these effects tend to average out on the voxel level and have a very negligible effect on anisotropy and the resulting fiber orientations (Tournier et al., 2004). A matrix inversion produces the fiber ODF by deconvolution of the response function in the spherical coordinate space, equivalent to Fourier transform in the Cartesian coordinate space. As such, the maximum angular resolution achievable is dictated by the integer harmonic degree l_{max} ($l_{max} \geq 0$). This requires sampling the diffusion signal with a minimum number of coefficients $\frac{1}{2}(l_{max} + 1)(l_{max} + 2)$ in fully characterizing the spherical function. For example, a spherical harmonic degree of 8 ($l_{max} = 8$) would require a minimum of $\frac{1}{2}(8 + 1)(8 + 2) = 45$ unique diffusion directions. However, the SD approach being ill-posed is very susceptible to noise, and the high frequency noise component induces negative lobes in the reconstructed FODs. The approach used in this thesis, thereby requires imposing a non-negativity constraint on the estimated FOD's, which is suitably termed as constrained spherical deconvolution (CSD) (Tournier et al., 2007). The multi-shell version of CSD, multi-shell multi-tissue CSD (MSMT-CSD) (Jeurissen et al., 2014) also decomposes the signal contributions to WM, GM, and CSF compartments. More recently, it has been possible to reap similar benefits using the single-shell 3-tissue CSD (SS3T-CSD) (Dhollander & Connelly, 2016) approach. SS3T-CSD was utilized in study **III** to distentangle the signal contributions from multiple tissue types post-severe trauma. In the context of CSD, a HARDI acquisition scheme with a b-value of 3000 s/mm^2 and a minimum of 45-50 unique diffusion directions has been suggested to be the most practical for resolving multiple fiber orientations based on simulations under *in vivo* conditions (Tournier et al., 2013) and in mouse brain *ex vivo* (Crater et al., 2022).

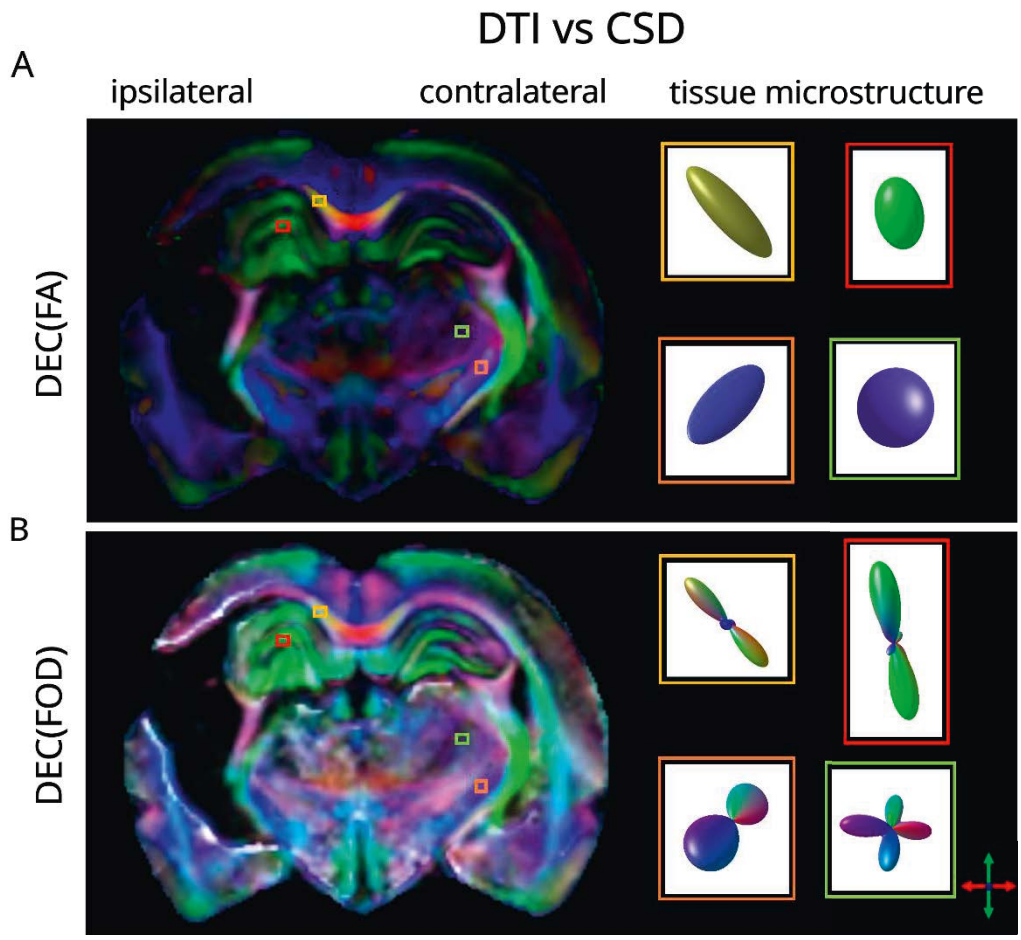

Figure 6. Conventional diffusion tensor modelling versus higher-order approaches. A) as compared to DTI, B) CSD provides better estimation of the local tissue microstructure. By estimating local fiber orientations, CSD reveals the presence of multiple fiber populations in highly anisotropic WM regions such as the corpus callosum (indicated by the yellow box). Additionally, in more complex regions such as the hippocampus (red box), ventrobasal complex (green box), and internal capsule (orange box), A) the tensor model oversimplifies the underlying tissue microstructure, as compared to CSD. Colours indicate directionality: red, medio-lateral; green, dorso-ventral; blue, rostro-caudal.

In addition to effectively decomposing numerous fiber bundle populations within a voxel by spherical deconvolution, the subsequent use of quantitative metrics for characterizing changes in individual fiber

populations would provide increased sensitivity. The CSD-derived quantitative measure, apparent fiber density (AFD) (Raffelt et al., 2012), is of particular interest in TBI, as one would expect loss in density of myelinated axons due to secondary processes post-trauma. In this thesis, we also employ the fixel-based analysis (FBA) framework (Raffelt et al., 2017), which represents the fiber orientation information in each voxel as a separate collection of fiber bundle populations termed 'fixels'. FBA permits group-wise comparison of fixel-specific changes in intra-axonal volume or the apparent fiber density (FD) (Raffelt et al., 2012), fiber bundle cross-section (FC) macroscopically (Raffelt et al., 2017), and combined changes in fiber density and bundle cross-section (FDC) (Raffelt et al., 2017).

FBA has successfully detected fiber-specific WM loss manifesting both microstructurally and microstructurally in patients with AD (Mito et al., 2018), MS patients with optic neuritis (Gajamange et al., 2018), or patients with first episode and chronic Schizophrenia (Grazioplene et al., 2018). When compared to FBA, voxel-based FA in these studies showed decreased sensitivity to WM changes (Mito et al., 2018), exaggeration of tissue damage (Gajamange et al., 2018), and exhibited significant differences mostly in crossing fiber regions suggesting effects from partial volume (Gajamange et al., 2018; Grazioplene et al., 2018).

NODDI utilized in study **II**, is one of the most commonly used biophysical models (Zhang et al., 2012). NODDI decomposes the dMRI signal into three compartments namely intraneurite water, extraneurite water, and CSF (Zhang et al., 2012). These compartments are representative of the volume fraction of the neurites (neurite density index; NDI), vector orientation of the neurites (orientation dispersion index; ODI), and volume fraction of free-water (free-water fraction; FWF). Thereby, these measures can provide estimates of the neurite density, and fanning or bending, and CSF contamination within a voxel (Zhang et al., 2012). The intrinsic diffusivity of the intraneurite compartment is fixed (Zhang et al., 2012), and the primary neurite orientation is set to the prinicipal eigen vector of the DTI model (Daducci et al., 2015). NODDI has been successfully utilized in a wide array of imaging applications such normal ageing (Nazeri

et al., 2015), and microstructural changes due to neurodegenerative diseases (Broad et al., 2019; Colgan et al., 2016; Kamagata et al., 2016).

2.5.2 Diffusion tractography

Tractography is one of the major applications of dMRI (J. Y. M. Yang et al., 2021), which has overseen tremendous development especially over the last decade with the emergence of higher-order diffusion models (Jeurissen et al., 2019).

Tractography techniques are broadly classified into deterministic and probabilistic approaches. Deterministic approaches generate streamlines by assuming the local fiber orientations to be collinear, when traversing from one voxel to another (Mori & van Zijl, 2002). Although computationally less intensive, it is highly sensitive to noise and partial volume effects, resulting in erroneous streamline propagation. The effect is more prominent when generating streamlines using DTI, which involves regions of low SNR corresponding to multiple fiber populations. Probabilistic tractography offers a better solution from these uncertainties, by sampling the underlying fiber orientations as a probability density function PDF to generate a density of streamlines (Behrens et al., 2003). In other words, probabilistic tractography algorithms at each step use a range of probable orientations to propagate to the next direction, rather than a unique solution. First-order probabilistic algorithms propagate by sampling from the FOD, which is interpolated as a PDF only at the current point, resulting in over-shoot in pathways with high curvature. Whereas second-order algorithms propagate by sampling from the FOD at multiple points (Tournier & Calamante, 2010). In this thesis, we have employed the second order integration over fiber orientation distributions (iFOD2) algorithm using the CSD model for estimating fiber orientations locally. The CSD-based higher-order probabilistic tractography used in studies **II** and **III** have demonstrated increased accuracy over the tensor-based approach (Tournier & Calamante, 2010).

2.6 TRAUMATIC BRAIN INJURY

2.6.1 TBI – a chronic disease

According to the National Institute of Neurological Disorders and Stroke, TBI is a form of acquired brain injury, which occurs when a sudden trauma causes damage to the brain. Mild traumatic brain injury (mTBI), is clinically defined by initial brief, decreased, or no loss of consciousness, disorientation, or amnesia, which tend to disappear within minutes or hours after injury (Mechtler et al., 2014; Pervez et al., 2018). Many individuals, however, still report about acute symptoms persevering for a period even up to several months after the initial injury. These include headache, dizziness, or attention/cognizance problems, or other continuing impediments, such as emotional distress, depression, sleeping disorders, or anxiety (Cole & Bailie, 2016; Ling et al., 2015; van der Naalt et al., 2017). On the contrary, severe TBI (sTBI) may lead to a permanent or extended period of unconsciousness, amnesia, or even death (Wang, 2018). Likewise, individuals suffering a severe trauma are also more likely to suffer from serious short- or long-term consequences which include motor impairments, cognitive problems, or mood disorders (Dixon et al., 1999; Kim et al., 2007; Pierce et al., 1998; Schwarzbold et al., 2008). Depending on the injury severity, acute and chronic consequences associated to TBI can result in permanent disabilities that can increase long-term mortality and reduce life-expectancy (Bramlett & Dietrich, 2015). It has been estimated that sixty-nine million individuals world-wide experience some form of TBI (Dewan et al., 2019). As such, the associated long-term effects of TBI can have drastic effects on the wellbeing of an individual and their immediate family aside from the socio-economic costs, as the occurrence of TBI is almost threefold in the low- and middle-income nations versus the affluent nations (Dewan et al., 2019).

2.6.2 TBI pathophysiology

Pathologically, TBI can be classified based on distribution of the impact as focal or diffuse and on the onset of impact as primary or secondary (Andriessen et al., 2010). Focal injuries mostly originate by contact leading to scalp wounds, skull fracture, and surface contusions resulting from the constriction of tissue below the cranium at the spot of contact or on its opposite side (Andriessen et al., 2010). Diffuse injuries lead to widespread damage to axons, vascular injury, and hypoxic-ischemic damage resulting from acceleration-deceleration forces (Andriessen et al., 2010). Both focal and diffuse injuries can co-exist and interact in an individual, rendering additional complexity to the TBI pathology (Andriessen et al., 2010).

Based on the onset of impact, the primary injury comprises of the initial damage from the mechanical forces affecting the brain tissue, whereas the secondary injury corresponds to the subsequent spurts of cellular and molecular activity provoked by the initial insult (Bramlett & Dietrich, 2002; Conti et al., 1998; Maas et al., 2008).

Neuronal death, axonal injury, demyelination, iron accumulation, calcifications are secondary changes prevalent after TBI (Daglas & Adlard, 2018; Johnson et al., 2015; Lehto et al., 2012; Nisenbaum et al., 2014; Smith et al., 2013). Neuronal death leading to irreversible loss of neurons results from either the initial physical damage directly or through a range of secondary processes.

Diffuse axonal injury (DAI) is the commonest consequence of TBI, which is manifested when biomechanical forces cause deformation amongst axons beyond their maximum elasticity, which may lead to complete axonal degeneration at the chronic phase (Smith et al., 2013). In the sub-acute phase, these shearing forces cause axonal swellings within 3-6 h post-injury (Smith et al., 2013), and axotomy and Wallerian degeneration become evident within 6-12 h. Demyelination results from apoptosis of the oligodendrocytes, constituting the myelin sheath. However, contrary to axonal degeneration, demyelination is a reversible process, with myelinated axons demonstrating a trend of partial recovery over time post-trauma (Reeves et al., 2005, 2012; Smith et al., 2013).

Furthermore, the simultaneous shear injuries associated with DAI also affect microvasculature near to the sites predisposed for DAI notably the grey-white matter interface, the corpus callosum and the brain stem, often manifesting in the form of small hemorrhages, which are more pronounced in severe TBI (Andriessen et al., 2010). In the chronic phase post-severe trauma, pathological accumulation of iron is in the form of hemosiderin (Fe^{3+}) crystals (Nisenbaum et al., 2014) as a consequence of hematoma and hemorrhage as explained in section 2.2.2. In addition, there is an excessive discharge of excitatory neurotransmitters including glutamate following injury, leading to abnormal extracellular concentrations of Ca^{2+} (Andriessen et al., 2010). These are transformed into calcifications in the form of hydroxyapatite, by microglia activation (Gayoso et al., 2003). Both, iron presence and calcifications can also vary in area and form based on the evolution of the disease (Duyn & Schenck, 2017; Wang & Liu, 2015; Ramonet et al., 2006).

In general, the secondary tissue changes are mostly subtle; however, they contribute to majority of the fatalities in individuals, at the chronic phase following injury (Marshall et al., 1991). Therefore, it is apparent that improvements in the identification of these changes non-invasively would attribute to superior judgement, classification, and outcome for TBI patients.

2.6.3 Experimental TBI

Owing to the complexness of TBI, animal models provide an exquisite opportunity for improved understanding of the underlying pathophysiology and investigating prospective treatment options. Rodents are the most widely used species due to their ease of availability, low costs and standardized outcome measures (Xiong et al., 2013). Broadly, the commonly used animal models of TBI in research can be classified based on the induced injury as being focal and diffuse. Focal injury models include the controlled cortical impact (CCI), diffuse models include blast injury, and mixed injury types include the weight-drop impact acceleration and fluid percussion injury (FPI) models (Ma et al., 2019; Xiong et al., 2013).

The FPI model inflicts an injury onto the exposed, intact dura of the animals via a fluid pressure pulse. The fluid pressure pulse is produced from a pendulum of a known height that hits the piston of a saline-filled reservoir (Ma et al., 2019; Thompson et al., 2005). The subsequent reverberation then causes a momentary shift and contortion of the brain tissue (Ma et al., 2019). Depending on the position of the craniotomy, FPI models can be further subdivided into midline, parasagittal and lateral (LFPI) (Thompson et al., 2005). The LFPI model, first described in 1989, is one of the most exhaustively used animal models for studying TBI (McIntosh et al., 1989).

LFPI is highly reproducible, and the injury severity is highly adjustable. In general, injury severity is derived from a mixture of fatality rate, fluid pulse pressure, righting reflexes, and apnea duration. Mild injury is established in the pressure interval of 0.9-1.5 atm, moderate injury at 1.6-2.5 atm, and any pressure exceeding 2.5 atm as severe (Ma et al., 2019). In this thesis, the mild LFPI model is used in study **II**, and the severe LFPI model is used in studies **I** and **III**, respectively. In rats, minutes from injury, it causes a mixture of cortical contusion focally and dispersed neuronal injury in subcortical areas such as the hippocampus and thalamus, which progresses to neuronal loss in 12 h (Thompson et al., 2005; Hicks et al., 1996). Progressive neurodegeneration is observed from days to months following injury, most predominantly in ipsilateral brain regions such as the cortex, thalamus, hippocampus, ventricles, and amygdala (Liu et al., 2010).

2.7 IMAGING TRAUMATIC BRAIN INJURY

Regarding applicability, QSM has exhibited more sensitivity to pathological iron accumulation than R_2 and R_2* combined (Barbosa et al., 2015; Murakami et al., 2015). In human TBI, (Liu et al., 2016) used QSM to detect cerebral microhemorrhages in military service personnel with chronic TBI, and interestingly reported decreasing susceptibility values from baseline to follow-up, possibly indicating that blood degradation products continually undergo subtle changes in the chronic stage post-TBI. In experimental TBI,

(Li et al., 2016) characterized spatiotemporal alterations in the corpus callosum post-mild injury combining DTI, T_2 mapping, QSM, and correlation with behaviour tests. Susceptibility differences revealed local increases in regions close by the primary injury corresponding with demyelination and axonal injury. The MRI results showed good congruency with behavioural experiments, and histopathological assessments in myelin staining. However, to disentangle and better understand the contributions of the multitude of tissue changes following severe trauma, it would be beneficial to include a thorough histological classification of affected brain areas, as performed in study **I** in this thesis.

In the context of DTI, most interesting observations were reported in a longitudinal study (Sidaros et al., 2008) wherein patients following injury showed decreased FA, AD, and increased RD. In the follow-up at the sub-acute phase, FA, and AD in patients with good clinical outcome, increased to attain normal levels without any accompanying increase in RD, compared to patients with poor outcome. DTI findings in experimental TBI studies over the last decade are mostly consistent with human TBI studies (Arfanakis et al., 2002). Following mTBI, several studies have highlighted the sensitivity of DTI to detect axonal damage associated with decreased FA and AD, and gliosis associated with increased RD (Hylin et al., 2013; mac Donald et al., 2007; San Martín Molina et al., 2020). Following severe LFPI in rats, decreased FA and increased RD was detected in WM at the chronic phase (Laitinen et al., 2015). On the contrary in GM, the thalamus showed a corresponding increase in FA, indicating myelin loss induced change in anisotropy. Neuronal reorganization was also observed in the hippocampus after focal TBI in rats, and changes in anisotropy and orientation ipsilaterally (Hutchinson et al., 2012; Sierra et al., 2015). Besides cellular alterations, glial alterations have also been reported by DTI metrics. These studies have reported increased FA and/or RD in the WM and GM resulting from reactive astrocytes at the chronic phase, and decreased FA in the WM close to the injury site due to demyelination and axonal degeneration/injury (Budde et al., 2011; mac Donald, et al., 2007).

DTI findings highlight the variability of DTI scalar measures to TBI pathophysiology based on the time, trauma severity and tissue category.

HARDI-based approaches present new avenues to gauge the microstructural environment and possibly lead to better identification and interpretation of pathology post-TBI. Previous studies have demonstrated fixel-based metrics such as fiber density and track-weighted imaging (TWI) metrics to be more sensitive to detect axonal degeneration following mild and severe trauma in rats *in vivo* (Wright et al., 2017, 2019). In a CCI study (McCunn et al., 2021) demonstrated NODDI-derived indices to be more sensitive to acute microstructural alterations undetected by DTI, and better detection of changes attributed to astrocyte and microglia compared to DTI (Gazdzinski et al., 2020). In humans, the incorporation of NODDI with DTI has shown to provide more insight into the tissue microstructure at the sub-acute and chronic phases following brain injury (Muller et al., 2021; Oehr et al., 2021).

3 AIMS OF THE STUDY

The aim of this thesis was to investigate the potential of advanced MRI approaches in detecting the varying pathological features of secondary tissue damage using an experimental model of mild and severe trauma.

More specifically, the aims of the individual studies were as outlined below:

1. To investigate spatial variations in susceptibility contrast using QSM for detecting subtle tissue changes due to secondary injury proximal and distal to the lesion site at the chronic phase after sTBI with comparison to R_2* (study **I**).
2. To investigate the potential of advanced multi-shell dMRI approaches such as FBA, and NODDI in comparison to conventional DTI to detect tissue microstructural alterations at the sub-acute phase after mild mTBI (study **II**).
3. To explore the potential of combining conventional and advanced single-shell dMRI approaches using DTI, and SS3T-CSD to detect tissue microstructural complexity at the chronic phase after sTBI (study **III**).

4 SUBJECTS AND METHODS

4.1 EXPERIMENTAL TBI

All the studies were performed using adult male Sprague-Dawley rats. All animal operations were implemented under licenses approved by the Animal Ethics Committee of the Provincial Government of Southern Finland and confirmed with the regulations of the European Community Council Directives 86/609/EREC.

Rats (10 weeks old, 300 – 350 g, Harlan Netherlands B.V., Horsrt, The Netherlands) were subjected to experimental TBI by LFPI (Kharatishvili et al., 2006) (n = 9; study **I**, n= 8; study **II**; n = 7; study **III**). Briefly, a single i.p. injection (6 ml/kg) of a concoction containing sodium pentobarbital (Mebunat, Orion Oy, Finland; 60 mg/kg), magnesium sulphate (127.2 mg/kg), propylene glycol (39.5%), and absolute ethanol (10%) was utilized to anesthetize rats. Subsequently, a craniectomy (Ø = 5 mm) was conducted between the bregma and lambda on the left skull convexity (anterior edge 2.0 mm posterior to the bregma; lateral edge adjacent to the left lateral ridge). LFPI was induced to the exposed dura with a fluid percussion device (AmScien Instruments, Richmond, VA, USA) using a transient fluid pulse (21 – 23 ms) to induce a severe injury (3.13 ± 0.09 atm) (studies **I** and **III**), and a mild injury (0.89 ± 0.21 atm) (**II**). After the injury, the dura was checked for intactness. Excluding the impact, similar operating procedures were induced in sham-operated rats (n = 5, study **I**, n = 6; **III**; n = 6 **II**). After the operation, the rats were moved to the animal facility and accommodated in independent cages regulated under a 12 h light/12 h dark cycle (lights on 07:00 a.m., temperature 22 ± 1˚C, humidity 50-60%) with unconstrained access to food and water. The sample size was chosen based on previous studies with the LFPI model (Laitinen et al., 2010; Sierra et al., 2015), which ensured enough statistical power.

4.1.1 Sample preparation for ex vivo MRI

Following experimental TBI, the rats were perfused after 140 days in studies **I** and **III** and after 35 days in study **II**. Briefly, rats were deeply anesthetized under 5 % isoflurane in 30%/70% O_2/N_2 gas mixture, and transcardially perfused using 0.9% saline for 2 min (30 ml/min), subsequently by 4% paraformaldehyde in 0.1 M phosphate buffer, pH 7.4 (30 ml/min) for 25 min. The brain was removed from the skull, post-fixed in a solution of 4% paraformaldehyde until imaging. In order to achieve maximum possible SNR by reducing T_1 relaxation times for dMRI approaches used in studies **II** and **III**, the brains were first moved to a solution containing 0.1M phosphate-buffered saline (PBS) containing 1mM gadolinium diethylenetriamine penta-acetic acid (Gd-DOTA, Dotarem®, Guerbet, Paris, France) (study **II**) and gadopentetate dimeglumine (Magnevist, Berlex Imaging, Wayne, NJ, United States) (study **III)** for a minimum of 72 h. Before MRI, every brain was positioned securely within a polyethylene tube filled with perfluoro polyether (Galden HS240, Vacuumservice Oy, Helsinki, Finland) to prevent tissue drying and to effectively suppress the background signal.

4.1.2 *Ex vivo* MRI acquisition

For studies **I** and **III**, the brains were imaged in a 9.4 T (400 MHz) 89-mm-vertical bore magnet (Oxford Instruments PLC, Abingdon, UK) incorporated with 100 G/cm actively shielded gradients interfaced to an Agilent DirectDrive console. A quadrature volume RF coil (diameter = 20 mm; Rapid Biomedical GmbH, Rimpar, Germany) was used for transmitting/receiving the MRI signal. For study **II**, the rat brains were imaged in an 11.7T NMR spectrometer (Bruker Biospin, Billerica, MA, USA), with a Micro5.0 gradient system (maximum gradient strength = 3000 mT/m). A birdcage volume coil (diameter = 20 mm, Rapid Biomedical GmbH, Rimpar, Germany) was used for transmitting/receiving the MRI signal.

In study **I**, a 3D MGE sequence was utilized with monopolar readout gradients a TR = 130 ms, flip angle = 25º, BW = 50 kHz, initial TE = 3 ms, no.

of echoes = 6, echo spacing = 4 ms, field of view = 15 mm × 19.2 mm × 25.6 mm, matrix size = 150 × 192 × 256, resolution = 100 μm isotropic, scan time = 1 h 40 min.

In study **II**, a 3D diffusion-weighted gradient- and spin-echo sequence (Aggarwal et al., 2010) was used with a TR = 800 ms, TE = 33 ms, rare-factor/EPI factor = 4/3, bandwidth = 100 kHz, no. of averages = 2, matrix size, = 152 x 112 x 78, spatial resolution = 150 μm^3 isotropic, zero-filled to 75 μm^3, diffusion images = 30, b-value = 3000 s/mm^2 and 6000 s/mm^2, images with minimal diffusion weighting = 3, diffusion gradient duration (δ)/separation (Δ) = 5/12 ms, scan time = 21 h.

In study **III**, a 3D spin-echo-echo-planar-imaging (SE-EPI) sequence with triple reference was employed with a TR = 800 ms, TE = 35 ms, echo spacing = 0.584 ms, no. of shots = 4, bandwidth = 250 kHz, no. of averages = 2, matrix size = 108 × 80 × 94, spatial resolution = 150 × 150 × 150 μm^3, diffusion images = 60, b-value = 3019.7 s/mm^2, images with minimal diffusion weighting = 1, gradient duration (δ)/separation (Δ) = 6/11.50 ms, scan time = 20 h 43 min. The long scan times resulted from the use of the inbuilt triple reference scheme which was the manufacturer's post-processing implementation for Nyquist ghost reduction and distortion correction in EPI. Briefly, the triple reference scheme requires acquisition of 3 reference scans; one with phase-encoding blips turned off (ref 1), one with blips turned off but the readout gradient polarity reversed (ref 2) and another with both blips and readout gradient polarities reversed (ref 3). Correction for the phase drifts between the odd and even echoes are then performed by using all the 3 reference scans.

4.2 IMAGE PROCESSING

For all the studies, raw data were reconstructed utilizing internal scripts in MATLAB (Math-works, Natick, MA, USA), 2012b; study **I**, R2017a; study **III**) and IDL (ITT Visual Information Solutions, Boulder, CO, United States; study **II**).

4.2.1 QSM and R_2* (study I)

For obtaining QSM maps, a field map was determined by fitting the complex data over multiple TE's (Liu et al., 2011). Following which a 3-D Laplacian unwrapping was performed (Schofield & Zhu, 2003) to remove residual phase wraps using a brain mask estimated from the magnitude image. The field perturbations arising from sources outside the imaging volume were removed using the projection onto dipole fields algorithm (Liu et al., 2011). Before background field removal, the brain mask was eroded by three voxels to lessen edge artefacts whist keeping the cortex as much as possible. Susceptibility maps were generated with a iterative Tikhonov inversion approach (alpha = 0.01) (Kressler et al., 2010) by adjusting for susceptibility underestimation (scaling factor = 0.2) (Schweser et al., 2013). For comparison, R_2* maps were computed utilizing non-linear exponential two-parameter fitting of the magnitude images over mutiple TE's.

4.2.2 Multi-shell CSD, NODDI and DTI (study II)

Data were subjected to denoising (Cordero-Grande et al., 2019), Gibbs unringing (Kellner et al., 2016), correction for eddy current induced geometric distortions (Andersson & Sotiropoulos, 2016), bias field correction (Tustison et al., 2010) to remove spatial inhomogeneities using the default parameters. All preprocessing steps were performed either using MRtrix3 (Tournier et al., 2019) and using MRtrix3 scripts linked with other software packages.

Using response functions for WM, GM, and PBS (replacing CSF *ex vivo*), FODs were estimated using multi-shell multi-tissue CSD (lmax = 6), which were further subjected to muti-tissue-based intensity normalization. A study template was then created using sham and mTBI brains by applying linear and non-linear registration (Raffelt et al., 2011), and the resulting warps were used to coregister the FODs from each rat brain to the study template (Raffelt et al., 2012). FODs were segmented at a peak amplitude of 0.06 and fixel-based metrics for FD, FC, and FDC were computed for each rat brain. In addition, data were fitted to a multi-compartment NODDI

model using the NODDI toolbox in MATLAB (http://nitrc.org/projects/noddi_tolbox) to derive NODDI measures including ODI, FWF, and NDI. Finally, tensor-based metrics including FA, MD, AD, and RD were estimated using both b-values by employing the iteratively weighted least squares (IWLS) method (Basser et al., 1994; Veraart et al., 2013). Finally, FBA, NODDI, and DTI metrics were coregistered to the study template using the non-linear warps generated previously.

4.2.3 Single-shell CSD, TWI, and DTI (III)

Data were subjected to similar pre-processing steps as described in study **II**. Additionally data were checked using EDDYQC (Bastiani et al., 2019) and data detected as outliers for motion and contrast-to-noise ratios (CNRs) were removed from subsequent analysis. The final dataset comprised of 10 rat brains (n(sham) = 4, n(TBI) = 6). Additionally, bootstrap aggregating was performed by removing 10 diffusion volumes from each animal.

WM, GM, and PBS response functions were computed from each sham-operated animal and averaged, and FODs were estimated using SS3T-CSD (lmax = 8) (https://3Tissue.github.io), followed by multi-tissue-based intensity normalization. FODs were segmented at a peak amplitude of 0.06 and scalar based metrics of total voxel-wise AFD, peak amplitude, complexity, primary- and secondary FD were computed. In addition, the WM, GM, and PBS signal fractions were normalized to compute 3-tissue signal fractions T_W, T_G, and T_P. Finally, tensor-based metrics including FA, MD, AD, and RD were derived using the IWLS method.

4.3 QUANTITATIVE ANALYSES

4.3.1 ROI-based analysis (study I)

Regions-of-interest (ROIs) were manually outlined (https://github.com/mjnissi/aedes) in 3 consecutive coronal slices on the first echo magnitude image. The external capsule and corpus callosum

were delineated at level -1.80 mm from bregma, rostrally to the epicenter of the primary injury. The ventrobasal complex, internal capsule, corpus callosum, and perilesional cortex were delineated at level -3.80 mm from bregma, at the epicenter of the primary injury. The ROIs were delineated both ipsilaterally and contralaterally and transferred to the computed QSM and R_2* maps to estimate the mean relative values of susceptibility values and R_2* relaxation rates.

4.3.2 Whole-brain analysis combined with ROIs (study II)

Whole-brain analyses comparing sham-operated and TBI animals were performed by a general linear model using non-parametric permutation testing (5,000 permutations) for both fixel- (Raffelt et al., 2015) and voxel-based metrics. The data were smoothed using a Gaussian filter of 0.3 mm^3 prior to analysis. FBA were conducted by connectivity-based fixel enhancement (CFE) (Smith & Nichols, 2009) using the parameters (C = 0.5, E = 2, H = 3). CFE was applied to the whole-brain tractogram derived from the study template generated utilizing the iFOD2 algorithm with number = 20 million, radius of curvature = 22.5º, minimum/maximum length = 0.3/22.5 mm, cut-off = 0.06, power = 1. The tractogram was then filtered to 2 million streamlines with spherical deconvolution informed filtering (Smith et al., 2013). Voxel-based analysis (VBA) for tensor-based metrics was performed with threshold-free cluster enhancement (TFCE) (Smith & Nichols, 2009) using the parameters (C = 6, E = 0.5, H = 2). All the analyses were rectified for family-wise error (FEW) with a *p*-value lower than 0.05 deemed statistically significant. In addition to whole-brain analysis, we also performed ROI analysis on predefined areas including the corpus callosum and external capsule at -1.80 mm and -3.50 mm from bregma, and internal capsule and ventrobasal complex at -3.50 mm from bregma in both ipsi- and contralateral areas. ROIs were manually drawn on a single rat brain in template space which was later inverse transformed into subject space for the CSD-based metrics (FD, peak amplitude, and dispersion), DTI-based-metrics (FA, MD, AD, and RD) and NODDI indices (ODI, NDI, and FWF). ROI-

based analysis for CSD-based metrics such as FC and FDC were performed on the template space.

4.3.3 ROI-based analysis (study III)

ROIs were manually outlined (https://github.com/mjnissi/aedes) in 3 consecutive coronal slices on the total-AFD maps in each rat brain at the epicenter of the primary lesion (-3.80 mm from bregma) including the corpus callosum, primary somatosensory cortex, stratum lacunosum-moleculare, dentate gyrus, ventrobasal complex, and internal capsule. The ROIs were then copied to the CSD-, and tensor-based metrics within the same animal. In addition, streamlines were generated along the thalamocortical pathway using the perilesional cortex and ventrobasal complex as seed and target ROIs, and by incorporating exclusion and inclusion ROIs. Streamlines were generated with the following parameters: minimum/maximum length = 0.15/10 mm, angle = 45°, no. of tracks = 10,000. The streamlines were generated five times and streamlines from every iteration were concatenated to derive track-weighted measures of average pathlength map (Pannek et al., 2012), and mean curvature (Calamante et al., 2012).

The ROIs in studies **I**, **II**, and **III** were selected based on previous studies that demonstrated changes in MRI and histology following LFPI in rats (Laitinen et al., 2010; San Martín Molina et al., 2020; Sierra et al., 2015).

4.4 HISTOLOGY

For histology, the brains following *ex vivo* imaging were washed for 24 h in 0.9% saline solution at 4ºC following which they were kept for 36 h in a cryoprotective solution consisting of 20% glycerol in 0.02 M potassium phosphate buffered saline (pH = 7.4). Finally, the brains were blocked, frozen with dry ice and stored at -70 º C. The brains were sectioned in the coronal plane (30 µm, 1-in-5 series) utilizing a sliding microtome. Tissue sections were stained for Nissl using thionin to evaluate the cytoarchitecture and gliosis in studies **I**, **II**, and **III**. Adjacent series of

sections were stained for gold chloride (Laitinen et al., 2010) to assess the myeloarchitecture (studies **I**, **II**, and **III**), myelin and/or axonal alterations (studies **I**, **II**, and **III**). In addition, the adjacent series of sections in study **I** also underwent Perls' staining enhanced with 3,3'-diaminobenzidine (DAB; D12384, Sigma-Aldrich, MO, USA) to determine the presence of iron (Fukunaga et al., 2010) and Alizarin Red S staining (Mäkinen et al., 2008) for calcifications in the brain tissue.

Qualitative assessment of the histological sections in studies **I, II,** and **III** were performed by an expert neuroscientist (A.S.). Only representative examples from the sham-operated and TBI group were chosen for corroborating the microstructural tissue alterations observed in the different brain areas. Finally, high-resolution photomicrographs were acquired using a light microscope (with a light microscope (Zeiss Axio Imager 2, White Plains, NY, USA) equipped with a digital camera (Zeiss Axiocam color 506).

Quantitative assessment of the histological sections was performed in study **II** using the structure tensor (ST) framework by deriving the anisotropy index (AI) (Budde et al., 2011) in mylein-stained sections, and the cell density (CD) in Nissl-stained sections employing internal MATLAB scripts to enable automated cell counting (San Martín Molina et al., 2020).

4.5 STATISTICAL ANALYSIS

Statistical analyses in studies **I** and **II** were computed utilizing GraphPad Prism (version 5.03 for Windows, La Jolla, CA, United States). In study **I**, changes amongst sham-operated and TBI rats were analysed utilizing the Mann-Whitney U-test, and changes between ipsi- and contralateral hemispheres inside the same brain were analysed utilizing the Wilcoxon matched-pairs signed-rank test. A $p < 0.05$ was considered statistically significant. In study **II**, changes amongst sham-operated and mTBI rats were analysed with the unpaired two-sample t-test. Changes between ipsi- and contralateral brain areas inside the same brain were analysed with the

paired t-test. Correlation between dMRI and histology metrics were performed using Pearson's correlation.

In study **III**, statistics were computed using Scipy (Virtanen et al., 2020), Statsmodels (Seabold & Perktold, 2010) (v1.7.1), and Pingouin (Vallat, 2018) (v0.4.0) packages in Python3 (v3.7.4) (Van Rossum, 1995). After checking for normality using the Shapiro-Wilk test (Shapiro & Wilk 1965), differences in tensor- (FA, AD, RD, and MD) and fixel-based metrics (AFD, peak amplitude, dispersion, primary FD, secondary FD, and complexity) between sham-operated and TBI rats were compared with the unpaired two-sample t-test. Changes amongst ipsi- and contralateral brain hemispheres inside the same brain were compared with the paired t-test. For the 3-tissue signal fractions, interdependence, and boundedness of the maps i.e., $T_W+T_G+T_P = 1$, and $0 < Tw, T_G, T_P < 1$ rendered conventional parametric statistical analyses unfeasible. Therefore, a compositional data analysis framework as described previously (Khan et al., 2020; Mito et al., 2020) was incorporated to convert the data into isometric log-ratio transforms. The isometric log-ratio transforms were subsequently checked for multivariate outliers using the Mahanabolis distance ($q < 0.01$) (Filzmoser, 2016), and normality by applying the Henze-Zirkler Multivariate Normality Test ($q < 0.01$) (Henze & Zirkler, 1990). Statistical analyses were performed using MANOVA between sham-operated and TBI rats, and between ipsi- and contralateral hemispheres inside the same brain. Pillai's trace was reported to be the MANOVA test statistic.

Statistics in studies **II** and **III** were rectified for multiple comparisons utilizing the Benajmini-Hochberg false discovery rate (FDR) method and a *q*-value (*p*-value adjusted for FDR) less than 0.05 was the threshold established for statistical significance (Benjamini & Hochberg, 1995).

5 RESULTS

5.1 SUSCEPTIBILITY VARIATIONS AFTER SEVERE TBI (STUDY I)

Most dramatic tissue changes post-trauma were exhibited at -3.80 mm from bregma (**Figure 7G-L**), corresponding to the epicenter of the primary lesion. More specifically, the ipsilateral side in several brain regions including the perilesional cortex, the thalamus demonstrated extensive degeneration, and the ipsilateral ventricle also showed a drastic increase in size. Moreover, the secondary damage also extended to areas distal from the lesion site at, -1.80 mm from bregma (**Figure 7A-F**).

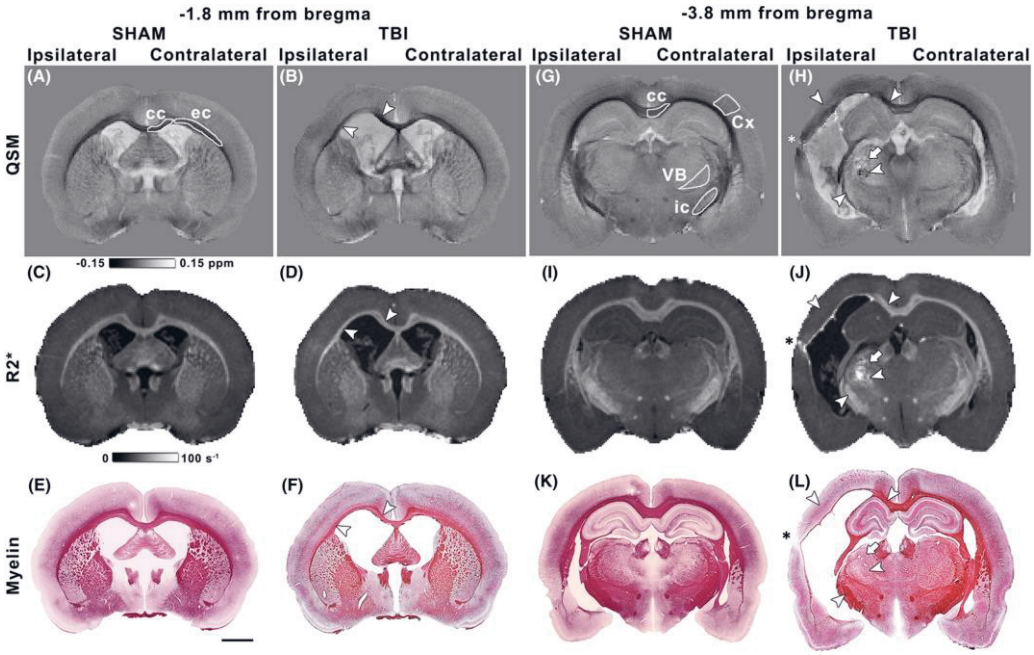

Figure 7. Representative QSM maps (A, B, G, H), R_2* maps (C, D, I, J) and myelin-stained sections (E, F, K, L) from a sham-operated and a TBI rat at −1.8 mm (A-F) and −3.8 mm (G-L) from the bregma. The white arrowheads indicate variations in susceptibility or relaxation rates. Myelin stainings were analysed in selected ROIs (white outlines in A and G). The white arrow (H, J, L) points to a thalamic calcification. The asterisk indicates the core of the primary lesion. Scale bar: 2 mm. Abbreviations: cc, corpus callosum; Cx,

perilesional cortex; ec, external capsule; ic, internal capsule; VB, ventrobasal complex. Reproduced with permission from (Chary, et al., 2020), *NMR in biomedicine, 34*(2), e4438.

5.1.1 Secondary tissue changes distal from the lesion site

In sTBI rats, the ipsilateral corpus callosum demonstrated a significant decrease in tissue susceptibility versus the contralateral side (p = 0.00078) and also when compared ipsilaterally (p = 0.0186) to sham-operated rats. In the external capsule, changes were insignificant in TBI rats when compared to sham-operated, even though, increased susceptibility was observed in some individual rats. In relation to R_2*, no significant differences were observed in the corpus callosum, while the R_2* values were significantly lower ipsilaterally (p = 0.0156) in TBI rats when compared contralaterally in the external capsule.

In histology, the Nissl-stained sections showed increased gliosis in both areas in TBI rats (**Figure 8A, 3B, 8K, and 8L**), more apparent in the deeper aspects of the corpus callosum and spread throughout the bundle in the external capsule (**Figure 8L**). The myelin-stained sections demonstrated reduced thickness in both these areas indicative of loss of myelinated axons (**Figure 8D and 8N**). However, the deeper aspects of the ipsilateral corpus callosum in the TBI rats appeared denser. Finally, iron accumulation in the form of small and widespread deposits were observed in the ipsilateral corpus callosum and external capsule, respectively (**Figure 8E, 8F, 8O and 8P**).

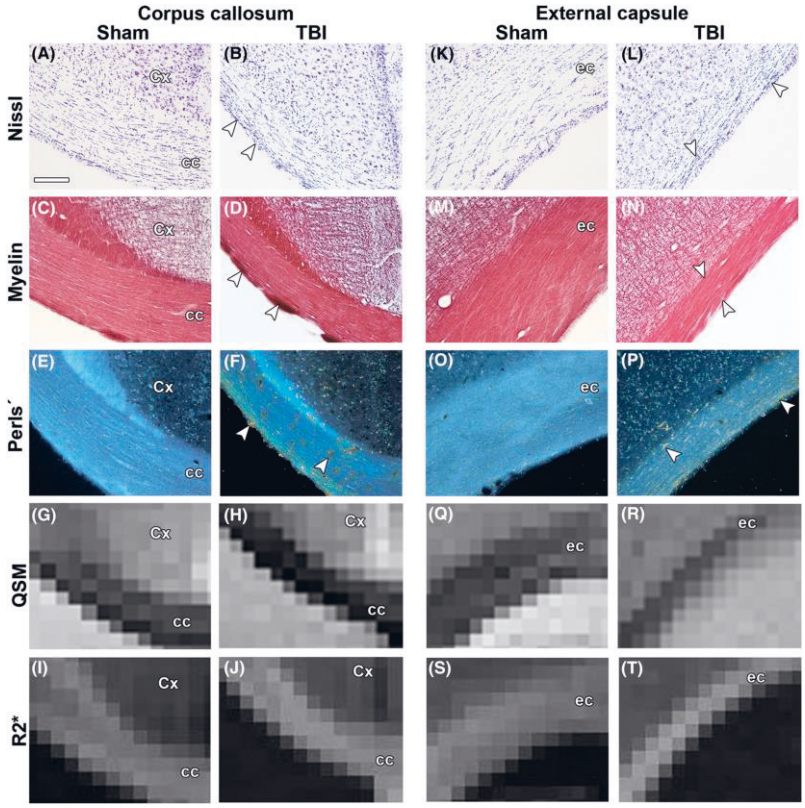

Figure 8. Representative photomicrographs of the ipsilateral corpus callosum (A-F) and external capsule (K-P) of a sham-operated and a TBI rat at −1.8 mm from the bregma. The histological sections are from the same animals and level as shown in Figure 7. The white arrowheads point to increased cell density in Nissl-stained sections, increased/decreased myelin in myelin-stained sections, and iron accumulation in Perls'-stained sections. Scale bar: 150 µm. Detail of the QSM maps and R_2* maps of the ipsilateral corpus callosum (G-J) and external capsule (Q-T) of a sham-operated and a TBI rat at −1.8 mm from the bregma. Abbreviations: cc, corpus callosum; Cx, cortex; ec, external capsule. Reproduced with permission from (Chary, et al., 2020), *NMR in biomedicine, 34*(2), e4438.

5.1.2 Secondary tissue changes proximal to the lesion site

The internal capsule and ventrobasal complex were first investigated at the level of the primary injury. In the ipsilateral internal capsule, TBI rats demonstrated higher susceptibility values (p = 0.0234) and lower R_2* rates

(p = 0.0078) as compared the contralateral side. In histology, TBI rats showed gliosis in the area (**Figure 9A-B**), and considerable loss of myelinated axons indicating reduced myelin density (**Figure 9C-D**). Additionally, there were minute amounts of iron deposits dispersed in the structure ipsilaterally in TBI rats (**Figure 9E-F**).

The ventrobasal complex is an area that exhibited the presence of both strongly paramagnetic and diamagnetic sources of susceptibility ipsilaterally in TBI rats (**Figure 7G-H**). Increase in tissue susceptibility was observed in most TBI animals ipsilaterally, and higher R_2* rates were observed when compared to the contralalateral side (p = 0.0078), and as compared to the ipsilateral side in the sham-operated (p = 0.0016). Histology demonstrated the complex pathology due to underlying tissue changes in the thalamus, emanating from the presence of gliosis (**Figure 9L**), substantial loss of myelinated axons (**Figure 9N**) in the several crossing fiber bundles observed in the area. Additionally, the area also showed iron accumulation which were both wide-spread and highly concentrated and the co-localized presence of calcifications (**Figure 9N and 9P**) with opposing influence on tissue susceptibility.

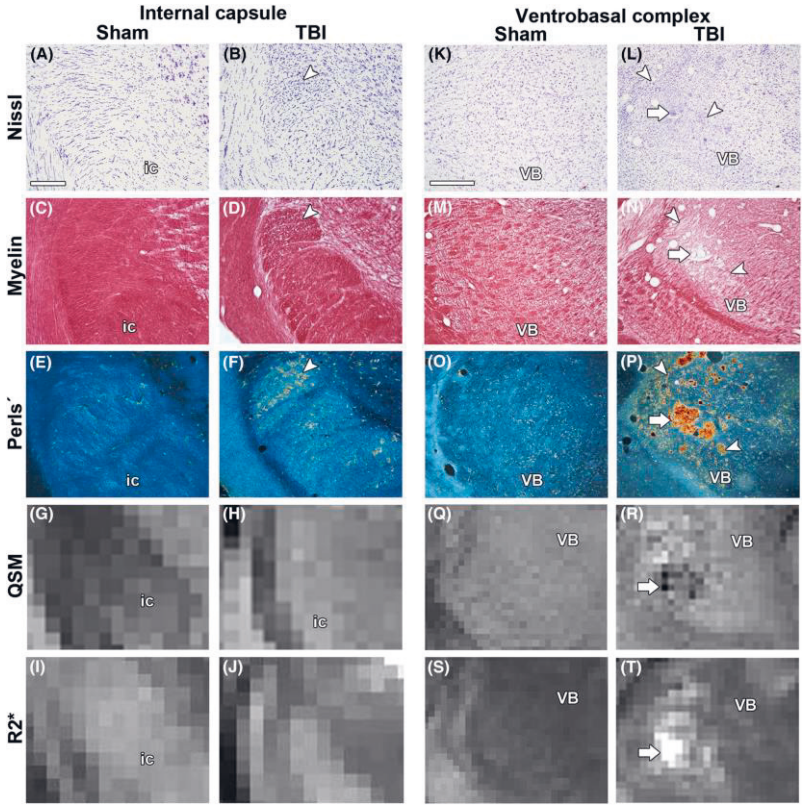

Figure 9. A-F, K-P, Representative photomicrographs of the ipsilateral internal capsule (A-F) and ventrobasal complex (K-P) of a sham- operated and a TBI rat at −3.8 mm from the bregma. The histological sections are from the same animals and level as shown in Figure 7. The white arrowheads point to increased cell density in Nissl-stained sections, increased/decreased myelin in myelin-stained sections, and iron accumulation in Perls'-stained sections. The white arrow indicates a calcification. Scale bars: 150 µm (A-F) and 400 µm (K-P). G-J, Q-T, Detail of the QSM maps and R_2* maps of the ipsilateral internal capsule (G-J) and ventrobasal complex (Q-T) of a sham-operated and a TBI rat at −3.8 mm from the bregma. Abbreviations: ic, internal capsule; VB, ventrobasal complex. Reproduced with permission from (Chary, et al., 2020) *NMR in biomedicine, 34*(2), e4438.

In addition, two other areas were investigated in close proximity to the primary lesion: the perilesional cortex and the corpus callosum. The ipsilateral perilesional cortex in TBI rats showed significantly reduced

susceptibility values when compared contralaterally (p = 0.0391). Significantly reduced R_2* values were also observed ipsilaterally in the TBI rats (p = 0.0156) as compared to the contralateral side. In histology, the Nissl-stained sections demonstrated gliosis throughout the cortical layers ipsilaterally in TBI rats, and myelin loss and iron presence throughout the cortex, but most extensively in layer VI.

In the corpus callosum, differences in tissue susceptibility were insignificant between TBI and sham-operated rats, both ipsi- and contralaterally. The R_2* rates increased in TBI rats ipsilaterally (p = 0.078) as compared to the contralateral hemisphere. In histology, the deep aspects of the ipsilateral corpus callosum showed the most pronounced changes including gliosis, reduced myelin density, and dense iron deposition.

5.2 MICROSTRUCTURAL CHANGES AFTER MILD TBI (STUDY II)

mTBI rats exhibited most dramatic changes at approximately -3.50 mm from bregma, the epicenter of the primary lesion when compared rostrally (approximately -1.80 mm from bregma). The secondary damage also extended to connected brain regions at 35 days post-initial injury (**Figure 10**).

5.2.1 Whole-brain group analyses of dMRI measures

The whole-brain group analysis revealed significant decreases in several DTI-, CSD- and NODDI-derived parameters including FA, AD, FD, FC, FDC, and ODI in mTBI rats as compared to shams (TFCE, p-value < 0.05, FWE-corrected) (**Figure 10**). More specifically, FA, FD, and FDC significantly decreased in TBI rats throughout the brain in both WM and GM areas. Besides, TBI rats exhibited significantly increased ODI in regions close to the primary lesion which mainly included the WM, and thalamic areas, with similar changes also observed in the FA, FD, FDC metrics. Changes in AD were resticted to a few voxels in the mid brain, while significantly reduced FC was also restricted to few damaged areas as shown in **Figure 10**.

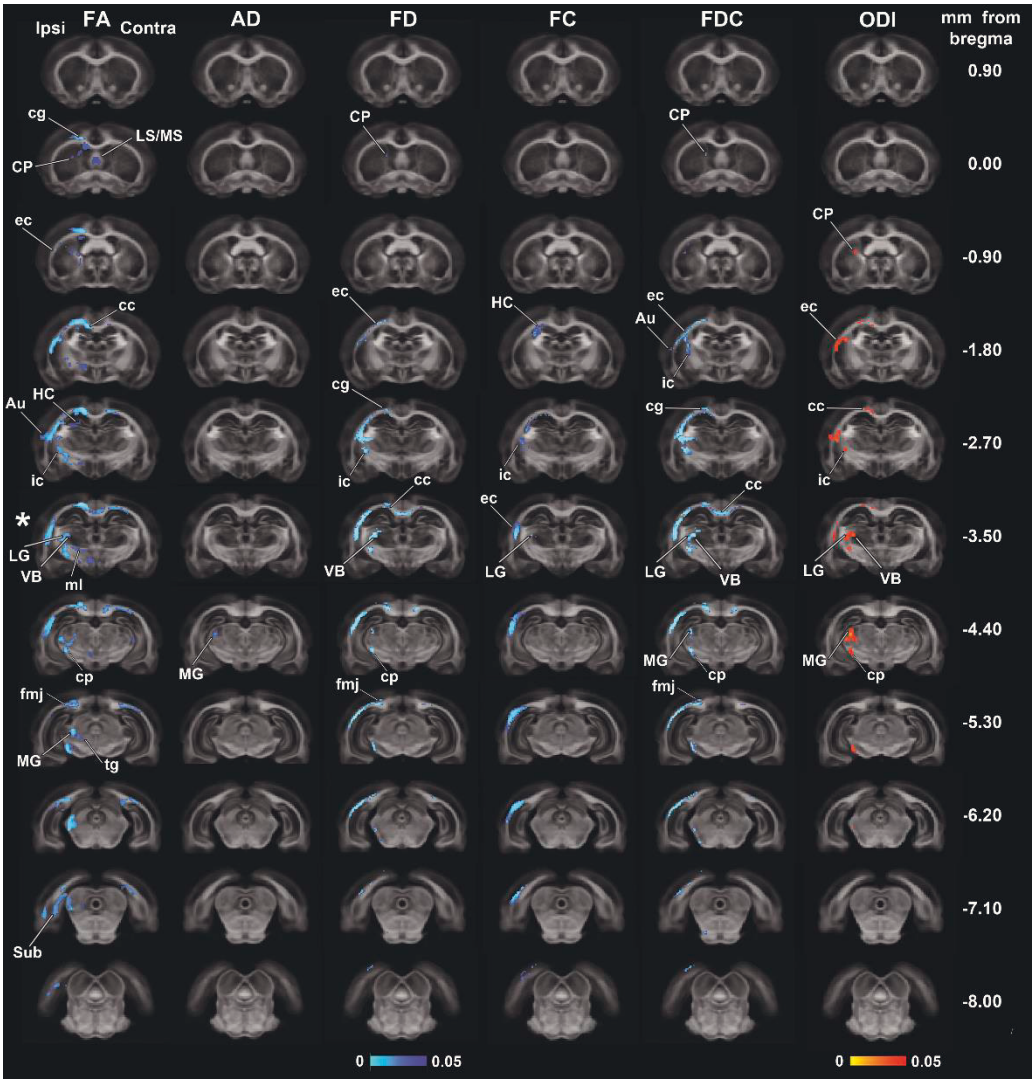

Figure 10. Whole-brain group differences in FA, AD, FD, FC, FDC, and ODI metrics when comparing sham-operated and mTBI rats after 35 days of the sham-operation or injury. Areas displaying significant group differences in mTBI versus sham-operated rats (TFCE, p-value < 0.05, FWE-corrected) are overlaid on the FOD-based template. Significances are displayed as voxels in a light-dark blue scale, representing mTBI group values lower than sham-operated group values, and in a red-yellow scale, representing mTBI group values higher than sham-operated group values. The asterisk shows the epicenter of the lesion. Au, auditory cortex; cc, corpus callosum; cg, cingulum; cp, cerebral peduncle; CP, caudate putamen; ec, external capsule; fmj, forceps minor of the corpus callosum; HC, hippocampus; ic,

internal capsule; LG, lateral geniculate nuclei; LS/MS, lateral/medial septal nucleus; MG, medial geniculate nucleus; ml, medial lemniscus; Sub, subiculum; tg, tegmental nuclei; VB, ventrobasal complex. Reproduced from (Chary et al., 2021), *Frontiers in neuroscience*, *15*, 746214 under the Creative Commons Attribution 4.0 (CC-BY, v4.0) International License.

5.2.2 Qualitative histology

mTBI rats exhibited microstructural alterations in the form of axonal injury and/or loss of myelinated axons (**Figure 11B'-H'**) and gliosis (**Figure 12 B'-H'**) in all the brain regions that revealed differences in the whole-brain group analysis. Extensive axonal alterations were observed rostrally in brain areas including the caudate putamen (**Figure 11B'**), cortex (**Figure 11E'**), and ventrobasal complex (**Figure 11H'**). Decreased myelin density was observed in the internal capsule (**Figure 11C'**), external capsule (**Figure 11D'**), auditory cortex (**Figure 11E'**), and stratum lacunosum-moleculare (**Figure 11G'**). In the corpus callosum, axonal alterations were observed both ipsi- and contralaterally along the fiber bundle and a less pronounced decrease in axonal density (**Figure 11F'**) as compared to the other brain areas. Thinning of the fiber bundles in the internal capsule was also observed rostrally (**Figure 11C'**).

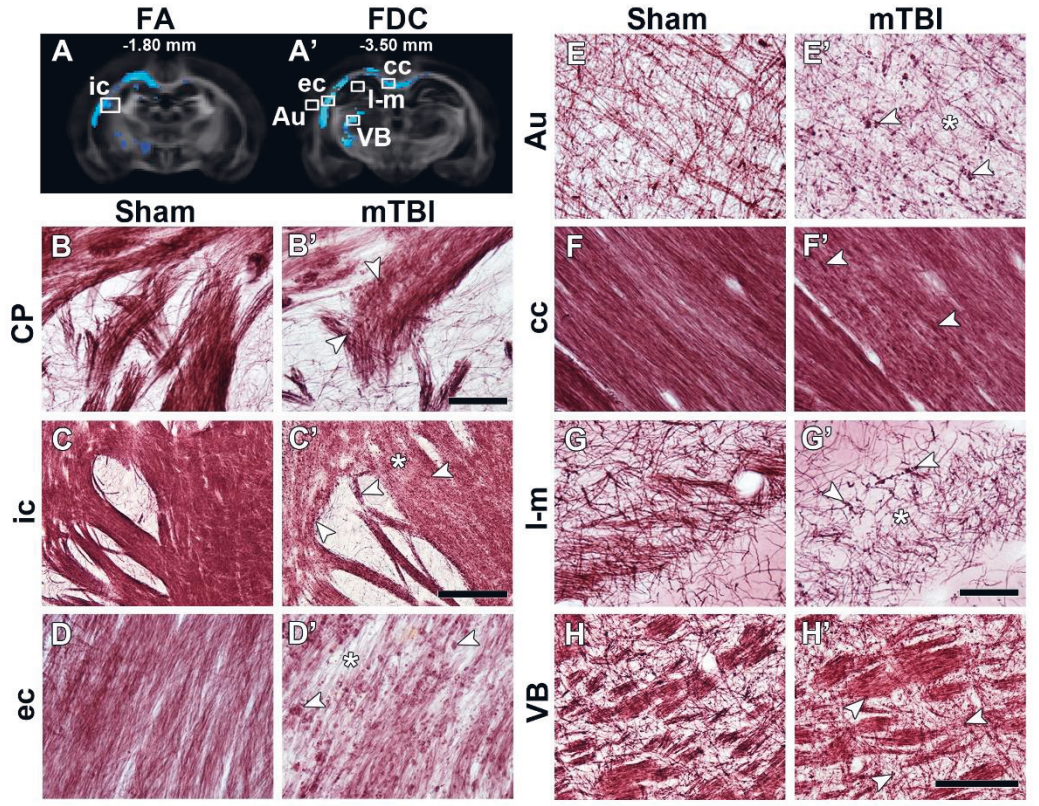

Figure 11. FA (A) and FDC (A') at –1.80 and –3.50 mm from bregma, respectively, from the group analyses. White squares indicate the location of the photomicrographs shown in (B–H). Representative photomicrographs of myelin-stained sections of a sham-operated and a mTBI rat from the caudate putamen (B,B') from –0.90 mm (not shown in A), internal capsule (C,C') from –1.80 mm, and external capsule (D,D'), auditory cortex (E,E'), corpus callosum (F,F'), stratum lacunosum-moleculare (G,G'), and ventrobasal complex (H,H') from –3.50 mm from bregma. White arrowheads point at myelin alterations associated with axonal damage and asterisks indicate areas with extensive decrease in density of myelinated axons. Au, auditory cortex; cc, corpus callosum; CP, caudate putamen; ec, external capsule; ic, internal capsule; l-m, stratum lacunosum-moleculare; VB, ventrobasal complex. Scale bars: 50 mm (B,B',D,D'–G,G'), 150 mm (H,H'), and 250 mm (C,C'). Reproduced from (Chary et al., 2021), *Frontiers in neuroscience*, *15*, 746214 under the Creative Commons Attribution 4.0 (CC-BY, v4.0) International License.

Nissl-stained sections revealed a widespread increase in cellularity extending rostrally (**Figure 12**), which was more pronounced in areas close to the primary lesion including the corpus callosum (**Figure 12F'**), external capsule (**Figure 12D'**), cortex (**Figure 12E'**), internal capsule (**Figure 12C'**), and ventrobasal complex (**Figure 12H'**). Finally, increased cellularity (**Figure 12G'**) was observed in the stratum lacunosum-moleculare combined with loss of fiber bundles (**Figure 12G'**) in the area.

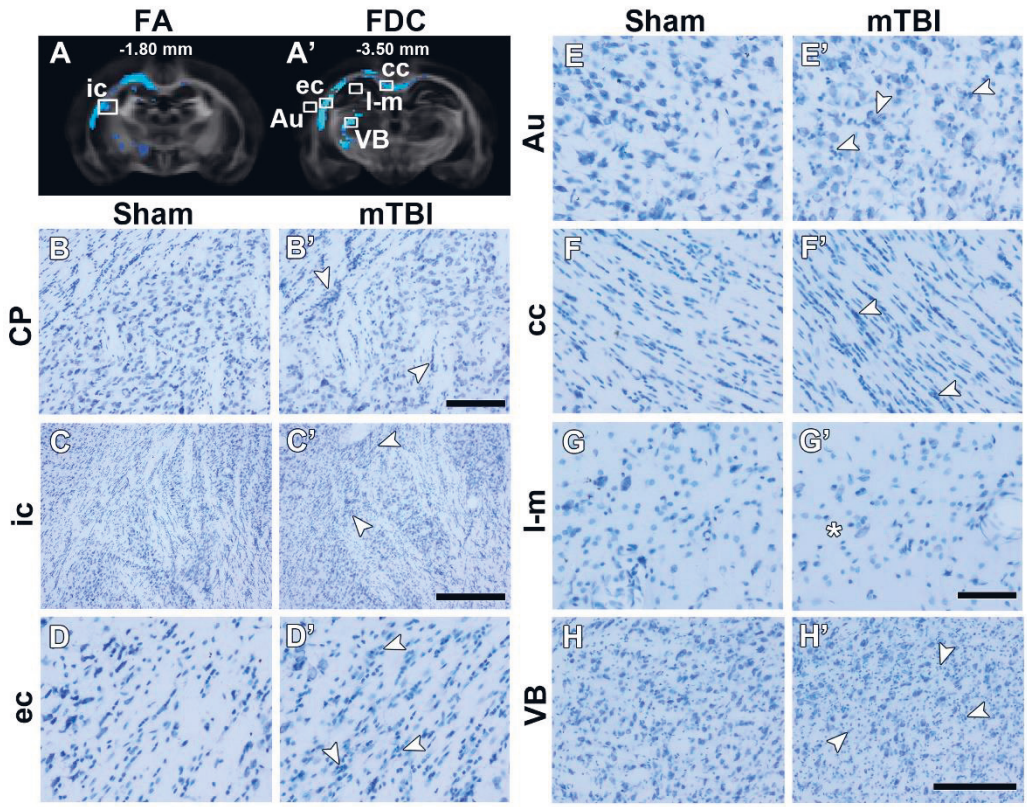

Figure 12. FA (A) and FDC (A') at –1.80 and –3.50 mm from bregma, respectively, from the group analyses. White squares indicate the location of the photomicrographs shown in (B–H). Representative photomicrographs of Nissl-stained sections of a sham-operated and a mTBI rat from the caudate putamen (B,B') from –0.90 mm (not shown in A), internal capsule (C,C') from –1.80 mm, and external capsule (D,D'), auditory cortex (E,E'), corpus callosum (F,F'), stratum lacunosum-moleculare (G,G'), and ventrobasal complex (H,H') from –3.50 mm from bregma. White

arrowheads point at gliosis alterations associated with axonal damage and asterisk indicates less cell density. Au, auditory cortex; cc, corpus callosum; CP, caudate putamen; ec, external capsule; ic, internal capsule; l-m, stratum lacunosum-moleculare; VB, ventrobasal complex. Scale bars: 50 mm (B,B',D,D'–G,G'), 150 mm (H,H'), and 250 mm (C,C'). Reproduced from (Chary et al., 2021), *Frontiers in neuroscience*, *15*, 746214 under the Creative Commons Attribution 4.0 (CC-BY, v4.0) International License.

5.2.3 Correlation of dMRI and histology measures

ROI analyses of conventional and advanced dMRI measures showed signifcant differences in several regions post-mild injury and also, demonstrated good correspondence with histology (**Table 1**).

Table 1. Pearson's correlations of dMRI and histology measures with co-efficient (*R*) and *q*-values (*q*).

Level	**-1.80 mm from bregma**	**-3.50 mm from bregma**			
Region	**ec**	**cc**	**ec**	**ic**	**VB**
Metric	**CD**	**AI**	**AI**	**CD**	**CD**	**AI**
FA *(R, q)*	(-0.333, 0.187)	(0.429, 0.075)	**(0.737, 9.623 x 10^{-5***})**	**(-0.712, 2.235 x 10^{-4***})**	(-0.344, 0.172)	(-0.333, 0.187)
RD (*R*, *q*)	**(0.474, 0.044*)**	**(-0.544, 0.014*)**	(-0.410, 0.093)	(0.434, 0.071)	(0.347, 0.168)	(0.119, 0.738)

Peak (*R*, *q*)	(-0.181, 0.573)	(0.329, 0.193)	**(0.781, 1.588 x 10^{-5***})**	**(-0.695 3.656 x 10^{-4***})**	(-0.189, 0.551)	(-0.383, 0.123)
FD (*R*, *q*)	(-0.423, 0.081)	(0.105, 0.768)	**(0.473 0.044*)**	**(-0.491, 0.034*)**	**(-0.571, 0.008**)**	(-0.302, 0.248)
FC (*R*, *q*)	(-0.147, 0.660)	(-0.125, 0.725)	(0.324, 0.201),	(-0.261, 0.342)	(-0.416, 0.087)	**(-0.467, 0.048*)**
FDC (*R*, *q*)	(-0.413, 0.090)	(0.177, 0.588)	**(-0.492, 0.034*)**	**(-0.505, 0.027*)**	**(-0.580, 0.007**)**	(-0.374, 0.133)
ODI (*R*, *q*)	(-0.042, 0.912)	(-0.089, 0.791)	**(-0.753, 4.780 x 10^{-5***})**	**(-0.709, 2.100 x 10^{-4***})**	(0.200, 0.515)	(0.434 ,0.071)

Numbers in bold indicate the correlations significantly different from zero: *q < 0.05; **q < 0.01; ***q < 0.001. AD, axial diffusivity; AI, anisotropy index; cc, corpus callosum; CD, cellular density; Disp, dispersion; ec, external capsule; FA, fractional anisotropy; FC, fiber bundle cross-section; FD, fiber density; FDC, fiber density and fiber bundle cross-section; FWF, free water fraction; ic, internal capsule; MD, mean diffusivity; NDI, neurite density index; ODI, orientation dispersion index; RD, radial diffusivity; VB, ventrobasal complex.

5.3 MICROSTRUCTURAL COMPLEXITY AFTER SEVERE TBI (STUDY III)

5.3.1 dMRI measures in detecting WM microstructural complexity

In the corpus callosum, TBI rats exhibited significantly decreased FA ipsi- (q = 0.002) and contralaterally (q = 0.008) when compared to sham-operated, and significantly decreased RD ipsi- (q = 0.005) and contralaterally (q = 0.004). In the internal capsule, significantly reduced FA (q = 0.015) and increased RD were observed ipsilaterally (q = 0.028) in sTBI rats as compared to sham-operated.

With regards to fixel-based measures, significantly decreased AFD was observed in the corpus callosum ipsi- (q = 0.008) and contralaterally (q = 0.006) in sTBI rats when compared to sham-operated. Significantly reduced peak FOD amplitudes and primary fiber bundle density was observed in sTBI rats ipsi- (q = 0.010, q = 0.006) and contralaterally (q = 0.010, q = 0.006). A significant decrease was also observed ipsilaterally (q = 0.010) in sham-operated rats when compared to contralateral side.

In relation to the 3-tissue signal fraction maps, sTBI rats exhibited lower T_W, and distinctly higher T_G and T_p, ipsi- and contralaterally in the corpus callosum when compared to sham-operated. Statistical analyses of the isometric log-ratios revealed significant differences ipsilaterally in sTBI rats when compared to sham-operated (Pillai's trace = 0.754, q = 0.015) and also contralaterally (Pillai's trace = 0.815, q = 0.011). sTBI rats also demonstrated lower T_W and higher T_G in the internal capsule ipsilaterally when compared to sham-operated, and a significant difference was found contralaterally when compared to shams (Pillai's trace = 0.767, q = 0.024).

5.3.2 dMRI measures in detecting GM microstructural complexity

In GM, the stratum lacunosum-moleculare was the only area which demonstrated senstivity to DTI parameters with significantly reduced FA observed in sTBI rats contralaterally (q = 0.009) when compared to the ipsilateral hemisphere, and when compared contralaterally to sham-

operated rats (q = 0.008). In this context, fixel-based parameters demonstrated more changes as compared to DTI parameters. Contralaterally, significantly decreased AFD and primary fiber density was observed in sTBI rats when compared to the ipsilateral side (q = 0.014), and (q = 0.011), and significantly decreased AFD (q = 0.017), peak FOD amplitudes (q = 0.030), and primary fiber bundle density q = 0.011) were observed as compared to sham-operated rats.

In the ventrobasal complex, significantly increased AFD was observed ipsilaterally (q = 0.010) in sham-operated rats as compared to the contralateral side, and significantly decreased primary fiber bundle density was observed ipsi- and contralaterally in sTBI rats (q = 0.012).

In relation to the 3-tissue signal fraction maps, the ventrobasal complex in sTBI rats showed higher T_W ipsilaterally as compared to sham-operated. A significant difference was observed ipsilaterally between sTBI and sham-operated rats (Pillai's trace = 0.734, q = 0.019), and between ipsi- and contralateral sides in the sham-operated rats (Pillai's trace = 0.914, q = 0.009). In the stratum lacunosum-moleculare, sTBI rats exhibited higher T_W as compared to the contralateral side and a significant difference was observed ipsi-contralaterally in sTBI rats (Pillai's trace = 0.734, q = 0.010) and contralaterally when comparing sTBI and sham-operated rats (Pillai's trace = 0.655, q = 0.048).

5.3.3 Qualitative histology

In the corpus callosum, there was sparse loss of myelin in the deeper aspects (**Figure 13a2**), and dorsally in the internal capsule (**Figure 13d2**). Both areas also exhibited the presence of gliosis along the structure (**Figure 13a4 and 13d4**). In GM areas, the somatosensory cortex and stratum lacunosum-moleculare exhibited extensive loss of myelinated axons and gliosis (**Figure 13b2 and 13b4**), which was less severe in the molecular layer of the dentate gyrus (**Figure 13c2 and 13c4**). Finally, there was thinning of the myelinated fiber bundles, accompanied with substantial neuronal loss and gliosis in the ventrobasal complex (**Figure 13e2 and 13e4**).

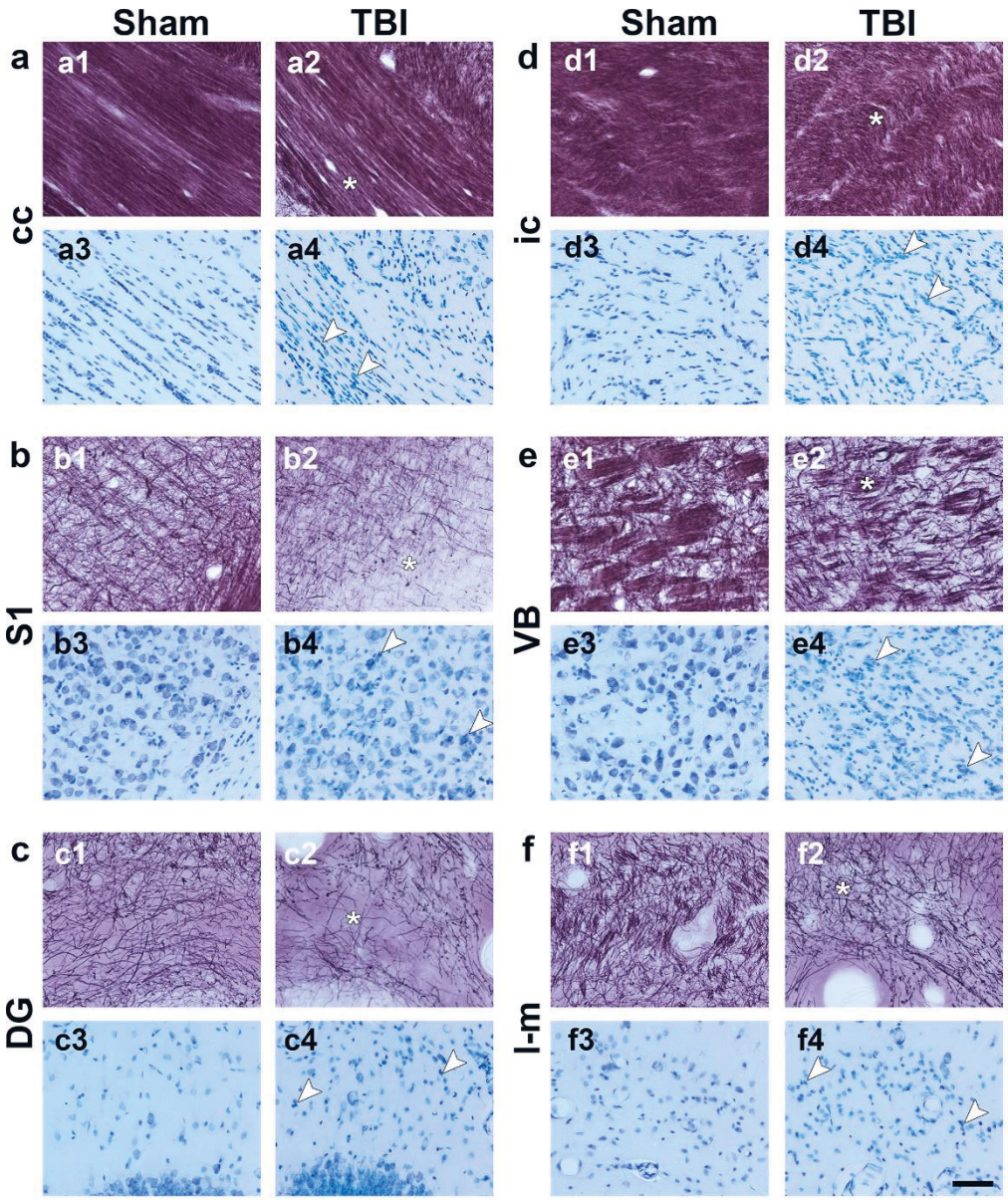

Figure 13. Representative photomicrographs of Nissl and myelin stainings from a sham-operated and a sTBI rat. Asterisks indicate a decrease in myelin density and arrowheads increased cell density (small and intense blue cells) associated to gliosis. Abbreviations: cc, corpus callosum; DG, dentate gyrus; ic, internal capsule; l-m, stratum lacunosum-moleculare; S1, primary somatosensory cortex; VB, ventrobasal complex. Scale bar: 50 µm. Manuscript Submitted.

5.3.4 Thalamocortical damage post-TBI

The streamlines generated along the thalamocortical tract demonstrated changes in orientation from dorso-ventral to rostro-caudal in sTBI rats ipsilaterally when compared to sham-operated (**Figure 14**). At -3.80 mm from bregma corresponding to the epicenter of the primary lesion, orientational changes were observed in the streamlines along the external capsule (**Figure 14c-d**). Distant to the lesion site at -1.80 mm from bregma, more pronounced orientational changes were observed in the streamlines originating from the thalamus into the perilesional cortex (**Figure 14c-d**).

Quantitative analyses of the streamlines revealed significantly reduced average pathlengths and curvature ipsilaterally (q = 0.004, q = 0.012) in sTBI rats as compared to sham-operated, and ipsi-contralaterally in sTBI rats (q = 0.004, q = 0.008) (**Figure 14e-f**).

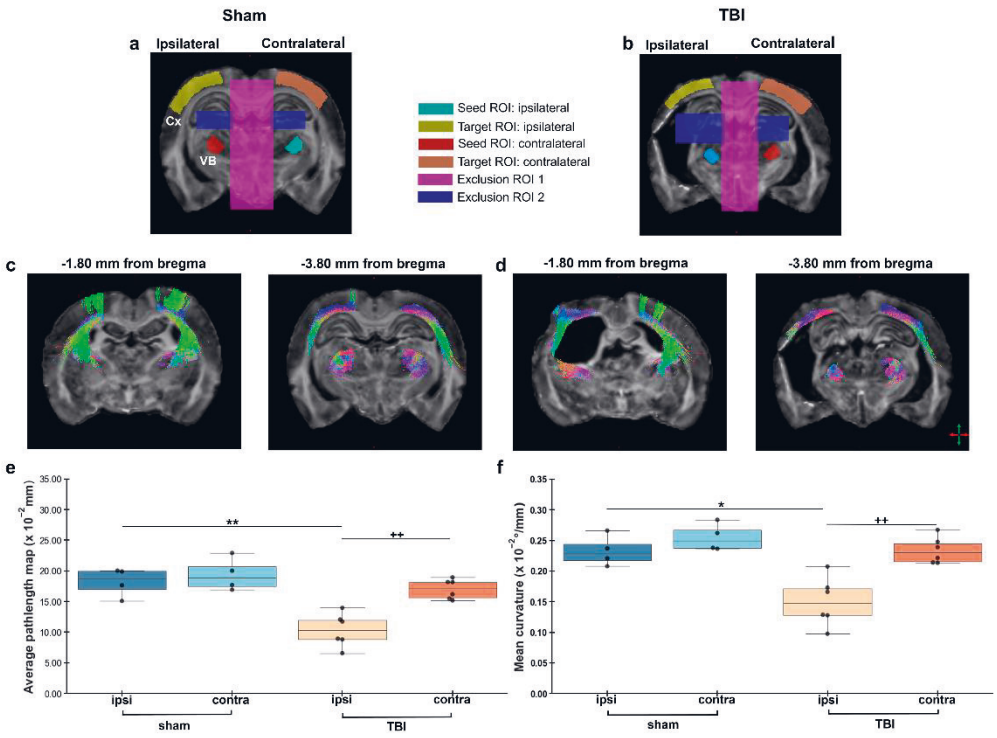

Figure 14. Targeted tractography. Probabilistic streamlines were generated using a combination of seed, target, and exclusion ROIs in sham-operated (a) and TBI (b) rats. 2D reconstruction of the thalamocortical pathway in a

representative sham and TBI rat at -1.80 mm and -3.80 mm from bregma (c, d), colors indicate directionality: red, medio-lateral; green, dorso-ventral; blue, rostro-caudal. Track-weighted measures of average pathlength map and mean curvature computed from the generated tractograms (e, f). Results are shown as minimum, lower quartile, median, upper quartile and maximum, and paired t-test comparing ipsi- and contralateral sides within animals (*q < 0.05, **q < 0.01) or unpaired t-test comparing the same hemisphere between sham-operated and TBI rats (^{++}q < 0.01) which are FDR corrected. Abbreviations: Cx, perilesional cortex; VB, ventrobasal complex. Manuscript Submitted.

6 DISCUSSION

This thesis demonstrated that the use of advanced quantitative MRI methodologies is essential in underpinning the varying pathological features of the secondary tissue damage post-TBI. At the chronic phase post-severe injury, study **I** showed quantitative variations in susceptibility contrast to be more sensitive in unravelling the different susceptibility sources such as iron and calcifications close to the lesion site, and more so, to changes distal from the lesion site as compared to R_2*, which provided complimentary information in some cases. Furthermore, considering DTI is the gold standard to assess tissue microstructure, particularly in the sub-acute and acute phases post-mild injury (Edlow et al., 2016), study **II** showed that the combination of conventional and advanced dMRI approaches is warranted to provide a more comprehensive overview of the underlying microstructural changes due to axonal damage and gliosis in both WM and GM regions. At the chronic phase post-severe injury, study **III** demonstrated that advanced dMRI metrics such as 3-tissue signal fractions can provide more specificity than conventional DTI to WM changes, which were reflective of the magnitude of tissue damage microstructurally and demonstrated the crucial need for the inclusion of bespoke analyses approaches such as TWI to fully gauge tract integrity post-injury, which may be unfeasible by conventional analyses.

6.1 ASSESSING WM POST-SEVERE INJURY

In study **I**, dense iron deposits were observed particularly in the deep aspects along the ipsilateral corpus callosum and external capsule. These findings were consistent with previous studies, which have reported the severe LFPI to produce bleeds along these structures adjacent to the primary injury site (Dietrich et al., 1994; Laitinen et al., 2015; Okubo et al., 2013). Moreover, these dense iron deposits several micrometers in

diameter induced very strong paramagnetic microscopic alterations in tissue susceptibility, which were consistent with increased R_2* rates.

DTI findings in the ipsilateral corpus callosum and internal capsule in study **III** showed good correspondence with studies reported previously (Laitinen et al., 2015). However, the slightly contrasting patterns of the 3-tissue signal fractions provided more specificity reflecting either more or less severe loss of myelinated axons and gliosis. Although, there are no previous studies in TBI for a direct comparison, similar findings were observed when characterizing microstructural heterogeneity associated with white matter lesions in patients with Alzheimer's disease (Mito et al., 2020) or stroke (Khan et al., 2020). More specifically, the authors reported periventricular WM hyperintensities, which are histologically characterized with considerable axonal loss, and gliosis (Fazekas et al., 1991, 1993; Schmidt et al., 2011), exhibited markedly higher T_c. On the contrary, the deep WM hyperintensities which are associated with less severe damage and gliosis (Fazekas et al., 1991, 1993; Schmidt et al., 2011), exhibited variations in all the 3-tissue signal profiles, instead of a marked increase in T_c alone. These findings suggest that the distinct variations observed in these 3-tissue signal fractions in WM strongly reflect tissue damage and could be potentially utilized as a quantitative marker to detect early pathological changes among patients with brain injury, as well in follow-ups that might lead to better patient outcomes.

Distal from the lesion site, the ipsilateral corpus callosum in study **I** demonstrated an unexpected finding. Susceptibility variations in the area were influenced by the increased diamagnetic myelin content over the strong paramagnetic effects of iron, which was observed in the form of small deposits. In addition, the external capsule exhibited the presence of widespread iron deposits, as compared to dense deposits, which were observed proximal to the primary lesion. Differences underlying pathological tissue in WM at the chronic phase post-severe injury have been described previously (Huttunen et al., 2018). Although, decreased R_2* rates suggested that myelin loss dominated the dispersed iron presence in the structure, caution must be excised as the R_2* contrast has several confounding factors as opposed to QSM such as water content, structure,

and orientation of myelin (Chappell et al., 2004; Cherubini et al., 2009; Li et al., 2012, 2016; Rudko et al., 2014; Wisnieff et al., 2015). In the ipsilateral thalamocortical tract, TWI measures in study **III** demonstrated more pronounced changes rostral to the primary injury site. These findings are reflective of the extent of the degeneration along the tract, post-severe injury. Previously, (Wright et al., 2017) detected reduced curvature, and average pathlengths in the corticospinal tract indicating degeneration of the tract ipsilaterally following LFPI in rats, at the chronic phase. These findings amongst others (Wright et al., 2016; 2017, 2021; Zamani et al., 2021) have demonstrated TWI measures in revealing widespread decreases in average pathlengths, mean curvature and track densities to be more sensitive to WM changes than conventional DTI, post-injury. More importantly, these findings highlight the promise of TWI-based measures as a quantitative marker in detecting alterations in WM tracts post-injury, which are not detectable by other dMRI approaches.

6.2 ASSESSING WM POST-MILD INJURY

Post-mild injury, several studies have explored the sensitivity of DTI to detect microstructural tissue changes in WM (Bennett et al., 2012; Herrera et al., 2017; Hutchinson et al., 2018; Hylin et al., 2013). Changes observed in these studies were attributed to axonal damage and gliosis which were mostly detected as decreased FA, and AD and increased RD (Hylin et al., 2013; mac Donald et al., 2007; San Martín Molina et al., 2020). DTI findings in study **II** were consistent with those reported previously. However, utilizing quantitative histology further enhanced our understanding of these changes that exhibited good correspondence between the dMRI measures and histology, which were attributed with increased cell density and loss of myelinated fiber bundles. More specifically, in the corpus callosum and external capsule, the positive association exhibited between DTI metrics including FA, AD and AI were indicative of axonal damage and/or axonal loss, while the negative association observed between FA and CD in the external capsule was associated to axonal damage in

combination with a significant increase in cellularity. Although, CSD-derived metrics also detected changes in both these areas that exhibited significant tissue damage, only changes in the external capsule showed good correspondence with quantitative histology. These findings, thereby reinforce the continued use of conventional DTI measures in investigating mild trauma, and the combined use of conventional and advanced dMRI for deriving more information as well as an enhanced comprehension of the tissue damage after mild injury.

In addition to CSD, multi-compartmental NODDI was also incorporated in study **II**. However, changes were only detected in ODI in areas with decreased FA including the corpus callosum and internal capsule, which was also demonstrated previously (Jespersen et al., 2012; Zhang et al., 2012). Moreover, given the changes observed in histology post-mild injury, we also expected other parameters such as NDI and FWF also to be sensitive to the tissue changes. However, it has been shown that FWF measures have high variance and low reproducibility at 9.4 T, thereby, requiring a considerably larger sample size to detect biological changes in these parameters (McCunn et al., 2021) post-mild injury. While the lack of changes detected in NDI could be hypothesized to the magnitude of axonal loss observed in a mildly injured brain, which is expected to be far less as compared to moderate or severe forms of injury.

Distal from the lesion site, fixel-based metrics detected more changes rostral to the injury site as compared to DTI. In this context, a previous study by Molina et al., 2020 at the sub-acute phase detected no changes using *in vivo* DTI distal from the lesion site. Although, caution must be exercised when comparing results obtained *in vivo* and *ex vivo*, these findings further reinforce the necessity for incorporating these advanced techniques, when assessing tissue microstructure post-mild injury.

6.3 ASSESSING GM POST-SEVERE AND MILD INJURY

In GM, the ventrobasal complex was an area that signified the complex pathophysiology post-TBI. In study **I,** there was a clear decrease in the

density of myelinated fiber bundles, and gliosis, combined with presence of iron and calcifications. Calcifications (Aggarwal et al., 2018; Lehto et al., 2012; Schweser et al., 2019) observed in the area were most likely linked to the activation of microglia (Gayoso et al., 2003), which contain hydroxyapatite resulting in their diamagnetic susceptibility. Moreover, in regions exhibiting co-localization of iron and calcium, the observed increase in susceptibility also demonstrated the dominating effect of paramagnetic iron over diamagnetic calcium. In this context, increase in R_2* rates resulting from iron and calcium deposition facilitated in distinguishing them in the ventrobasal complex and thereby, highlighted the use of incorporating histology in assessing the different factors influencing the magnetic susceptibility contrast.

Using DTI, a previous study (Laitinen et al., 2015) found significantly reduced RD in the ventrobasal complex in the TBI rats ipsilaterally which corresponded with thinning of the fiber bundles, loss of myelin, neurodegeneration, and calcifications (Lehto et al., 2012). Although, none of the DTI metrics were able to detect any changes in study **III**, significant changes were observed in the fixel-based metrics and 3-tissue signal fractions. More specifically, reduced FD observed in the area could be possibly attributed to the reduction in density of the fiber bundles. In addition, a previous study by (Grazioplene et al., 2018) have suggested that the loss in density of the primary fiber bundle also leads to secondary processes filling the space, mimicking the presence of crossing fibers in the microstructure. This causes restriction to the isotropic diffusion signal which manifests as an increase in the density of the secondary fiber bundle, also observed in study **II**. Although, the changes in the fixel-based measures could be reasonably explained with histology, the changes detected in the 3-tissue signal profiles were contradictory. In this case, the higher Tw observed was not reflective of an increase in the diffusion signal due to increased myelin content, but rather reflected contributions from secondary processes such as gliosis, and thereby requires careful interpretation.

We also investigated the sensitivity of dMRI to other GM regions post-severe injury including the stratum lacunosum-moleculare, dentate gyrus,

and perilesional cortex. Previously, (Laitinen et al., 2010) were unable to detect any changes in *ex vivo* DTI measures in the stratum lacunosum-moleculare, 6 months after sTBI. However, the authors observed orientational changes in the primary diffusion towards the mediolateral direction, which was associated with substantial loss of myelinated axons and increased gliosis. Moreover, increased DTI and SS3T-CSD metrics detected in study **III** suggest the increased diffusion anisotropy observed in the area was mostly associated with gliosis. In the dentate gyrus, neither conventional and advanced dMRI detected any changes, which could be reflective of the less severe myelin loss, and gliosis observed when compared to other GM regions investigated in the study. Finally, despite the proximity to the primary lesion site, the dMRI measures failed to detect any changes in the perilesional cortex in the ROI analysis. We hypothesized this lack of sensitivity to the multitude of trauma-related changes such as the variable atrophy in the cortex, crossing fiber presence, microstructural alterations including extensive myelin loss, neurodegeneration, or gliosis.

6.4 ADVANTAGES, LIMITATIONS, AND FUTURE PERSPECTIVES

It is also important to highlight the advantages, and limitations of the studies in this thesis, that might direct future research in the field.

6.4.1 Advantages

In study **I**, the corpus callosum and perilesional cortex adjacent to the lesion site were mostly affected by the microscopic susceptibility sources resulting from the old bleeds, but areas rostral to the lesion site were less influenced and thereby, demonstrated more sensitivity to tissue changes as compared to R_2*.

In study **II**, the multi-shell diffusion MRI enabled us to perform higher-order modelling using MSMT-CSD, and NODDI which provided complimentary information to DTI in assessing mTBI-related changes. In a similar context, combination of FBA and DTI has been used to study the effects of cognitive training on adolescents after moderate-to-severe TBI

(Verhelst et al., 2019), and the combination of NODDI and DTI has demonstrated better understanding of TBI-related WM alterations in the sub-acute and chronic phase in adults (Muller et al., 2021; Oehr et al., 2021).

SS3T-CSD utilized in study **III** is a time-efficient approach, which would enable the incorporation of other quantitative MRI measures such as R_2* and QSM to investigate other tissue alterations observed at the chronic phase after severe trauma, such as iron presence and/or calcifications. Furthermore, only utilizing averaged response functions from sham-operated rats ensured our interpretation of the findings remained clear of any bias to the underlying pathology. Finally, although, the low angular resolution achieved by the nominally used b-value can result in the underestimation of FODs *ex vivo* (Tournier et al., 2013), the accuracy and interpretation of the quantitative CSD measures can be deemed biologically meaningful when compared with higher b-value acquisitions (Calamuneri et al., 2018).

6.4.2 Limitations

With regards to limitations, QSM, is inherently ill-posed by nature, and secondly, is unable to fully resolve sub-voxel areas, which are associated with strong susceptibility sources. A typical example was the dense microscopic iron deposits observed in the external capsule and corpus callosum in study **I**. As a result, a combination of these issues caused streaking artefacts that extended beyond the susceptibility source into other regions resulting in an underestimation of their underlying tissue susceptibility. We employed different dipole inversion approaches based on literature to mitigate the effects of these streaking artefacts. Dipole inversion using the Tikhonov approach provided the best compromise between reduction of streaking artefacts and preservation of anatomical details. Nevertheless, the strong paramagnetic susceptibility contrast may provide useful information qualitatively about the nature of these iron deposits, and moreover, as QSM is a very rapidly evolving field, future acquisition, and post-processing approaches (Acosta-Cabronero et al.,

2018; Langkammer et al., 2018) may enable better resolution of these strong susceptibility sources.

Regarding limitations associated with dMRI, the protocol used in study **II** was incorporated with higher b-values than typically used to accommodate the decreased diffusivity in *ex vivo* tissues due to temperature, and chemical fixation (Rane & Duong, 2011; Sun et al., 2003; Wang et al., 2018; Wu et al., 2013). In spite of the high b-values used, differences still persist *ex vivo* due to the presence of immobile water hypothesized in the extra-axonal space (Stanisz et al., 1997; Veraart et al., 2019), which might remain un-attenuated. The single-shell protocol used in study **III** did not permit the application of other advanced modelling approaches such as multi-shell NODDI, which could have provided additional insights to infer tissue microstructural complexity post-severe TBI.

6.4.3 Future perspectives

In the context of future directions, all the studies in this thesis were performed *ex vivo*, which enabled us to acquire high-quality data required for successfully applying the advanced MRI tools for assessing TBI-related alterations. Future studies would be planned *in vivo* with the possibility of including multiple time-points with naïve animals (Chary et al., 2021; Chary et al., 2021; Lehto et al., 2012; Mohamed et al., 2021; Sierra et al., 2015; Stemper et al., 2015; Wright et al., 2017; Zamani et al., 2021), allowing monitoring of the TBI-related tissue changes over time, which in-turn would enable a clearer understanding of the TBI pathology and improved clinical translatability (Agoston et al., 2019). Moreover, future studies would also benefit with the inclusion of both males and females to better investigate the influence of gender-related differences post-trauma, and inform more individualized treatment strategies (Biegon, 2021; Gupte et al., 2019; Levin et al., 2021).

Although, the high-resolution susceptibility and dMRI maps in study **I** enabled assessment of complex susceptibility variations in the ventrobasal complex, future studies are warranted for evaluating the counteracting susceptibility mechanisms of iron and calcifications in pathological tissue.

Studies **II** and **III** may also warrant the inclusion of multiple response functions (de Luca et al., 2020) to accurately model different WM regions (Schilling et al., 2019) and GM anisotropy, which not only comprises of axons, but also dendrites and cell bodies (Jespersen et al., 2012; Palombo et al., 2020; Zhang et al., 2012). In this context, the inclusion of quantitative histology (Budde et al., 2011; Salo et al., 2021) and/or histological tract tracing (Harsan et al., 2013) would be beneficial to corroborate the quantitative MRI results.

Finally, we have applied quantitative MRI approaches in this thesis, and hypothesized them to be most sensitive to the varying features of the secondary tissue alterations post-trauma. However, considering the complex pathophysiology of TBI, a multi-modal approach might enable a more thorough comprehension of the underlying pathophysiology (Heffernan et al., 2013; Wiegand et al., 2022; Yang et al., 2021).

7 CONCLUSIONS

The global incidence of TBI requires precise evaluation of tissue changes both qualitatively and quantitatively to establish the injury severity, and provide suitable treatment. Therefore, this thesis focused on the application of advanced MRI techniques to assess the subtle secondary tissue changes post-TBI. Conventionally used MRI methods were utilized for the purpose of comparison. Coupled with comprehensive histology, this thesis was able to demonstrate the advantages, pitfalls, and limitations of these approaches. More specifically, this thesis showed that magnetic susceptibility variations in WM and GM areas post-injury were associated to reduction and/or loss of myelin, and presence of iron and calicifications. QSM allowed detection of secondary injury-related tissue changes rostral to the primary lesion, where R_2* values exhibited normalcy. This thesis also demonstrated the potential of dMRI for the detection of microstructural alterations after mild and severe trauma, and the combination of conventional and advanced dMRI approaches detected progressive changes in both WM and GM areas. Overall, information provided by the advanced quantitative MRI measures enhanced our understanding of the underlying pathophysiology and could be potentially leveraged in the clinics for more precise assessement of tissue alterations after mild and severe trauma. Finally, work done in this thesis will inform future research and developmental strategies to evaluate the outcomes at both the sub-acute and chronic phases in a mild and severely injured brain, thereby, further enhancing their prognosis and diagnosis.

REFERENCES

Acosta-Cabronero, J., Milovic, C., Mattern, H., Tejos, C., Speck, O., & Callaghan, M. F. (2018). A robust multi-scale approach to quantitative susceptibility mapping. *NeuroImage*, *183*. https://doi.org/10.1016/j.neuroimage.2018.07.065

Aganj, I., Lenglet, C., Sapiro, G., Yacoub, E., Ugurbil, K., & Harel, N. (2010). Reconstruction of the orientation distribution function in single- and multiple-shell q-ball imaging within constant solid angle. *Magnetic Resonance in Medicine*, *64*(2). https://doi.org/10.1002/mrm.22365

Aggarwal, M., Li, X., Gröhn, O., & Sierra, A. (2018). Nuclei-specific deposits of iron and calcium in the rat thalamus after status epilepticus revealed with quantitative susceptibility mapping (QSM). *Journal of Magnetic Resonance Imaging*, *47*(2). https://doi.org/10.1002/jmri.25777

Aggarwal, M., Mori, S., Shimogori, T., Blackshaw, S., & Zhang, J. (2010). Three-dimensional diffusion tensor microimaging for anatomical characterization of the mouse brain. *Magnetic Resonance in Medicine*, *64*(1). https://doi.org/10.1002/mrm.22426

Agoston, D. v., Vink, R., Helmy, A., Risling, M., Nelson, D., & Prins, M. (2019). How to Translate Time: The Temporal Aspects of Rodent and Human Pathobiological Processes in Traumatic Brain Injury. *Journal of Neurotrauma*, *36*(11). https://doi.org/10.1089/neu.2018.6261

Alexander, D. C., Dyrby, T. B., Nilsson, M., & Zhang, H. (2019). Imaging brain microstructure with diffusion MRI: practicality and applications. *NMR in Biomedicine, 32*(4). https://doi.org/10.1002/nbm.3841

Alsop, D. C., Murai, H., Detre, J. A., McIntosh, T. K., & Smith, D. H. (1996). Detection of acute pathologic changes following experimental traumatic brain injury using diffusion-weighted magnetic resonance imaging. *Journal of Neurotrauma*, *13*(9). https://doi.org/10.1089/neu.1996.13.515

Andersson, J. L. R., & Sotiropoulos, S. N. (2016). An integrated approach to correction for off-resonance effects and subject movement in diffusion MR imaging. *NeuroImage*, *125*. https://doi.org/10.1016/j.neuroimage.2015.10.019

Andriessen, T. M. J. C., Jacobs, B., & Vos, P. E. (2010). Clinical characteristics and pathophysiological mechanisms of focal and diffuse traumatic brain injury. *Journal of Cellular and Molecular Medicine*, *14*(10). https://doi.org/10.1111/j.1582-4934.2010.01164.x

Arfanakis, K., Haughton, V. M., Carew, J. D., Rogers, B. P., Dempsey, R. J., & Meyerand, M. E. (2002). Diffusion tensor MR imaging in diffuse axonal injury. *American Journal of Neuroradiology*, *23*(5).

Assaf, Y. (2019). Imaging laminar structures in the gray matter with diffusion MRI. In *NeuroImage*, *197*. https://doi.org/10.1016/j.neuroimage.2017.12.096

Babikian, T., Freier, M. C., Tong, K. A., Nickerson, J. P., Wall, C. J., Holshouser, B. A., Burley, T., Riggs, M. L., & Ashwal, S. (2005). Susceptibility weighted imaging: Neuropsychologic outcome and pediatric head injury. *Pediatric Neurology*, *33*(3). https://doi.org/10.1016/j.pediatrneurol.2005.03.015

Barbosa, J. H. O., Santos, A. C., Tumas, V., Liu, M., Zheng, W., Haacke, E. M., & Salmon, C. E. G. (2015). Quantifying brain iron deposition in patients with Parkinson's disease using quantitative susceptibility mapping, R2 and R2*. *Magnetic Resonance Imaging*, *33*(5). https://doi.org/10.1016/j.mri.2015.02.021

Basser, P. J., Mattiello, J., & LeBihan, D. (1994). MR diffusion tensor spectroscopy and imaging. *Biophysical Journal*, *66*(1). https://doi.org/10.1016/S0006-3495(94)80775-1

Bastiani, M., Cottaar, M., Fitzgibbon, S. P., Suri, S., Alfaro-Almagro, F., Sotiropoulos, S. N., Jbabdi, S., & Andersson, J. L. R. (2019). Automated quality control for within and between studies diffusion MRI data using a non-parametric framework for movement and distortion correction. *NeuroImage*, *184*. https://doi.org/10.1016/j.neuroimage.2018.09.073

Beaulieu, C. (2002). The basis of anisotropic water diffusion in the nervous system - A technical review. *NMR in Biomedicine,* 15(7–8). https://doi.org/10.1002/nbm.782

Beaulieu, C. (2013). The Biological Basis of Diffusion Anisotropy. In *Diffusion MRI: From Quantitative Measurement to In vivo Neuroanatomy: Second Edition*. https://doi.org/10.1016/B978-0-12-396460-1.00008-1

Behrens, T. E. J., Berg, H. J., Jbabdi, S., Rushworth, M. F. S., & Woolrich, M. W. (2007). Probabilistic diffusion tractography with multiple fibre orientations: What can we gain? *NeuroImage*, *34*(1). https://doi.org/10.1016/j.neuroimage.2006.09.018

Behrens, T. E. J., Woolrich, M. W., Jenkinson, M., Johansen-Berg, H., Nunes, R. G., Clare, S., Matthews, P. M., Brady, J. M., & Smith, S. M. (2003). Characterization and Propagation of Uncertainty in Diffusion-Weighted MR Imaging. *Magnetic Resonance in Medicine*, *50*(5). https://doi.org/10.1002/mrm.10609

Benjamini, Y., & Hochberg, Y. (1995). Controlling the False Discovery Rate: A Practical and Powerful Approach to Multiple Testing. *Journal of the Royal Statistical Society: Series B (Methodological)*, *57*(1). https://doi.org/10.1111/j.2517-6161.1995.tb02031.x

Bennett, R. E., mac Donald, C. L., & Brody, D. L. (2012). Diffusion tensor imaging detects axonal injury in a mouse model of repetitive closed-skull traumatic brain injury. *Neuroscience Letters*, *513*(2). https://doi.org/10.1016/j.neulet.2012.02.024

Biegon, A. (2021). Considering Biological Sex in Traumatic Brain Injury. *Frontiers in Neurology*, *12*. https://doi.org/10.3389/fneur.2021.576366

Blamire, A. M. (2018). MR approaches in neurodegenerative disorders. In *Progress in Nuclear Magnetic Resonance Spectroscopy*, *108*. https://doi.org/10.1016/j.pnmrs.2018.11.001

Bosemani, T., Poretti, A., & Huisman, T. A. G. M. (2014). Susceptibility-weighted imaging in pediatric neuroimaging. *Journal of Magnetic Resonance Imaging*, *40*(3). https://doi.org/10.1002/jmri.24410

Bourke, N. J., Yanez Lopez, M., Jenkins, P. O., de Simoni, S., Cole, J. H., Lally, P., Mallas, E.-J., Zhang, H., & Sharp, D. J. (2021). Traumatic brain injury: a comparison of diffusion and volumetric magnetic resonance imaging

measures. *Brain Communications*, *3*(2). https://doi.org/10.1093/braincomms/fcab006

Bradley, W. G. (1993). MR appearance of hemorrhage in the brain. In *Radiology* (Vol. 189, Issue 1). https://doi.org/10.1148/radiology.189.1.8372185

Bramlett, H. M., & Dietrich, W. D. (2002). Quantitative structural changes in white and gray matter 1 year following traumatic brain injury in rats. *Acta Neuropathologica*, *103*(6). https://doi.org/10.1007/s00401-001-0510-8

Bramlett, H. M., & Dietrich, W. D. (2015). Long-Term Consequences of Traumatic Brain Injury: Current Status of Potential Mechanisms of Injury and Neurological Outcomes. *Journal of Neurotrauma*, *32*(23). https://doi.org/10.1089/neu.2014.3352

Broad, R. J., Gabel, M. C., Dowell, N. G., Schwartzman, D. J., Seth, A. K., Zhang, H., Alexander, D. C., Cercignani, M., & Leigh, P. N. (2019). Neurite orientation and dispersion density imaging (NODDI) detects cortical and corticospinal tract degeneration in ALS. *Journal of Neurology, Neurosurgery and Psychiatry*, *90*(4). https://doi.org/10.1136/jnnp-2018-318830

Budde, M. D., Janes, L., Gold, E., Turtzo, L. C., & Frank, J. A. (2011). The contribution of gliosis to diffusion tensor anisotropy and tractography following traumatic brain injury: Validation in the rat using Fourier analysis of stained tissue sections. *Brain*, *134*(8). https://doi.org/10.1093/brain/awr161

Calamante, F., Tournier, J. D., Smith, R. E., & Connelly, A. (2012). A generalised framework for super-resolution track-weighted imaging. *NeuroImage*, *59*(3). https://doi.org/10.1016/j.neuroimage.2011.08.099

Calamuneri, A., Arrigo, A., Mormina, E., Milardi, D., Cacciola, A., Chillemi, G., Marino, S., Gaeta, M., & Quartarone, A. (2018). White matter tissue quantification at Low b-values within constrained spherical deconvolution framework. *Frontiers in Neurology*, *9*. https://doi.org/10.3389/fneur.2018.00716

Carr, H. Y., & Purcell, E. M. (1954). Effects of diffusion on free precession in nuclear magnetic resonance experiments. *Physical Review*, *94*(3). https://doi.org/10.1103/PhysRev.94.630

Cercignani, M., & Horsfield, M. A. (2001). The physical basis of diffusion-weighted MRI. *Journal of the Neurological Sciences*, *186*(Suppl. 1). https://doi.org/10.1016/S0022-510X(01)00486-5

Chappell, K. E., Robson, M. D., Stonebridge-Foster, A., Glover, A., Allsop, J. M., Williams, A. D., Herlihy, A. H., Moss, J., Gishen, P., & Bydder, G. M. (2004). Magic Angle Effects in MR Neurography. *American Journal of Neuroradiology*, *25*(3). https://doi.org/10.1016/s0513-5117(08)70339-9

Chary, K., Narvaez, O., Salo, R. A., San Martín Molina, I., Tohka, J., Aggarwal, M., Gröhn, O., & Sierra, A. (2021). Microstructural Tissue Changes in a Rat Model of Mild Traumatic Brain Injury. *Frontiers in Neuroscience*, *15*. https://doi.org/10.3389/fnins.2021.746214

Chary, K., Nissi, M. J., Nykänen, O., Manninen, E., Rey, R. I., Shmueli, K., Sierra, A., & Gröhn, O. (2021). Quantitative susceptibility mapping of the rat brain after traumatic brain injury. *NMR in Biomedicine*, *34*(2). https://doi.org/10.1002/nbm.4438

Chavhan, G. B., Babyn, P. S., Thomas, B., Shroff, M. M., & Mark Haacke, E. (2009). Principles, techniques, and applications of T2*-based MR imaging and its special applications. *Radiographics*, *29*(5). https://doi.org/10.1148/rg.295095034

Cherubini, A., Péran, P., Hagberg, G. E., Varsi, A. E., Luccichenti, G., Caltagirone, C., Sabatini, U., & Spalletta, G. (2009). Characterization of white matter fiber bundles with T2* relaxometry and diffusion tensor imaging. *Magnetic Resonance in Medicine*, *61*(5). https://doi.org/10.1002/mrm.21978

Cole, W. R., & Bailie, J. M. (2016). Neurocognitive and psychiatric symptoms following mild traumatic brain injury. In *Translational Research in Traumatic Brain Injury*. https://doi.org/10.1201/b18959-24

Colgan, N., Siow, B., O'Callaghan, J. M., Harrison, I. F., Wells, J. A., Holmes, H. E., Ismail, O., Richardson, S., Alexander, D. C., Collins, E. C., Fisher, E. M., Johnson, R., Schwarz, A. J., Ahmed, Z., O'Neill, M. J., Murray, T. K., Zhang, H., & Lythgoe, M. F. (2016). Application of neurite orientation

dispersion and density imaging (NODDI) to a tau pathology model of Alzheimer's disease. *NeuroImage*, *125*. https://doi.org/10.1016/j.neuroimage.2015.10.043

Collorone, S., Prados, F., Kanber, B., Cawley, N. M., Tur, C., Grussu, F., Solanky, B. S., Yiannakas, M., Davagnanam, I., Wheeler-Kingshott, C. A. M. G., Barkhof, F., Ciccarelli, O., & Toosy, A. T. (2021). Brain microstructural and metabolic alterations detected in vivo at onset of the first demyelinating event. *Brain*, *144*(5). https://doi.org/10.1093/brain/awab043

Conti, A. C., Raghupathi, R., Trojanowski, J. Q., & McIntosh, T. K. (1998). Experimental brain injury induces regionally distinct apoptosis during the acute and delayed post-traumatic period. *Journal of Neuroscience*, *18*(15). https://doi.org/10.1523/jneurosci.18-15-05663.1998

Cordero-Grande, L., Christiaens, D., Hutter, J., Price, A. N., & Hajnal, J. v. (2019). Complex diffusion-weighted image estimation via matrix recovery under general noise models. *NeuroImage*, *200*. https://doi.org/10.1016/j.neuroimage.2019.06.039

Crater, S., Maharjan, S., Qi, Y., Zhao, Q., Cofer, G., Cook, J. C., Johnson, G. A., & Wang, N. (2022). Resolution and b value dependent structural connectome in ex vivo mouse brain. *NeuroImage*, *255*. https://doi.org/10.1016/J.NEUROIMAGE.2022.119199

Daducci, A., Canales-Rodríguez, E. J., Zhang, H., Dyrby, T. B., Alexander, D. C., & Thiran, J. P. (2015). Accelerated Microstructure Imaging via Convex Optimization (AMICO) from diffusion MRI data. *NeuroImage*, *105*. https://doi.org/10.1016/j.neuroimage.2014.10.026

Daglas, M., & Adlard, P. A. (2018). The Involvement of Iron in Traumatic Brain Injury and Neurodegenerative Disease. In *Frontiers in Neuroscience*, *12*. https://doi.org/10.3389/fnins.2018.00981

de Luca, A., Guo, F., Froeling, M., & Leemans, A. (2020). Spherical deconvolution with tissue-specific response functions and multi-shell diffusion MRI to estimate multiple fiber orientation distributions (mFODs). *NeuroImage*, *222*. https://doi.org/10.1016/j.neuroimage.2020.117206

Dell'Acqua, F., & Tournier, J. D. (2019). Modelling white matter with spherical deconvolution: How and why? *NMR in Biomedicine*, *32*(4). https://doi.org/10.1002/nbm.3945

Descoteaux, M., Angelino, E., Fitzgibbons, S., & Deriche, R. (2007). Regularized, fast, and robust analytical Q-ball imaging. *Magnetic Resonance in Medicine*, *58*(3). https://doi.org/10.1002/mrm.21277

Dewan, M. C., Rattani, A., Gupta, S., Baticulon, R. E., Hung, Y. C., Punchak, M., Agrawal, A., Adeleye, A. O., Shrime, M. G., Rubiano, A. M., Rosenfeld, J. v., & Park, K. B. (2019). Estimating the global incidence of traumatic brain injury. *Journal of Neurosurgery*, *130*(4). https://doi.org/10.3171/2017.10.JNS17352

Dhollander, T., & Connelly, A. (2016). *A novel iterative approach to reap the benefits of multi-tissue CSD from just single-shell (+b=0) diffusion MRI data*. *A novel iterative approach to reap the benefits of multi-tissue CSD from just single-shell (+b=0) diffusion MRI data*. In *Proc. 24th Annual Meeting of the ISMRM, Singapore.*

Dietrich, W. D., Alonso, O., & Halley, M. (1994). Early Microvascular and Neuronal Consequences of Traumatic Brain Injury: A Light and Electron Microscopic Study in Rats. *Journal of Neurotrauma*, *11*(3). https://doi.org/10.1089/neu.1994.11.289

Dixon, C. E., Kochanek, P. M., Yan, H. Q., Schiding, J. K., Griffith, R. G., Baum, E., Marion, D. W., & DeKosky, S. T. (1999). One-year study of spatial memory performance, brain morphology, and cholinergic markers after moderate controlled cortical impact in rats. *Journal of Neurotrauma*, *16*(2). https://doi.org/10.1089/neu.1999.16.109

Duyn, J. H., & Schenck, J. (2017). Contributions to magnetic susceptibility of brain tissue. *NMR in Biomedicine, 30*(4). https://doi.org/10.1002/nbm.3546

Edlow, B. L., Copen, W. A., Izzy, S., Bakhadirov, K., van der Kouwe, A., Glenn, M. B., Greenberg, S. M., Greer, D. M., & Wu, O. (2016). Diffusion tensor imaging in acute-to-subacute traumatic brain injury: A longitudinal analysis. *BMC Neurology*, *16*(1). https://doi.org/10.1186/s12883-015-0525-8

Enzinger, C., Barkhof, F., Ciccarelli, O., Filippi, M., Kappos, L., Rocca, M. A., Ropele, S., Rovira, À., Schneider, T., de Stefano, N., Vrenken, H., Wheeler-Kingshott, C., Wuerfel, J., & Fazekas, F. (2015). Nonconventional MRI and microstructural cerebral changes in multiple sclerosis. In *Nature Reviews Neurology, 11*(12). https://doi.org/10.1038/nrneurol.2015.194

Fazekas, F., Kleinert, R., Offenbacher, H., Payer, F., Schmidt, R., Kleinert, G., Radner, H., & Lechner, H. (1991). The morphologic correlate of incidental punctate white matter hyperintensities on MR images. *American Journal of Roentgenology*, *157*(6).

Fazekas, F., Kleinert, R., Offenbacher, H., Schmidt, R., Kleinert, G., Payer, F., Radner, H., & Lechner, H. (1993). Pathologic correlates of incidental mri white matter signal hyperintensities. *Neurology*, *43*(9). https://doi.org/10.1212/wnl.43.9.1683

Filzmoser, P. (2016). Identification of Multivariate Outliers: A Performance Study. *Austrian Journal of Statistics*, *34*(2). https://doi.org/10.17713/ajs.v34i2.406

Fukunaga, M., Li, T. Q., van Gelderen, P., de Zwart, J. A., Shmueli, K., Yao, B., Lee, J., Maric, D., Aronova, M. A., Zhang, G., Leapman, R. D., Schenck, J. F., Merkle, H., & Duyn, J. H. (2010). Layer-specific variation of iron content in cerebral cortex as a source of MRI contrast. *Proceedings of the National Academy of Sciences of the United States of America*, *107*(8). https://doi.org/10.1073/pnas.0911177107

G. van Rossum. (1995). Python tutorial, Technical Report CS-R9526, Centrum voor Wiskunde en Informatica (CWI). *Amsterdam*.

Gajamange, S., Raffelt, D., Dhollander, T., Lui, E., van der Walt, A., Kilpatrick, T., Fielding, J., Connelly, A., & Kolbe, S. (2018). Fibre-specific white matter changes in multiple sclerosis patients with optic neuritis. *NeuroImage: Clinical*, *17*. https://doi.org/10.1016/j.nicl.2017.09.027

Galloway, N. R., Tong, K. A., Ashwal, S., Oyoyo, U., & Obenaus, A. (2008). Diffusion-weighted imaging improves outcome prediction in pediatric traumatic brain injury. *Journal of Neurotrauma*, *25*(10). https://doi.org/10.1089/neu.2007.0494

Gayoso, M. J., Al-Majdalawi, A., Garrosa, M., Calvo, B., & Díz-Flores, L. (2003). Selective calcification of rat brain lesions caused by systemic administration of kainic acid. *Histology and Histopathology*, *18*(3).

Gazdzinski, L. M., Mellerup, M., Wang, T., Adel, S. A. A., Lerch, J. P., Sled, J. G., Nieman, B. J., & Wheeler, A. L. (2020). White Matter Changes Caused by Mild Traumatic Brain Injury in Mice Evaluated Using Neurite Orientation Dispersion and Density Imaging. *Journal of Neurotrauma*, *37*(16). https://doi.org/10.1089/neu.2020.6992

Grazioplene, R. G., Bearden, C. E., Subotnik, K. L., Ventura, J., Haut, K., Nuechterlein, K. H., & Cannon, T. D. (2018). Connectivity-enhanced diffusion analysis reveals white matter density disruptions in first episode and chronic schizophrenia. *NeuroImage: Clinical*, *18*. https://doi.org/10.1016/j.nicl.2018.02.015

Gupte, R., Brooks, W., Vukas, R., Pierce, J., & Harris, J. (2019). Sex Differences in Traumatic Brain Injury: What We Know and What We Should Know. *Journal of Neurotrauma, 36*(22). https://doi.org/10.1089/neu.2018.6171

Haacke, E. M., Cheng, N. Y. C., House, M. J., Liu, Q., Neelavalli, J., Ogg, R. J., Khan, A., Ayaz, M., Kirsch, W., & Obenaus, A. (2005). Imaging iron stores in the brain using magnetic resonance imaging. *Magnetic Resonance Imaging*, *23*(1). https://doi.org/10.1016/j.mri.2004.10.001

Haacke, E. M., Mittal, S., Wu, Z., Neelavalli, J., & Cheng, Y. C. N. (2009). Susceptibility-weighted imaging: Technical aspects and clinical applications, part 1. In *American Journal of Neuroradiology,* 30(1). https://doi.org/10.3174/ajnr.A1400

Haase, A., Frahm, J., Matthaei, D., Hanicke, W., & Merboldt, K. D. (1986). FLASH imaging. Rapid NMR imaging using low flip-angle pulses. *Journal of Magnetic Resonance*, *67*(2). https://doi.org/10.1016/0022-2364(86)90433-6

Hahn, E. L. (1950). Spin echoes. *Physical Review*, *80*(4). https://doi.org/10.1103/PhysRev.80.580

Hanstock, C. C., Faden, A. I., Bendall, M. R., & Vink, R. (1994). Diffusion-weighted imaging differentiates ischemic tissue from traumatized tissue. *Stroke*, *25*(4). https://doi.org/10.1161/01.STR.25.4.843

Harsan, L. A., Dávid, C., Reisert, M., Schnell, S., Hennig, J., von Elverfeldt, D., & Staiger, J. F. (2013). Mapping remodeling of thalamocortical projections in the living reeler mouse brain by diffusion tractography. *Proceedings of the National Academy of Sciences of the United States of America*, *110*(19). https://doi.org/10.1073/pnas.1218330110

Heffernan, M. E., Huang, W., Sicard, K. M., Bratane, B. T., Sikoglu, E. M., Zhang, N., Fisher, M., & King, J. A. (2013). Multi-modal approach for investigating brain and behavior changes in an animal model of traumatic brain injury. *Journal of Neurotrauma*, *30*(11). https://doi.org/10.1089/neu.2012.2366

Henze, N., & Zirkler, B. (1990). A class of invariant consistent tests for multivariate normality. *Communications in Statistics - Theory and Methods*, *19*(10). https://doi.org/10.1080/03610929008830400

Herrera, J. J., Bockhorst, K., Kondraganti, S., Stertz, L., Quevedo, J., & Narayana, P. A. (2017). Acute White Matter Tract Damage after Frontal Mild Traumatic Brain Injury. *Journal of Neurotrauma*, *34*(2). https://doi.org/10.1089/neu.2016.4407

Hicks, R., Soares, H., Smith, D., & McIntosh, T. (1996). Temporal and spatial characterization of neuronal injury following lateral fluid-percussion brain injury in the rat. *Acta Neuropathologica*, *91*(3). https://doi.org/10.1007/s004010050421

Hou, D. J., Tong, K. A., Ashwal, S., Oyoyo, U., Joo, E., Shutter, L., & Obenaus, A. (2007). Diffusion-weighted magnetic resonance imaging improves outcome prediction in adult traumatic brain injury. *Journal of Neurotrauma*, *24*(10). https://doi.org/10.1089/neu.2007.0339

Hutchinson, E. B., Rutecki, P. A., Alexander, A. L., & Sutula, T. P. (2012). Fisher statistics for analysis of diffusion tensor directional information. *Journal of Neuroscience Methods*, *206*(1). https://doi.org/10.1016/j.jneumeth.2012.02.004

Hutchinson, E. B., Schwerin, S. C., Avram, A. v., Juliano, S. L., & Pierpaoli, C. (2018). Diffusion MRI and the detection of alterations following traumatic brain injury. In *Journal of Neuroscience Research, 96*(4). https://doi.org/10.1002/jnr.24065

Hutchinson, E. B., Schwerin, S. C., Radomski, K. L., Sadeghi, N., Komlosh, M. E., Irfanoglu, M. O., Juliano, S. L., & Pierpaoli, C. (2018). Detection and distinction of mild brain injury effects in a ferret model using diffusion tensor MRI (DTI) and DTI-driven tensor-based morphometry (D-TBM). *Frontiers in Neuroscience*, *12*. https://doi.org/10.3389/fnins.2018.00573

Huttunen, J. K., Airaksinen, A. M., Barba, C., Colicchio, G., Niskanen, J. P., Shatillo, A., Sierra Lopez, A., Ndode-Ekane, X. E., Pitkänen, A., & Gröhn, O. H. (2018). Detection of Hyperexcitability by Functional Magnetic Resonance Imaging after Experimental Traumatic Brain Injury. *Journal of Neurotrauma*, *35*(22). https://doi.org/10.1089/neu.2017.5308

Hylin, M. J., Orsi, S. A., Zhao, J., Bockhorst, K., Perez, A., Moore, A. N., & Dash, P. K. (2013). Behavioral and histopathological alterations resulting from mild fluid percussion injury. *Journal of Neurotrauma*, *30*(9). https://doi.org/10.1089/neu.2012.2630

Jensen, J. H., & Helpern, J. A. (2010). MRI quantification of non-Gaussian water diffusion by kurtosis analysis. *NMR in Biomedicine, 23*(7). https://doi.org/10.1002/nbm.1518

Jespersen, S. N., Leigland, L. A., Cornea, A., & Kroenke, C. D. (2012). Determination of axonal and dendritic orientation distributions within the developing cerebral cortex by diffusion tensor imaging. *IEEE Transactions on Medical Imaging*, *31*(1). https://doi.org/10.1109/TMI.2011.2162099

Jeurissen, B., Descoteaux, M., Mori, S., & Leemans, A. (2019). Diffusion MRI fiber tractography of the brain. *NMR in Biomedicine, 32*(4). https://doi.org/10.1002/nbm.3785

Jeurissen, B., Leemans, A., Jones, D. K., Tournier, J. D., & Sijbers, J. (2010). Estimating the number of fiber orientations in diffusion MRI voxels: a constrained spherical deconvolution study. *Proceedings of the International Society for Magnetic Resonance in Medicine*, *18*.

Jeurissen, B., Tournier, J. D., Dhollander, T., Connelly, A., & Sijbers, J. (2014). Multi-tissue constrained spherical deconvolution for improved analysis of multi-shell diffusion MRI data. *NeuroImage*, *103*. https://doi.org/10.1016/j.neuroimage.2014.07.061

Johnson, V. E., Meaney, D. F., cullen, D. K., & Smith, D. H. (2015). Animal models of traumatic brain injury. In *Handbook of Clinical Neurology, 127*. https://doi.org/10.1016/B978-0-444-52892-6.00008-8

Johnson, V. E., Stewart, W., & Smith, D. H. (2013). Axonal pathology in traumatic brain injury. In *Experimental Neurology, 246*. https://doi.org/10.1016/j.expneurol.2012.01.013

Jones, D. K., Knösche, T. R., & Turner, R. (2013). White matter integrity, fiber count, and other fallacies: The do's and don'ts of diffusion MRI. In *NeuroImage, 73*. https://doi.org/10.1016/j.neuroimage.2012.06.081

Kamagata, K., Hatano, T., Okuzumi, A., Motoi, Y., Abe, O., Shimoji, K., Kamiya, K., Suzuki, M., Hori, M., Kumamaru, K. K., Hattori, N., & Aoki, S. (2016). Neurite orientation dispersion and density imaging in the substantia nigra in idiopathic Parkinson disease. *European Radiology*, *26*(8). https://doi.org/10.1007/s00330-015-4066-8

Kellner, E., Dhital, B., Kiselev, V. G., & Reisert, M. (2016). Gibbs-ringing artifact removal based on local subvoxel-shifts. *Magnetic Resonance in Medicine*, *76*(5). https://doi.org/10.1002/mrm.26054

Khan, W., Egorova, N., Khlif, M. S., Mito, R., Dhollander, T., & Brodtmann, A. (2020). Three-tissue compositional analysis reveals in-vivo microstructural heterogeneity of white matter hyperintensities following stroke. *NeuroImage*, *218*. https://doi.org/10.1016/j.neuroimage.2020.116869

Kharatishvili, I., Nissinen, J. P., McIntosh, T. K., & Pitkänen, A. (2006). A model of posttraumatic epilepsy induced by lateral fluid-percussion brain injury in rats. *Neuroscience*, *140*(2). https://doi.org/10.1016/j.neuroscience.2006.03.012

Kim, E., Lauterbach, E. C., Reeve, A., Arciniegas, D. B., Coburn, K. L., Mendez, M. F., Rummans, T. A., & Coffey, E. C. (2007). Neuropsychiatric complications of traumatic brain injury: A critical review of the literature (A report by the ANPA Committee on research). *Journal of Neuropsychiatry and Clinical Neurosciences*, *19*(2). https://doi.org/10.1176/jnp.2007.19.2.106

Klohs, J., & Hirt, A. M. (2021). Investigation of the magnetic susceptibility properties of fresh and fixed mouse heart, liver, skeletal muscle and

brain tissue. *Physica Medica*, *88*. https://doi.org/10.1016/j.ejmp.2021.06.014

Kressler, B., de Rochefort, L., Liu, T., Spincemaille, P., Jiang, Q., & Wang, Y. (2010). Nonlinear regularization for per voxel estimation of magnetic susceptibility distributions from MRI field maps. *IEEE Transactions on Medical Imaging*, *29*(2). https://doi.org/10.1109/TMI.2009.2023787

Laitinen, T., Sierra, A., Pitkänen, A., & Gröhn, O. (2010). Diffusion tensor MRI of axonal plasticity in the rat hippocampus. *NeuroImage*, *51*(2). https://doi.org/10.1016/j.neuroimage.2010.02.077

Laitinen, T., Sierra López, A., Bolkvadze, T., Pitkänen, A., & Gröhn, O. (2015). Diffusion tensor imaging detects chronic microstructural changes in white and grey matter after traumatic brain injury in rat. *Frontiers in Neuroscience*, *9*. https://doi.org/10.3389/fnins.2015.00128

Langkammer, C., Liu, T., Khalil, M., Enzinger, C., Jehna, M., Fuchs, S., Fazekas, F., Wang, Y., & Ropele, S. (2013). Quantitative susceptibility mapping in multiple sclerosis. *Radiology*, *267*(2). https://doi.org/10.1148/radiol.12120707

Langkammer, C., Schweser, F., Shmueli, K., Kames, C., Li, X., Guo, L., Milovic, C., Kim, J., Wei, H., Bredies, K., Buch, S., Guo, Y., Liu, Z., Meineke, J., Rauscher, A., Marques, J. P., & Bilgic, B. (2018). Quantitative susceptibility mapping: Report from the 2016 reconstruction challenge. *Magnetic Resonance in Medicine*, *79*(3). https://doi.org/10.1002/mrm.26830

Lauterbur, P. C. (1973). Image formation by induced local interactions: Examples employing nuclear magnetic resonance. *Nature*, *242*(5394). https://doi.org/10.1038/242190a0

le Bihan, D., Breton, E., Lallemand, D., Grenier, P., Cabanis, E., & Laval-Jeantet, M. (1986). MR imaging of intravoxel incoherent motions: Application to diffusion and perfusion in neurologic disorders. *Radiology*, *161*(2). https://doi.org/10.1148/radiology.161.2.3763909

le Bihan, D., Poupon, C., Amadon, A., & Lethimonnier, F. (2006). Artifacts and pitfalls in diffusion MRI. In *Journal of Magnetic Resonance Imaging, 24*(3). https://doi.org/10.1002/jmri.20683

Lehto, L. J., Sierra, A., Corum, C. A., Zhang, J., Idiyatullin, D., Pitkänen, A., Garwood, M., & Gröhn, O. (2012). Detection of calcifications in vivo and ex vivo after brain injury in rat using SWIFT. *NeuroImage*, *61*(4). https://doi.org/10.1016/j.neuroimage.2012.03.002
Lehto, L. J., Sierra, A., Corum, C. A., Zhang, J., Idiyatullin, D., Pitkänen, A., Garwood, M., & Gröhn, O. (2012). Detection of calcifications in vivo and ex vivo after brain injury in rat using SWIFT. *NeuroImage*, *61*(4). https://doi.org/10.1016/j.neuroimage.2012.03.002
Leutritz, T., Hilfert, L., Smalla, K. H., Speck, O., & Zhong, K. (2013). Accurate quantification of water-macromolecule exchange induced frequency shift: Effects of reference substance. *Magnetic Resonance in Medicine*, *69*(1). https://doi.org/10.1002/mrm.24223

Levitt, M. H. (2002). Spin dynamics: basics of nuclear magnetic resonance. In *Magnetic Resonance in Chemistry, 40*.

Li, W., Long, J. A., Watts, L., Shen, Q., Liu, Y., Jiang, Z., & Duong, T. Q. (2016). Spatiotemporal changes in diffusion, T2 and susceptibility of white matter following mild traumatic brain injury. *NMR in Biomedicine*, *29*(7). https://doi.org/10.1002/nbm.3536

Li, W., Wu, B., Avram, A. v., & Liu, C. (2012). Magnetic susceptibility anisotropy of human brain in vivo and its molecular underpinnings. *NeuroImage*, *59*(3). https://doi.org/10.1016/j.neuroimage.2011.10.038

Ling, H., Hardy, J., & Zetterberg, H. (2015). Neurological consequences of traumatic brain injuries in sports. In *Molecular and Cellular Neuroscience, 66*(Pt. B). https://doi.org/10.1016/j.mcn.2015.03.012

Liu, C., Li, W., Johnson, G. A., & Wu, B. (2011). High-field (9.4T) MRI of brain dysmyelination by quantitative mapping of magnetic susceptibility. *NeuroImage*, *56*(3). https://doi.org/10.1016/j.neuroimage.2011.02.024

Liu, C., Li, W., Tong, K. A., Yeom, K. W., & Kuzminski, S. (2015). Susceptibility-weighted imaging and quantitative susceptibility mapping in the brain. In *Journal of Magnetic Resonance Imaging, 42*(1). https://doi.org/10.1002/jmri.24768

Liu, J., Liu, T., de Rochefort, L., Ledoux, J., Khalidov, I., Chen, W., Tsiouris, A. J., Wisnieff, C., Spincemaille, P., Prince, M. R., & Wang, Y. (2012). Morphology enabled dipole inversion for quantitative susceptibility

mapping using structural consistency between the magnitude image and the susceptibility map. *NeuroImage*, *59*(3). https://doi.org/10.1016/j.neuroimage.2011.08.082

Liu, T., Khalidov, I., de Rochefort, L., Spincemaille, P., Liu, J., Tsiouris, A. J., & Wang, Y. (2011). A novel background field removal method for MRI using projection onto dipole fields (PDF). *NMR in Biomedicine*, *24*(9). https://doi.org/10.1002/nbm.1670

Liu, T., Spincemaille, P., de Rochefort, L., Kressler, B., & Wang, Y. (2009). Calculation of susceptibility through multiple orientation sampling (COSMOS): A method for conditioning the inverse problem from measured magnetic field map to susceptibility source image in MRI. *Magnetic Resonance in Medicine*, *61*(1). https://doi.org/10.1002/mrm.21828

Liu, W., Soderlund, K., Senseney, J. S., Joy, D., Yeh, P. H., Ollinger, J., Sham, E. B., Liu, T., Wang, Y., Oakes, T. R., & Riedy, G. (2016). Imaging cerebral microhemorrhages in military service members with chronic traumatic brain injury. *Radiology*, *278*(2). https://doi.org/10.1148/radiol.2015150160

Liu, Y. R., Cardamone, L., Hogan, R. E., Gregoire, M. C., Williams, J. P., Hicks, R. J., Binns, D., Koe, A., Jones, N. C., Myers, D. E., O'Brien, T. J., & Bouilleret, V. (2010). Progressive metabolic and structural cerebral perturbations after traumatic brain injury: An in vivo imaging study in the rat. *Journal of Nuclear Medicine*, *51*(11). https://doi.org/10.2967/jnumed.110.078626

Ma, X., Aravind, A., Pfister, B. J., Chandra, N., & Haorah, J. (2019). Animal Models of Traumatic Brain Injury and Assessment of Injury Severity. In *Molecular Neurobiology*, *56*(8). https://doi.org/10.1007/s12035-018-1454-5

Maas, A. I., Stocchetti, N., & Bullock, R. (2008). Moderate and severe traumatic brain injury in adults. In *The Lancet Neurology, 7*(8). https://doi.org/10.1016/S1474-4422(08)70164-9

mac Donald, C. L., Dikranian, K., Bayly, P., Holtzman, D., & Brody, D. (2007). Diffusion tensor imaging reliably detects experimental traumatic

axonal injury and indicates approximate time of injury. *Journal of Neuroscience*, *27*(44). https://doi.org/10.1523/JNEUROSCI.3647-07.2007

mac Donald, C. L., Dikranian, K., Song, S. K., Bayly, P. v., Holtzman, D. M., & Brody, D. L. (2007). Detection of traumatic axonal injury with diffusion tensor imaging in a mouse model of traumatic brain injury. *Experimental Neurology*, *205*(1). https://doi.org/10.1016/j.expneurol.2007.01.035

Mäkinen, S., van Groen, T., Clarke, J., Thornell, A., Corbett, D., Hiltunen, M., Soininen, H., & Jolkkonen, J. (2008). Coaccumulation of calcium and β-amyloid in the thalamus after transient middle cerebral artery occlusion in rats. *Journal of Cerebral Blood Flow and Metabolism*, *28*(2). https://doi.org/10.1038/sj.jcbfm.9600529

Mansfield, P., & Grannell, P. K. (1973). Nmr 'diffraction' in solids? In *Journal of Physics C: Solid State Physics, 6*(22). https://doi.org/10.1088/0022-3719/6/22/007

Marshall, L. F., Marshall, S. B., Klauber, M. R., van Berkum Clark, M., Eisenberg, H. M., Jane, J. A., Luerssen, T. G., Marmarou, A., & Foulkes, M. A. (1991). A new classification of head injury based on computerized tomography. *Journal of Neurosurgery*, *75*(Suppl. 1). https://doi.org/10.3171/sup.1991.75.1s.0s14

McCunn, P., Xu, X., Moszczynski, A., Li, A., Brown, A., & Bartha, R. (2021). Neurite orientation dispersion and density imaging in a rodent model of acute mild traumatic brain injury. *Journal of Neuroimaging*, *31*(5). https://doi.org/10.1111/jon.12917

McIntosh, T. K., Vink, R., Noble, L., Yamakami, I., Fernyak, S., Soares, H., & Faden, A. L. (1989). Traumatic brain injury in the rat: Characterization of a lateral fluid-percussion model. *Neuroscience*, *28*(1). https://doi.org/10.1016/0306-4522(89)90247-9

Mechtler, L. L., Shastri, K. K., & Crutchfield, K. E. (2014). Advanced neuroimaging of mild traumatic brain injury. In *Neurologic Clinics, 32*(1). https://doi.org/10.1016/j.ncl.2013.08.002

Mito, R., Dhollander, T., Xia, Y., Raffelt, D., Salvado, O., Churilov, L., Rowe, C. C., Brodtmann, A., Villemagne, V. L., & Connelly, A. (2020). In vivo microstructural heterogeneity of white matter lesions in healthy

elderly and Alzheimer's disease participants using tissue compositional analysis of diffusion MRI data. *NeuroImage: Clinical*, *28*. https://doi.org/10.1016/j.nicl.2020.102479

Mito, R., Raffelt, D., Dhollander, T., Vaughan, D. N., Tournier, J. D., Salvado, O., Brodtmann, A., Rowe, C. C., Villemagne, V. L., & Connelly, A. (2018). Fibre-specific white matter reductions in Alzheimer's disease and mild cognitive impairment. *Brain*, *141*(3). https://doi.org/10.1093/brain/awx355

Mittal, S., Wu, Z., Neelavalli, J., & Haacke, E. M. (2009). Susceptibility-weighted imaging: Technical aspects and clinical applications, part 2. In *American Journal of Neuroradiology, 30*(2). https://doi.org/10.3174/ajnr.A1461

Mohamed, A. Z., Cumming, P., & Nasrallah, F. A. (2021). Traumatic brain injury augurs ill for prolonged deficits in the brain's structural and functional integrity following controlled cortical impact injury. *Scientific Reports*, *11*(1). https://doi.org/10.1038/s41598-021-00660-5

Molina, I. S. M., Salo, R. A., Abdollahzadeh, A., Tohka, J., Gröhn, O., & Sierra, A. (2020). In vivo diffusion tensor imaging in acute and subacute phases of mild traumatic brain injury in rats. *ENeuro*, *7*(3). https://doi.org/10.1523/ENEURO.0476-19.2020

Mori, S., & Tournier, J. D. (2013). Introduction to diffusion tensor imaging: And higher order models: Second edition. In *Introduction to Diffusion Tensor Imaging: And Higher Order Models: Second Edition*. https://doi.org/10.1016/C2011-0-07607-X

Mori, S., & van Zijl, P. C. M. (2002). Fiber tracking: Principles and strategies - A technical review. In *NMR in Biomedicine, 15*(7–8). https://doi.org/10.1002/nbm.781

Mori, S., & Zhang, J. (2006). Principles of Diffusion Tensor Imaging and Its Applications to Basic Neuroscience Research. In *Neuron, 51*(5). https://doi.org/10.1016/j.neuron.2006.08.012

Muller, J., Middleton, D., Alizadeh, M., Zabrecky, G., Wintering, N., Bazzan, A. J., Lang, J., Wu, C., Monti, D. A., Wu, Q., Newberg, A. B., & Mohamed, F. B. (2021). Hybrid diffusion imaging reveals altered white matter tract integrity and associations with symptoms and cognitive dysfunction in

chronic traumatic brain injury. *NeuroImage: Clinical*, *30*. https://doi.org/10.1016/j.nicl.2021.102681

Murakami, Y., Kakeda, S., Watanabe, K., Ueda, I., Ogasawara, A., Moriya, J., Ide, S., Futatsuya, K., Sato, T., Okada, K., Uozumi, T., Tsuji, S., Liu, T., Wang, Y., & Korogi, Y. (2015). Usefulness of quantitative susceptibility mapping for the diagnosis of Parkinson disease. *American Journal of Neuroradiology*, *36*(6). https://doi.org/10.3174/ajnr.A4260

Nazeri, A., Chakravart, M., Rotenberg, D. J., Rajji, T. K., Rathi, X., Michailovich, O. v., & Voineskos, A. N. (2015). Functional consequences of neurite orientation dispersion and density in humans across the adult lifespan. *Journal of Neuroscience*, *35*(4). https://doi.org/10.1523/JNEUROSCI.3979-14.2015

Nisenbaum, E. J., Novikov, D. S., & Lui, Y. W. (2014). The presence and role of iron in mild traumatic brain injury: An imaging perspective. *Journal of Neurotrauma*, *31*(4). https://doi.org/10.1089/neu.2013.3102

Noll, D. C., Nishimura, D. G., & Macovski, A. (1991). Homodyne Detection in Magnetic Resonance Imaging. *IEEE Transactions on Medical Imaging*, *10*(2). https://doi.org/10.1109/42.79473

Oehr, L. E., Yang, J. Y. M., Chen, J., Maller, J. J., Seal, M. L., & Anderson, J. F. I. (2021). Investigating White Matter Tract Microstructural Changes at Six-Twelve Weeks following Mild Traumatic Brain Injury: A Combined Diffusion Tensor Imaging and Neurite Orientation Dispersion and Density Imaging Study. *Journal of Neurotrauma*, *38*(16). https://doi.org/10.1089/neu.2020.7310

Okubo, S., Xi, G., Keep, R. F., Muraszko, K. M., & Hua, Y. (2013). Cerebral hemorrhage, brain edema, and heme oxygenase-1 expression after experimental traumatic brain injury. *Acta Neurochirurgica. Supplement*, *118*. https://doi.org/10.1007/978-3-7091-1434-6_14

Özarslan, E., Koay, C. G., Shepherd, T. M., Komlosh, M. E., Irfanoğlu, M. O., Pierpaoli, C., & Basser, P. J. (2013). Mean apparent propagator (MAP) MRI: A novel diffusion imaging method for mapping tissue microstructure. *NeuroImage*, *78*. https://doi.org/10.1016/j.neuroimage.2013.04.016

Palombo, M., Ianus, A., Guerreri, M., Nunes, D., Alexander, D. C., Shemesh, N., & Zhang, H. (2020). SANDI: A compartment-based model for non-invasive apparent soma and neurite imaging by diffusion MRI. *NeuroImage*, *215*. https://doi.org/10.1016/j.neuroimage.2020.116835

Pannek, K., Raffelt, D., Salvado, O., & Rose, S. (2012). Incorporating Directional Information in Diffusion Tractography Derived Maps: Angular Track Imaging (ATI). In *Proc. 20th Annual Meeting of the Intl. Soc. Magn. Reson. Med. (ISMRM), Melbourne, Australia*.

Pervez, M., Kitagawa, R. S., & Chang, T. R. (2018). Definition of Traumatic Brain Injury, Neurosurgery, Trauma Orthopedics, Neuroimaging, Psychology, and Psychiatry in Mild Traumatic Brain Injury. In *Neuroimaging Clinics of North America, 28*(1). https://doi.org/10.1016/j.nic.2017.09.010

Pierce, J. E. S., Smith, D. H., Trojanowski, J. Q., & McIntosh, T. K. (1998). Enduring cognitive, neurobehavioral and histopathological changes persist for up to one year following severe experimental brain injury in rats. *Neuroscience*, *87*(2). https://doi.org/10.1016/S0306-4522(98)00142-0

Pierpaoli, C., Barnett, A., Pajevic, S., Chen, R., Penix, L. R., Virta, A., & Basser, P. (2001). Water diffusion changes in wallerian degeneration and their dependence on white matter architecture. *NeuroImage*, *13*(6). https://doi.org/10.1006/nimg.2001.0765

Pierpaoli, C., & Basser, P. J. (1996). Toward a quantitative assessment of diffusion anisotropy. *Magnetic Resonance in Medicine*, *36*(6). https://doi.org/10.1002/mrm.1910360612

Rabi, I. I., Zacharias, J. R., Millman, S., & Kusch, P. (1938). A new method of measuring nuclear magnetic moment [5]. In *Physical Review, 53*(4). https://doi.org/10.1103/PhysRev.53.318

Raffelt, D., Tournier, J. D., Fripp, J., Crozier, S., Connelly, A., & Salvado, O. (2011). Symmetric diffeomorphic registration of fibre orientation distributions. *NeuroImage*, *56*(3). https://doi.org/10.1016/j.neuroimage.2011.02.014

Raffelt, D., Tournier, J. D., Crozier, S., Connelly, A., & Salvado, O. (2012). Reorientation of fiber orientation distributions using apodized point

spread functions. *Magnetic Resonance in Medicine*, *67*(3). https://doi.org/10.1002/mrm.23058

Raffelt, D. A., Smith, R. E., Ridgway, G. R., Tournier, J. D., Vaughan, D. N., Rose, S., Henderson, R., & Connelly, A. (2015). Connectivity-based fixel enhancement: Whole-brain statistical analysis of diffusion MRI measures in the presence of crossing fibres. *NeuroImage*, *117*. https://doi.org/10.1016/j.neuroimage.2015.05.039

Raffelt, D. A., Tournier, J. D., Smith, R. E., Vaughan, D. N., Jackson, G., Ridgway, G. R., & Connelly, A. (2017). Investigating white matter fibre density and morphology using fixel-based analysis. *NeuroImage*, *144*. https://doi.org/10.1016/j.neuroimage.2016.09.029

Raffelt, D., Tournier, J. D., Rose, S., Ridgway, G. R., Henderson, R., Crozier, S., Salvado, O., & Connelly, A. (2012). Apparent Fibre Density: A novel measure for the analysis of diffusion-weighted magnetic resonance images. *NeuroImage*, *59*(4). https://doi.org/10.1016/j.neuroimage.2011.10.045

Ramonet, D., de Yebra, L., Fredriksson, K., Bernal, F., Ribalta, T., & Mahy, N. (2006). Similar calcification process in acute and chronic human brain pathologies. *Journal of Neuroscience Research*, *83*(1). https://doi.org/10.1002/jnr.20711

Rane, S., & Duong, T. Q. (2011). Comparison of In Vivo and Ex Vivo Diffusion Tensor Imaging in Rhesus Macaques at Short and Long Diffusion Times. *The Open Neuroimag Journal*, *5*(Suppl. 2). https://doi.org/10.2174/1874440001105010172

Reeves, T. M., Phillips, L. L., & Povlishock, J. T. (2005). Myelinated and unmyelinated axons of the corpus callosum differ in vulnerability and functional recovery following traumatic brain injury. *Experimental Neurology*, *196*(1). https://doi.org/10.1016/j.expneurol.2005.07.014

Reeves, T. M., Smith, T. L., Williamson, J. C., & Phillips, L. L. (2012). Unmyelinated axons show selective rostrocaudal pathology in the corpus callosum after traumatic brain injury. *Journal of Neuropathology and Experimental Neurology*, *71*(3). https://doi.org/10.1097/NEN.0b013e3182482590

Rudko, D. A., Klassen, L. M., de Chickera, S. N., Gati, J. S., Dekaban, G. A., & Menon, R. S. (2014). Origins of R2* orientation dependence in gray and white matter. *Proceedings of the National Academy of Sciences of the United States of America*, *111*(1). https://doi.org/10.1073/pnas.1306516111

Saini, J., Kesavadas, C., Thomas, B., Kapilamoorthy, T. R., Gupta, A. K., Radhakrishnan, A., & Radhakrishnan, K. (2009). Susceptibility weighted imaging in the diagnostic evaluation of patients with intractable epilepsy. *Epilepsia*, *50*(6). https://doi.org/10.1111/j.1528-1167.2008.01882.x

Salo, R. A., Belevich, I., Jokitalo, E., Gröhn, O., & Sierra, A. (2021). Assessment of the structural complexity of diffusion MRI voxels using 3D electron microscopy in the rat brain. *NeuroImage*, *225*. https://doi.org/10.1016/j.neuroimage.2020.117529

Schenck, J. F. (1996). The role of magnetic susceptibility in magnetic resonance imaging: MRI magnetic compatibility of the first and second kinds. *Medical Physics*, *23*(6). https://doi.org/10.1118/1.597854

Schilling, K. G., Gao, Y., Stepniewska, I., Janve, V., Landman, B. A., & Anderson, A. W. (2019). Histologically derived fiber response functions for diffusion MRI vary across white matter fibers—An ex vivo validation study in the squirrel monkey brain. *NMR in Biomedicine*, *32*(6). https://doi.org/10.1002/nbm.4090

Schmidt, R., Grazer, A., Enzinger, C., Ropele, S., Homayoon, N., Pluta-Fuerst, A., Schwingenschuh, P., Katschnig, P., Cavalieri, M., Schmidt, H., Langkammer, C., Ebner, F., & Fazekas, F. (2011). MRI-detected white matter lesions: Do they really matter? In *Journal of Neural Transmission,* 118(5). https://doi.org/10.1007/s00702-011-0594-9

Schofield, M. A., & Zhu, Y. (2003). Fast phase unwrapping algorithm for interferometric applications. *Optics Letters*, *28*(14). https://doi.org/10.1364/ol.28.001194

Schwarzbold, M., Diaz, A., Martins, E. T., Rufino, A., Amante, L. N., Thais, M. E., Quevedo, J., Hohl, A., Linhares, M. N., & Walz, R. (2008). Psychiatric disorders and traumatic brain injury. In *Neuropsychiatric Disease and Treatment, 4*(4). https://doi.org/10.2147/ndt.s2653

Schweser, F., Deistung, A., Lehr, B. W., & Reichenbach, J. R. (2010). Differentiation between diamagnetic and paramagnetic cerebral lesions based on magnetic susceptibility mapping. *Medical Physics*, *37*(10). https://doi.org/10.1118/1.3481505

Schweser, F., Deistung, A., Lehr, B. W., & Reichenbach, J. R. (2011). Quantitative imaging of intrinsic magnetic tissue properties using MRI signal phase: An approach to in vivo brain iron metabolism? *NeuroImage*, *54*(4). https://doi.org/10.1016/j.neuroimage.2010.10.070

Schweser, F., Deistung, A., & Reichenbach, J. R. (2016). Foundations of MRI phase imaging and processing for Quantitative Susceptibility Mapping (QSM). *Zeitschrift Fur Medizinische Physik*, *26*(1). https://doi.org/10.1016/j.zemedi.2015.10.002

Schweser, F., Deistung, A., Sommer, K., & Reichenbach, J. R. (2013). Toward online reconstruction of quantitative susceptibility maps: Superfast dipole inversion. *Magnetic Resonance in Medicine*, *69*(6). https://doi.org/10.1002/mrm.24405

Schweser, F., Kyyriäinen, J., Preda, M., Pitkänen, A., Toffolo, K., Poulsen, A., Donahue, K., Levy, B., & Poulsen, D. (2019). Visualization of thalamic calcium influx with quantitative susceptibility mapping as a potential imaging biomarker for repeated mild traumatic brain injury. *NeuroImage*, *200*. https://doi.org/10.1016/j.neuroimage.2019.06.024

Seabold, S., & Perktold, J. (2010). Statsmodels: Econometric and Statistical Modeling with Python. *Proceedings of the 9th Python in Science Conference*. https://doi.org/10.25080/majora-92bf1922-011

Shapiro, S. S., & Wilk, M. B. (1965). An analysis of variance test for normality (complete samples). *Biometrika*, *52*(3–4). https://doi.org/10.1093/biomet/52.3-4.591

Shmueli, K., de Zwart, J. A., van Gelderen, P., Li, T. Q., Dodd, S. J., & Duyn, J. H. (2009). Magnetic susceptibility mapping of brain tissue in vivo using MRI phase data. *Magnetic Resonance in Medicine*, *62*(6). https://doi.org/10.1002/mrm.22135

Shmueli, K., Dodd, S. J., Li, T. Q., & Duyn, J. H. (2011). The contribution of chemical exchange to MRI frequency shifts in brain tissue. *Magnetic*

Resonance in Medicine : Official Journal of the Society of Magnetic Resonance in Medicine / Society of Magnetic Resonance in Medicine, *65*(1). https://doi.org/10.1002/mrm.22604

Shoamanesh, A., Kwok, C. S., & Benavente, O. (2011). Cerebral microbleeds: Histopathological correlation of neuroimaging. In *Cerebrovascular Diseases, 32*(6). https://doi.org/10.1159/000331466

Sidaros, A., Engberg, A. W., Sidaros, K., Liptrot, M. G., Herning, M., Petersen, P., Paulson, O. B., Jernigan, T. L., & Rostrup, E. (2008). Diffusion tensor imaging during recovery from severe traumatic brain injury and relation to clinical outcome: A longitudinal study. *Brain*, *131*(2). https://doi.org/10.1093/brain/awm294

Sierra, A., Laitinen, T., Gröhn, O., & Pitkänen, A. (2015). Diffusion tensor imaging of hippocampal network plasticity. *Brain Structure and Function*, *220*(2). https://doi.org/10.1007/s00429-013-0683-7

Smith, D. H., Hicks, R., & Povlishock, J. T. (2013). Therapy development for diffuse axonal injury. In *Journal of Neurotrauma, 30*(5). https://doi.org/10.1089/neu.2012.2825

Smith, D. H., Meaney, D. F., Lenkinski, R. E., Alsop, D. C., Grossman, R., Kimura, H., Mcintosh, T. K., & Gennarelli, T. A. (1995). New Magnetic Resonance Imaging Techniques for the Evaluation of Traumatic Brain Injury. *Journal of Neurotrauma*, *12*(4). https://doi.org/10.1089/neu.1995.12.573

Smith, R. E., Tournier, J. D., Calamante, F., & Connelly, A. (2013). SIFT: Spherical-deconvolution informed filtering of tractograms. *NeuroImage*, *67*. https://doi.org/10.1016/j.neuroimage.2012.11.049

Smith, S. M., & Nichols, T. E. (2009). Threshold-free cluster enhancement: Addressing problems of smoothing, threshold dependence and 123ocalization in cluster inference. *NeuroImage*, *44*(1). https://doi.org/10.1016/j.neuroimage.2008.03.061

Stanisz, G. J., Szafer, A., Wright, G. A., & Henkelman, R. M. (1997). An analytical model of restricted diffusion in bovine optic nerve. *Magnetic Resonance in Medicine*, *37*(1). https://doi.org/10.1002/mrm.1910370115

Stejskal, E. O., & Tanner, J. E. (1965). Spin diffusion measurements: Spin echoes in the presence of a time-dependent field gradient. *The Journal of Chemical Physics*, *42*(1). https://doi.org/10.1063/1.1695690

Stemper, B. D., Shah, A. S., Pintar, F. A., McCrea, M., Kurpad, S. N., Glavaski-Joksimovic, A., Olsen, C., & Budde, M. D. (2015). Head Rotational Acceleration Characteristics Influence Behavioral and Diffusion Tensor Imaging Outcomes Following Concussion. *Annals of Biomedical Engineering*, *43*(5). https://doi.org/10.1007/s10439-014-1171-9

Stocchetti, N., & Zanier, E. R. (2016). Chronic impact of traumatic brain injury on outcome and quality of life: A narrative review. In *Critical Care, 20*(1). https://doi.org/10.1186/s13054-016-1318-1

Stroop, R., Thomale, U. W., Päuser, S., Bernarding, J., Vollmann, W., Wolf, K. J., Lanksch, W. R., & Unterberg, A. W. (1998). Magnetic Resonance Imaging Studies with Cluster Algorithm for Characterization of Brain Edema after Controlled Cortical Impact Injury (CCII). *Acta Neurochirurgica, Supplement*, *71*. https://doi.org/10.1007/978-3-7091-6475-4_88

Sun, S. W., Neil, J. J., & Song, S. K. (2003). Relative indices of water diffusion anisotropy are equivalent in live and formalin-fixed mouse brains. *Magnetic Resonance in Medicine*, *50*(4). https://doi.org/10.1002/mrm.10605

Suskauer, S. J., & Huisman, T. A. G. M. (2009). Neuroimaging in pediatric traumatic brain injury: Current and future predictors of functional outcome. In *Developmental Disabilities Research Reviews, 15*(2). https://doi.org/10.1002/ddrr.62

Symms, M., Jäger, H. R., Schmierer, K., & Yousry, T. A. (2004). A review of structural magnetic resonance neuroimaging. In *Journal of Neurology, Neurosurgery and Psychiatry, 75*(9). https://doi.org/10.1136/jnnp.2003.032714

Tae, W. S., Ham, B. J., Pyun, S. B., Kang, S. H., & Kim, B. J. (2018). Current clinical applications of diffusion-tensor imaging in neurological disorders. In *Journal of Clinical Neurology (Korea)*,*14*(2). https://doi.org/10.3988/jcn.2018.14.2.129

Thompson, H. J., Lifshitz, J., Marklund, N., Grady, M. S., Graham, D. I., Hovda, D. A., & Mcintosh, T. K. (2005). Lateral fluid percussion brain injury: A 15-year review and evaluation. In *Journal of Neurotrauma, 22*(1). https://doi.org/10.1089/neu.2005.22.42

Tong, K. A., Ashwal, S., Holshouser, B. A., Nickerson, J. P., Wall, C. J., Shutter, L. A., Osterdock, R. J., Haacke, E. M., & Kido, D. (2004). Diffuse axonal injury in children: Clinical correlation with hemorrhagic lesions. *Annals of Neurology*, *56*(1). https://doi.org/10.1002/ana.20123

Tong, K. A., Ashwal, S., Holshouser, B. A., Shutter, L. A., Herigault, G., Haacke, E. M., & Kido, D. K. (2003). Hemorrhagic shearing lesions in children and adolescents with posttraumatic diffuse axonal injury: Improved detection and initial results. *Radiology*, *227*(2). https://doi.org/10.1148/radiol.2272020176

Tournier, J. D., Calamante, F., Gadian, D. G., & Connelly, A. (2004). Direct estimation of the fiber orientation density function from diffusion-weighted MRI data using spherical deconvolution. *NeuroImage*, *23*(3). https://doi.org/10.1016/j.neuroimage.2004.07.037

Tournier, J. D., Calamante, F., & Connelly, A. (2007). Robust determination of the fibre orientation distribution in diffusion MRI: Non-negativity constrained super-resolved spherical deconvolution. *NeuroImage*, *35*(4). https://doi.org/10.1016/j.neuroimage.2007.02.016

Tournier, J.-D., & , F. Calamante, and a. C. (2010). Improved probabilistic streamlines tractography by 2nd order integration over fibre orientation distributions. In *Proc. Joint Annual Meeting of the ISMRM-ESMRMB, Stockholm, Sweden.*

Tournier, J. D., Mori, S., & Leemans, A. (2011). Diffusion tensor imaging and beyond. In *Magnetic Resonance in Medicine, 65*(6). https://doi.org/10.1002/mrm.22924

Tournier, J. D., Calamante, F., & Connelly, A. (2013). Determination of the appropriate b value and number of gradient directions for high-angular-resolution diffusion-weighted imaging. *NMR in Biomedicine*, *26*(12). https://doi.org/10.1002/nbm.3017

Tournier, J. D., Smith, R., Raffelt, D., Tabbara, R., Dhollander, T., Pietsch, M., Christiaens, D., Jeurissen, B., Yeh, C. H., & Connelly, A. (2019). MRtrix3:

A fast, flexible and open software framework for medical image processing and visualisation. In *NeuroImage, 202*. https://doi.org/10.1016/j.neuroimage.2019.116137

Tuch, D. S., Reese, T. G., Wiegell, M. R., Makris, N., Belliveau, J. W., & van Wedeen, J. (2002). High angular resolution diffusion imaging reveals intravoxel white matter fiber heterogeneity. *Magnetic Resonance in Medicine*, *48*(4). https://doi.org/10.1002/mrm.10268

Tustison, N. J., Avants, B. B., Cook, P. A., Zheng, Y., Egan, A., Yushkevich, P. A., & Gee, J. C. (2010). N4ITK: Improved N3 bias correction. *IEEE Transactions on Medical Imaging*, *29*(6). https://doi.org/10.1109/TMI.2010.2046908

Unterberg, A. W., Stroop, R., Thomale, U. W., Kiening, K. L., Päuser, S., & Vollmann, W. (1997). Characterisation of Brain Edema Following "Controlled Cortical Impact Injury" in Rats. *Acta Neurochirurgica, Supplement*, *70*. https://doi.org/10.1007/978-3-7091-6837-0_33

Vallat, R. (2018). Pingouin: statistics in Python. *Journal of Open Source Software*, *3*(31). https://doi.org/10.21105/joss.01026

van der Naalt, J., Timmerman, M. E., de Koning, M. E., van der Horn, H. J., Scheenen, M. E., Jacobs, B., Hageman, G., Yilmaz, T., Roks, G., & Spikman, J. M. (2017). Early predictors of outcome after mild traumatic brain injury (UPFRONT): an observational cohort study. *The Lancet Neurology*, *16*(7). https://doi.org/10.1016/S1474-4422(17)30117-5

Veraart, J., Fieremans, E., & Novikov, D. S. (2019). On the scaling behavior of water diffusion in human brain white matter. *NeuroImage*, *185*. https://doi.org/10.1016/j.neuroimage.2018.09.075

Veraart, J., Sijbers, J., Sunaert, S., Leemans, A., & Jeurissen, B. (2013). Weighted linear least squares estimation of diffusion MRI parameters: Strengths, limitations, and pitfalls. *NeuroImage*, *81*. https://doi.org/10.1016/j.neuroimage.2013.05.028

Verhelst, H., Giraldo, D., vander Linden, C., Vingerhoets, G., Jeurissen, B., & Caeyenberghs, K. (2019). Cognitive Training in Young Patients With Traumatic Brain Injury: A Fixel-Based Analysis. *Neurorehabilitation and Neural Repair*, *33*(10). https://doi.org/10.1177/1545968319868720

Virtanen, P., Gommers, R., Oliphant, T. E., Haberland, M., Reddy, T., Cournapeau, D., Burovski, E., Peterson, P., Weckesser, W., Bright, J., van der Walt, S. J., Brett, M., Wilson, J., Millman, K. J., Mayorov, N., Nelson, A. R. J., Jones, E., Kern, R., Larson, E., … Vázquez-Baeza, Y. (2020). SciPy 1.0: fundamental algorithms for scientific computing in Python. *Nature Methods*, *17*(3). https://doi.org/10.1038/s41592-019-0686-2

Wang, C., Song, L., Zhang, R., & Gao, F. (2018). Impact of fixation, coil, and number of excitations on diffusion tensor imaging of rat brains at 7.0 T. *European Radiology Experimental*, *2*(1). https://doi.org/10.1186/s41747-018-0057-2

Wang, K. (2018). *Neurotrauma: A Comprehensive Textbook on Traumatic Brain Injury and Spinal Cord Injury*. OXFORD University Press. https://books.google.co.uk/books?id=TlByDwAAQBAJ

Wang, Y., & Liu, T. (2015). Quantitative susceptibility mapping (QSM): Decoding MRI data for a tissue magnetic biomarker. *Magnetic Resonance in Medicine*, *73*(1). https://doi.org/10.1002/mrm.25358

Wesbey, G. E., Moseley, M. E., & Ehman, R. L. (1984). Translational molecular self-diffusion in magnetic resonance imaging: II. Measurement of the self-diffusion coefficient. *Investigative Radiology*, *19*(6). https://doi.org/10.1097/00004424-198411000-00005

Wharton, S., Schäfer, A., & Bowtell, R. (2010). Susceptibility mapping in the human brain using threshold-based k-space division. *Magnetic Resonance in Medicine*, *63*(5). https://doi.org/10.1002/mrm.22334

Wheeler-Kingshott, C. A. M., & Cercignani, M. (2009). About "axial" and "radial" diffusivities. *Magnetic Resonance in Medicine*, *61*(5). https://doi.org/10.1002/mrm.21965

Wiegand, T. L. T., Sollmann, N., Bonke, E. M., Umeasalugo, K. E., Sobolewski, K. R., Plesnila, N., Shenton, M. E., Lin, A. P., & Koerte, I. K. (2022). Translational neuroimaging in mild traumatic brain injury. In *Journal of Neuroscience Research, 100*(5). https://doi.org/10.1002/jnr.24840

Wisnieff, C., Ramanan, S., Olesik, J., Gauthier, S., Wang, Y., & Pitt, D. (2015). Quantitative susceptibility mapping (QSM) of white matter multiple sclerosis lesions: Interpreting positive susceptibility and the presence

of iron. *Magnetic Resonance in Medicine*, *74*(2). https://doi.org/10.1002/mrm.25420

Wright, D. K., Johnston, L. A., Kershaw, J., Ordidge, R., O'Brien, T. J., & Shultz, S. R. (2017). Changes in Apparent Fiber Density and Track-Weighted Imaging Metrics in White Matter following Experimental Traumatic Brain Injury. *Journal of Neurotrauma*, *34*(13). https://doi.org/10.1089/neu.2016.4730

Wu, D., Xu, J., McMahon, M. T., van Zijl, P. C. M., Mori, S., Northington, F. J., & Zhang, J. (2013). In vivo high-resolution diffusion tensor imaging of the mouse brain. *NeuroImage*, *83*. https://doi.org/10.1016/j.neuroimage.2013.06.012

Xiong, Y., Mahmood, A., & Chopp, M. (2013). Animal models of traumatic brain injury. In *Nature Reviews Neuroscience, 14*(2). https://doi.org/10.1038/nrn3407

Yamada, N., Imakita, S., Sakuma, T., & Takamiya, M. (1996). Intracranial calcification on gradient-echo phase image: Depiction of diamagnetic susceptibility. *Radiology*, *198*(1). https://doi.org/10.1148/radiology.198.1.8539373

Yang, J. Y. M., Yeh, C. H., Poupon, C., & Calamante, F. (2021). Diffusion MRI tractography for neurosurgery: The basics, current state, technical reliability and challenges. In *Physics in Medicine and Biology, 66*(15). https://doi.org/10.1088/1361-6560/ac0d90

Yang, Z., Zhu, T., Pompilus, M., Fu, Y., Zhu, J., Arjona, K., Arja, R. D., Grudny, M. M., Plant, H. D., Bose, P., Wang, K. K., & Febo, M. (2021). Compensatory functional connectome changes in a rat model of traumatic brain injury. *Brain Communications*, *3*(4). https://doi.org/10.1093/braincomms/fcab244

Zamani, A., O'Brien, T. J., Kershaw, J., Johnston, L. A., Semple, B. D., & Wright, D. K. (2021). White matter changes following experimental pediatric traumatic brain injury: an advanced diffusion-weighted imaging investigation. *Brain Imaging and Behavior*, *15*(6). https://doi.org/10.1007/s11682-020-00433-0

Zhang, H., Schneider, T., Wheeler-Kingshott, C. A., & Alexander, D. C. (2012). NODDI: Practical in vivo neurite orientation dispersion and density

imaging of the human brain. *NeuroImage*, *61*(4). https://doi.org/10.1016/j.neuroimage.2012.03.072

Zhong, K., Leupold, J., von Elverfeldt, D., & Speck, O. (2008). The molecular basis for gray and white matter contrast in phase imaging. *NeuroImage*, *40*(4). https://doi.org/10.1016/j.neuroimage.2008.01.061

Zhu, W. Z., Qi, J. P., Zhan, C. J., Shu, H. G., Zhang, L., Wang, C. Y., Xia, L. M., Hu, J. W., & Feng, D. Y. (2008). Magnetic resonance susceptibility weighted imaging in detecting intracranial calcification and hemorrhage. *Chinese Medical Journal*, *121*(20). https://doi.org/10.1097/00029330-200810020-00014

ORIGINAL PUBLICATIONS (I – III)

I

Quantitative susceptibility mapping of the rat brain after traumatic brain injury

Chary K, Nissi M J, Nykänen, Manninen, E, Rey R I, Shmueli K, Sierra A and Gröhn O

NMR in biomedicine 34: e4438, 2020

II

Microstructural changes in a rat model of mild traumatic brain injury

Chary K, Narvaez O, Salo R A, Molina ISM, Tohka J, Aggarwal M, Gröhn O and Sierra A

Frontiers in Neuroscience 15: 746214, 2021

frontiers in Neuroscience

ORIGINAL RESEARCH
published: 26 November 2021
doi: 10.3389/fnins.2021.746214

Microstructural Tissue Changes in a Rat Model of Mild Traumatic Brain Injury

Karthik Chary[1†], Omar Narvaez[1†], Raimo A. Salo[1], Isabel San Martín Molina[1], Jussi Tohka[1], Manisha Aggarwal[2], Olli Gröhn[1] and Alejandra Sierra[1]*

[1] A. I. Virtanen Institute for Molecular Sciences, University of Eastern Finland, Kuopio, Finland, [2] Russell H. Morgan Department of Radiology and Radiological Science, The Johns Hopkins University School of Medicine, Baltimore, MD, United States

Our study investigates the potential of diffusion MRI (dMRI), including diffusion tensor imaging (DTI), fixel-based analysis (FBA) and neurite orientation dispersion and density imaging (NODDI), to detect microstructural tissue abnormalities in rats after mild traumatic brain injury (mTBI). The brains of sham-operated and mTBI rats 35 days after lateral fluid percussion injury were imaged *ex vivo* in a 11.7-T scanner. Voxel-based analyses of DTI-, fixel- and NODDI-based metrics detected extensive tissue changes in directly affected brain areas close to the primary injury, and more importantly, also in distal areas connected to primary injury and indirectly affected by the secondary injury mechanisms. Histology revealed ongoing axonal abnormalities and inflammation, 35 days after the injury, in the brain areas highlighted in the group analyses. Fractional anisotropy (FA), fiber density (FD) and fiber density and fiber bundle cross-section (FDC) showed similar pattern of significant areas throughout the brain; however, FA showed more significant voxels in gray matter areas, while FD and FDC in white matter areas, and orientation dispersion index (ODI) in areas most damage based on histology. Region-of-interest (ROI)-based analyses on dMRI maps and histology in selected brain regions revealed that the changes in MRI parameters could be attributed to both alterations in myelinated fiber bundles and increased cellularity. This study demonstrates that the combination of dMRI methods can provide a more complete insight into the microstructural alterations in white and gray matter after mTBI, which may aid diagnosis and prognosis following a mild brain injury.

Keywords: traumatic brain injury, fixel-based analysis, diffusion tensor imaging, axonal damage, gliosis, histology, neurite orientation dispersion and density imaging

OPEN ACCESS

Edited by:
Maxime Descoteaux, Université de Sherbrooke, Canada

Reviewed by:
Guido Guberman, McGill University, Canada
Matthew D. Budde, Medical College of Wisconsin, United States
Sudhir Kumar Pathak, University of Pittsburgh, United States

****Correspondence:***
Alejandra Sierra
alejandra.sierralopez@uef.fi

[†]These authors share first authorship

Specialty section:
This article was submitted to Brain Imaging Methods, a section of the journal Frontiers in Neuroscience

Received: *23 July 2021*
Accepted: *27 October 2021*
Published: *26 November 2021*

Citation:
Chary K, Narvaez O, Salo RA, San Martín Molina I, Tohka J, Aggarwal M, Gröhn O and Sierra A (2021) Microstructural Tissue Changes in a Rat Model of Mild Traumatic Brain Injury. Front. Neurosci. 15:746214. doi: 10.3389/fnins.2021.746214

Abbreviations: AD, axial diffusivity; AI, anisotropy index; CD, cellular density; CFE, connectivity-based fixel enhancement; CSD, constrained spherical deconvolution; CT, computed tomography; DTI, diffusion tensor imaging; dMRI, diffusion magnetic resonance imaging; DW-GRASE, diffusion-weighted gradient- and spin-echo; FA, fractional anisotropy; FBA, fixel-based analysis; FC, fiber bundle cross-section; FD, fiber density; FDC, fiber density and fiber bundle cross-section; FOD, fiber orientation distribution; FWE, family-wise error; FWF, free water fraction; GM, gray matter; HARDI, high-angular-resolution diffusion imaging; LFP, lateral fluid percussion; MD, mean diffusivity; MRI, magnetic resonance imaging; mTBI, mild traumatic brain injury; NODDI, neurite orientation dispersion and density imaging; NDI, neurite density index; ODI, orientation dispersion index; PBS, phosphate-buffered saline; RD, radial diffusivity; ROI, region-of-interest; ST, structure tensor; TFCE, threshold-free cluster enhancement; VBA, voxel-based analyses; WM, white matter.

INTRODUCTION

Magnetic resonance imaging (MRI) and computed tomography (CT) are routinely used to assess tissue damage in patients after traumatic brain injury (TBI; Duhaime et al., 2010). While these imaging methodologies can assess tissue damage after moderate and severe injury, mild TBI (mTBI) remains a challenge by not providing clear radiological evidence of brain injury (Mittl et al., 1994; Iverson et al., 2000; Scheid et al., 2003; Hughes et al., 2004). Clinically, mTBI is defined by initial brief, decreased, or no loss of consciousness, disorientation, or amnesia, which tend to disappear within minutes or hours after injury (Mechtler et al., 2014; Pervez et al., 2018). However, many patients complain about persisting symptoms for days or even months after the injury, such as headache, dizziness, concentration/memory problems, or other long-term complications, such as sleeping disorders, emotional distress, depression, or anxiety (Katz et al., 2015; Ling et al., 2015; Cole and Bailie, 2016; van der Naalt et al., 2017). These short- and long term-consequences after a mild injury indicate that there are still ongoing processes in the brain, which are not detected by the clinically available imaging methods.

Diffusion MRI (dMRI) detects the displacement of water molecules, which reflects tissue microstructure. Therefore, changes in the tissue microenvironment can provide non-invasively detectable information associated to pathological processes ongoing in the tissue. In particular, diffusion tensor imaging (DTI; Basser et al., 1994) has demonstrated a good sensitivity to reveal microstructure-associated changes of pathological features of mTBI both in patients (Inglese et al., 2005; Yuh et al., 2014; Asken et al., 2018; Wallace et al., 2018; Yin et al., 2019) and animal models of TBI (Bennett et al., 2012; Hylin et al., 2013; Stemper et al., 2015; Herrera et al., 2017; Hutchinson et al., 2018). Despite being widely used, the single tensor model assumes one water pool with Gaussian distribution, which oversimplifies the highly complex architecture of the tissue within a voxel. For example, it has been studied that white matter voxels may contain up to 90% of crossing fibers (Jeurissen et al., 2013). Therefore, differences detected in a region-of-interest (ROI) or voxel-based analyses are confounded by partial volume effects making interpretation of DTI outcomes a challenge in the presence of multiple fiber bundles or in the gray matter (Jones et al., 2013). Recently, the introduction of more advanced techniques, such as high-angular-resolution diffusion imaging (HARDI) acquisitions (Tuch et al., 2002) in combination with higher-order diffusion modeling tools, such as constrained spherical deconvolution (CSD; Tournier et al., 2004, 2007), Q-ball (Tuch, 2004) or persistent angular structure-MRI (Jansons and Alexander, 2003), offer new windows to estimate the more complex microstructural environment of the brain tissue. Based on CSD, Raffelt et al. (2012) introduced a novel statistical analyses method for HARDI data known as fixel-based analysis (FBA), which enables quantification of individual fiber bundle populations within a voxel. More specifically, the FBA framework provides estimation of microstructural changes in apparent fiber density and macroscopic changes in fiber bundle cross-section (Raffelt et al., 2012, 2017). On the other hand, multi-compartment models, such as neurite orientation dispersion and density imaging (NODDI; Zhang et al., 2012), can extract information of volume fractions of isotropic, hindered, and restricted compartments and identify microstructural features associated with pathological process occurring in the brain. Both FBA framework and NODDI has been already used to assess tissue alterations after TBI in both animals and humans (Wright et al., 2017; Churchill et al., 2019; Verhelst et al., 2019; Gazdzinski et al., 2020; Palacios et al., 2020; Wallace et al., 2020; McCunn et al., 2021; Muller et al., 2021; Oehr et al., 2021), however, there are few studies including corroboration of the tissue changes after brain injury with histology.

The aim of our study was to investigate microstructural tissue changes throughout the brain in an experimental mTBI rat model using DTI-, fixel- and NODDI based analyses. We performed voxel-based analysis (VBA) comparing *ex vivo* sham-operated and mTBI brains of the DTI-based metrics: fractional anisotropy (FA), and axial (AD), radial (RD) and mean (MD) diffusivities; fixel-based metrics: fiber density (FD), fiber bundle cross-section (FC), and fiber density and fiber bundle cross-section (FDC); and NODDI metrics: orientation dispersion index (ODI), free water fraction (FWF), and neurite density index (NDI). Histologically, we confirmed axonal alterations and increased cell density associated to gliosis in highlighted brain areas in both analyses by using myelin and Nissl stainings, respectively. Additionally, we performed an ROI analysis on MRI and histology in the same animals, and correlated values from individual MRI maps with ones obtained from histological sections stained for myelin and Nissl. Altogether, this study explores the potential of established and advanced diffusion MRI techniques with histological validation, and more importantly, increases our understanding of tissue microstructural changes in the brain after mild injury.

MATERIALS AND METHODS

Animal Model

Experimental TBI was induced in male Sprague-Dawley rats ($n = 8$; 10 weeks old, 300–350 g, Harlan Netherlands B.V., Horst, Netherlands) by lateral fluid percussion (LFP) injury. Rats were anesthetized with a single i.p. injection (6 ml/kg) of a mixture containing sodium pentobarbital (Mebunat, Orion Pharma, Finland; 60 mg/kg), magnesium sulfate (127.2 mg/kg), propylene glycol (39.5%), and absolute ethanol (10%). Then, a craniectomy ($Ø = 5$ mm) was performed between bregma and lambda on the left skull convexity (anterior edge 2.0 mm posterior to the bregma; lateral edge adjacent to the left lateral ridge). A fluid percussion device (AmScien Instruments, Richmond, VA, United States) was then used to induce an LFP injury to the exposed dura using a transient fluid pulse (21–23 ms) to induce a mild injury (0.89 ± 0.21 atm). After the injury, we checked that the dura was intact. Sham-operated rats ($n = 6$) were subjected to same operational procedures except for the impact.

Following the operation, the animals were transferred to the animal facility and housed in individual cages maintained under

a 12 h light/12 h dark cycle (lights on 07:00 a.m., temperature 22 ± 1°C, humidity 50–60%) with free access to food and water. All animal procedures were carried out under licenses that have been approved by the Animal Ethics Committee of the Provincial Government of Southern Finland and in accordance with the guidelines of the European Community Council Directives 86/609/EREC.

Tissue Preparation

Thirty-five days after the operation, all the rats (n = 14) were deeply anesthetized under 5% isoflurane in 30%/70% O_2/N_2 gas mixture, and transcardially perfused with saline for 2 min (30 ml/min) followed by 4% paraformaldehyde in 0.1 M phosphate buffer, pH 7.4 (30 ml/min) for 25 min. After perfusion, the brains were removed from the skull and post-fixed in a solution of 4% paraformaldehyde until imaging. Before MRI, the brains were transferred to a solution of 0.1 M phosphate-buffered saline (PBS) containing 1 mM gadopentetate dimeglumine (Magnevist, Berlex Imaging, Wayne, NJ, United States) for at least 72 h. The brains were then placed tightly inside a polyethylene tube filled with perfluoro polyether (Fomblin, Solvay Inc., Princeton, NJ, United States) to prevent tissue drying and to effectively suppress the background signal.

Ex vivo Magnetic Resonance Imaging Acquisition

The brains were scanned on an 11.7 T NMR spectrometer (Bruker BioSpin, Billerica, MA, United States), with a Micro2.5 gradient system (maximum gradient strength = 1,000 mT/m). A 20-mm-diameter birdcage volume coil was used for radiofrequency transmission and signal reception. Diffusion data were acquired using a 3D diffusion-weighted gradient- and spin-echo (DW-GRASE) sequence (Aggarwal et al., 2010) with TR/TE = 800/33 ms, rare-factor/EPI factor = 4/3, bandwidth = 100 kHz, number of averages = 2, FOV = 22.8 mm × 16.8 mm × 11.7 mm, matrix size (read × phase × phase 2) = 152 × 112 × 78, acquired spatial resolution = 150 μm^3 isotropic (zero-filling interpolation to 0.075 mm^3 isotropic), number of uniformly distributed diffusion directions = 30 for each b-value of 3,000 and 6,000 s/mm^2, number of minimally diffusion-weighted images = 3, diffusion gradient duration (δ)/separation (Δ) = 5/12 ms, total acquisition time ∼21 h.

Image Pre-processing

k-space data were processed using in-house code in IDL (ITT Visual Information Solutions, Boulder, CO, United States) to reconstruct the diffusion weighted images. Preprocessing of the reconstructed data consisted of image denoising based on random matrix theory (Cordero-Grande et al., 2019) and Gibbs ringing removal using the method of local subvoxel-shifts (Kellner et al., 2016), both tools included in the MRtrix3 software (Tournier et al., 2019). Finally, bias field correction was applied to remove spatial intensity inhomogeneities (Tustison et al., 2010) followed by motion and eddy current correction using Advanced Normalization Tools (ANTs) software (Avants et al., 2014).

Fixel-Based, Tensor-Based and Neurite Orientation Dispersion and Density Imaging Analyses

To perform FBA (Raffelt et al., 2012), tissue specific response functions were estimated for white matter (WM), gray matter (GM), and PBS in an unsupervised manner for each sham-operated animal (Dhollander and Connelly, 2016), and combined to create group averaged response functions. Whole brain masks were obtained for each image. The fiber orientation distributions (FODs) with a spherical harmonic degree (lmax = 6) were then estimated from the group averaged response functions using multi-shell, multi-tissue constrained spherical deconvolution (MSMT-CSD; Jeurissen et al., 2014). The resulting FODs were corrected for intensity inhomogeneities using multi-tissue-informed intensity normalization.

Unbiased Population Template

The FOD maps from all the brains, including sham-operated and mTBI, were then co-registered in two steps; first with rigid and affine registration followed by a non-linear registration to optimize a group-average template. The linear and non-linear warps generated during co-registration were subsequently used to warp (without orientation) the intensity normalized FODs from each rat to the template.

Fixel-Based Metrics: Fiber Density, Fiber Bundle Cross-Section, Fiber Density and Fiber Bundle Cross-Section

To ensure that further analysis is performed on fixels that contain data from all the rat brains, all the individual masks were warped to the template, and the intersection of the masks were computed to obtain a population template mask. Then, a white matter template fixel mask was created by segmenting the peak FOD amplitudes of each fixel in the FOD based template, at a threshold of 0.06. The selected threshold for the fixel mask was chosen to include fixels in crossing fiber areas that are genuinely in WM and areas with a mixture of WM and GM, without the inclusion of any spurious fixels. Each FOD lobe from the warped individual rat brain FODs were segmented into corresponding fixels by taking the integral of the FOD lobe (at the threshold defined previously) to obtain the FD per fixel and reoriented into the template image (Raffelt et al., 2012). The fixel spatial correspondence was achieved by taking each reoriented fixel in the individual rat brain FODs and assigning it to the corresponding fixel in the FOD template (Raffelt et al., 2017). The FC metric was computed from the deformation fields obtained during co-registration (from the individual to template). Finally, FDC metric was computed by modulating the FD with FC computed previously.

Tensor-Based and Multicompartment Model Neurite Orientation Dispersion and Density Imaging Analyses

We calculated tensor-based metrics using both b-values (i.e., 3,000 and 6,000 s/mm^2) and the iteratively weighted least-squares (IWLS) method to improve accuracy in the parameter estimations (Basser et al., 1994; Veraart et al., 2013). The tensor-based metrics included were fractional anisotropy (FA), axial diffusivity (AD), radial diffusivity (RD), and

mean diffusivity (MD). Multicompartment model NODDI was computed and fitted using the NODDI toolbox (UCL, United Kingdom) for Matlab[1]. The derived NODDI indices included orientation dispersion index (ODI), free water fraction (FWF), and neurite density index (NDI). For the voxel-wise analysis, the tensor- and NODDI-based metrics were then warped to the FOD-based template using the non-linear transformations obtained during FBA analysis.

Statistical Analysis

Statistical analysis for fixel-based metrics were performed by connectivity-based fixel enhancement (CFE) which uses whole brain tractography-derived connectivity information to infer the amount of cluster-like local spatial support for each corresponding voxel (Raffelt et al., 2015). For this purpose, whole-brain tractography was performed on the study-specific FOD template within the template mask intersection using the iFOD2 algorithm by generating 20 million streamlines, angle = 22.5°, minimum length = 0.3 mm, maximum length = 22.5 mm, cutoff = 0.06, power = 1. In order to minimize errors between tractography-derived streamline densities and spherical deconvolution-derived fiber densities, the resulting tractogram was reduced to 2 million streamlines using spherical-deconvolution-informed filtering of tractograms (SIFT; Smith et al., 2013). Connectivity-based fixel enhancement was performed for the group analysis FD, FC, and FDC metrics comparing sham-operated versus mTBI rats applying a spatial Gaussian filter of 0.3 mm × 0.3 mm × 0.3 mm and using general linear model with non-parametric permutation testing (5,000 permutations) using the default MRtrix3 *fixelcfestats* tool parameters (C = 0.5, E = 2, H = 3) (Raffelt et al., 2015). For voxel-based metrics, a spatial Gaussian filter of 0.3 mm × 0.3 mm × 0.3 mm was applied to the data and the statistical analysis was performed with non-parametric permutation testing (5,000 permutations) using threshold-free cluster enhancement (TFCE) with the default FSL *randomize* tool parameters (C = 6, E = 0.5, H = 2) (Smith and Nichols, 2009). Both the DTI- and fixel-based voxel-wise statistical analyses were fully corrected for family-wise error (FWE). A p-value of less than 0.05 was considered statistically significant.

We pre-selected the regions of interest based on histology in the same animals as in MRI. We selected the corpus callosum and external capsule at −1.80 and −3.50 mm from bregma, and internal capsule and ventrobasal complex at −3.50 mm from bregma, both ipsi- and contralaterally. A single set of ROIs were manually drawn in the template. The selection of ROIs was based on our previous study (San Martín Molina et al., 2020). Then, the ROIs were transformed to the subject space using the inverse matrix transformation for each brain. The ROI-based analysis for histology comparison was performed for tensor-based (FA, RD, AD, and MD) and CSD-based metrics (FD, dispersion, and peak), as well as NODDI parameters (ODI, FWF, and NDI). The ROI-based analysis of FC and FDC were also included but note that these metrics requires the non-linear transformations used to generate the template, hence, the corresponded ROIs were calculated in template space.

[1]http://nitrc.org/projects/noddi_tolbox

Histological Procedures and Analysis

The histological procedures and ROI analysis were presented in our previous study (San Martín Molina et al., 2020). In brief, after *ex vivo* imaging, the brains were washed in 0.9% NaCl for at least for 2 h at 4°C. After this, they were placed in a cryoprotective solution containing 20% glycerol in 0.02 M potassium phosphate-buffered saline (pH = 7.4) for 36 h. Then, the brains were blocked, frozen in dry ice, and preserved at −70°C until sectioning. The brains were sectioned in the coronal plane (30 μm, 1-in-5 series) using a sliding microtome. Sections from the first series were stored in 10% formalin while the remaining series were stored in a cryoprotectant tissue-collecting solution (30% ethylene glycol, 25% glycerol in 0.05 M sodium phosphate buffer) at −20°C until further processing. The first series of sections was stained with Nissl (thionin) and the second series with a gold chloride solution for myelin (Laitinen et al., 2010).

For the quantitative analysis, we selected brain areas that showed microstructural changes in the group analysis and were of interest in the TBI pathology (Laitinen et al., 2015; San Martín Molina et al., 2020; Chary et al., 2021). These brain areas were the corpus callosum and external capsule at −1.80 and −3.50 mm from bregma, internal capsule and ventrobasal complex at −3.50 mm from bregma. All the analyses were performed on high-resolution photomicrographs of the sections acquired at a resolution of 0.013 μm^2/pixel using a light microscope (Zeiss Axio Imager 2, White Plains, NY, United States) equipped with a digital camera (Zeiss Axiocam color 506). We performed structure tensor (ST) and derived the anisotropy index (AI; Budde et al., 2011), which correlates strongly with alternative dispersion measures, from myelin-stained sections, and cell density (CD) from Nissl-stained sections using an in-house Matlab code for automated cell counting analysis (San Martín Molina et al., 2020).

Region-of-Interest Statistical Analyses

All data were analyzed using GraphPad Prism software (version 5.03 for Windows, La Jolla, CA, United States). Differences between sham-operated and mTBI rats were assessed using the unpaired two-sample t-test, and differences between ipsi- and contralateral brain areas within the same brain using the paired t-test. Pearson's correlation was used to correlate dMRI and histological metrics. The Benjamini-Hochberg false discovery rate (FDR) method was used for multiple comparison corrections in both tests, and FDR-threshold $q < 0.05$ was chosen for statistical significance (Benjamini and Hochberg, 1995).

RESULTS

Figure 1 shows the outcomes from the group analyses in FA, AD, FD, FC, FDC, and ODI maps when comparing mTBI and sham-operated rats. The epicenter of the primary lesion in mTBI animals was at approximately −3.50 mm from bregma (asterisk in **Figure 1**), where we found the most extensive significant changes between the groups. The secondary damage expanded into connected areas throughout the brain at 35 days after the initial injury. These five parameters showed significant

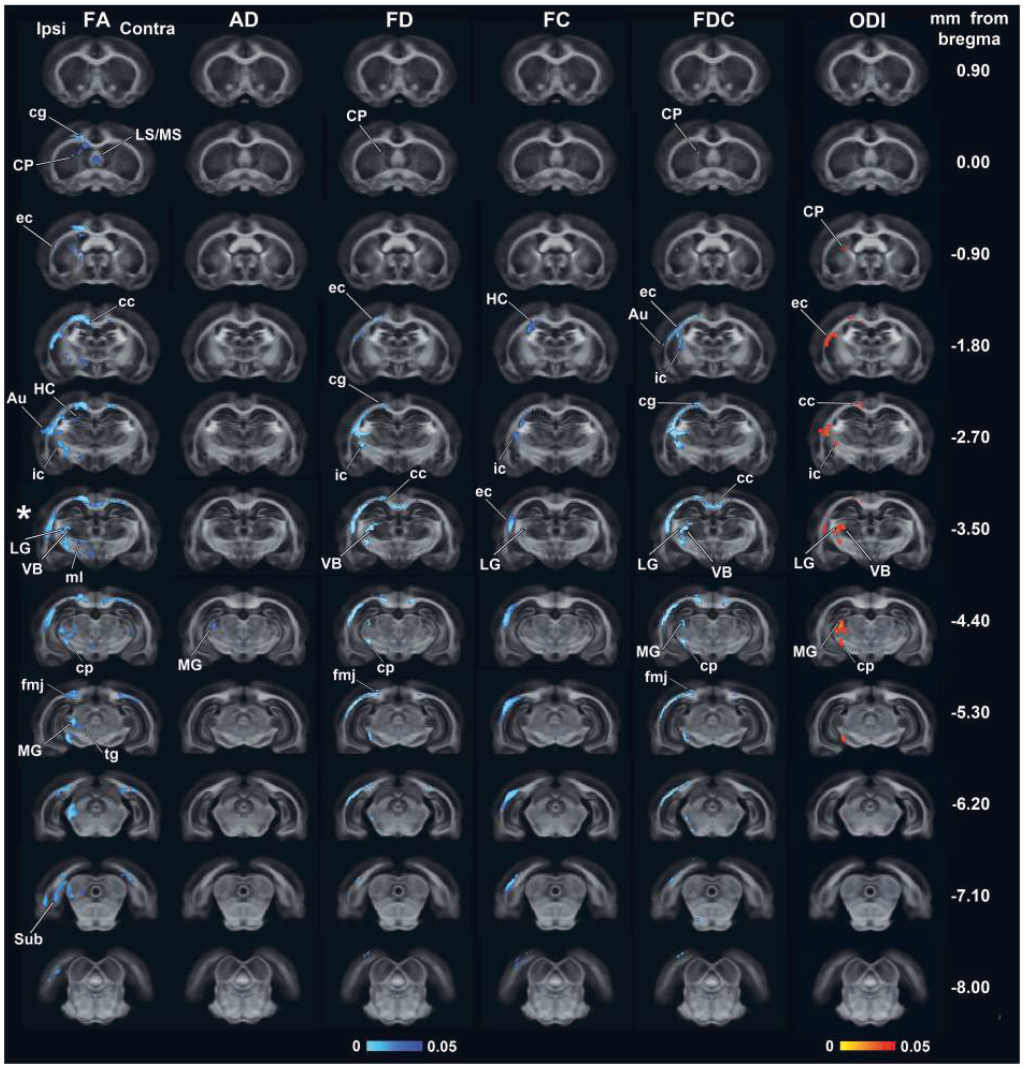

FIGURE 1 | Whole-brain group differences in FA, AD, FD, FC, FDC, and ODI metrics when comparing sham-operated and mTBI rats after 35 days of the sham-operation or injury. Areas displaying significant group differences in mTBI versus sham-operated rats (TFCE, p-value < 0.05, FWE-corrected) are overlaid on the FOD-based template. Significances are displayed as voxels in a light-dark blue scale, representing mTBI group values lower than sham-operated group values, and in a red-yellow scale, representing mTBI group values higher than sham-operated group values. The asterisk shows the epicenter of the lesion. Au, auditory cortex; cc, corpus callosum; cg, cingulum; cp, cerebral peduncle; CP, caudate putamen; ec, external capsule; fmj, forceps minor of the corpus callosum; HC, hippocampus; ic, internal capsule; LG, lateral geniculate nuclei; LS/MS, lateral/medial septal nucleus; MG, medial geniculate nucleus; ml, medial lemniscus; Sub, subiculum; tg, tegmental nuclei; VB, ventrobasal complex.

decreases (TFCE, p-value < 0.05, FWE-corrected) in mTBI rats compared to sham-operated ones. From the DTI parameters, FA significantly decreased in both white and gray matter areas throughout the brain and AD showed few highlighted voxels in the midbrain. FD and FDC showed similar pattern of changes than FA, while the results in FC were restricted to few damaged areas. ODI significantly increased in the closed areas to the primary injury, mainly white matter and thalamic areas, which were also shown in FA, FD, and FDC maps.

Figure 2 shows representative photomicrographs of myelin-stained sections from a sham-operated and mTBI rat 35 days after the sham-operation or injury. We observed two microstructural

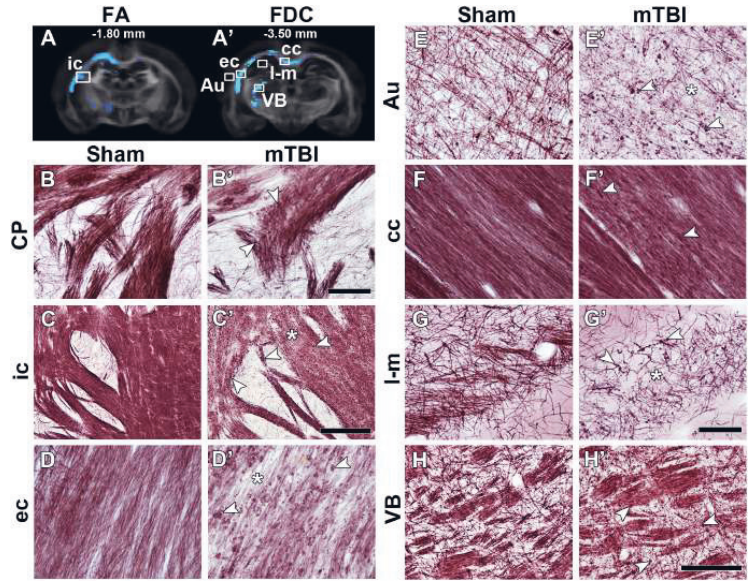

FIGURE 2 | FA **(A)** and FDC **(A')** at –1.80 and –3.50 mm from bregma, respectively, from the group analyses. White squares indicate the location of the photomicrographs shown in **(B–H)**. Representative photomicrographs of myelin-stained sections of a sham-operated and a mTBI rat from the caudate putamen **(B,B')** from –0.90 mm (not shown in **A**), internal capsule **(C,C')** from –1.80 mm, and external capsule **(D,D')**, auditory cortex **(E,E')**, corpus callosum **(F,F')**, stratum-lacunosum moleculare **(G,G')**, and ventrobasal complex **(H,H')** from –3.50 mm from bregma. White arrowheads point at myelin alterations associated with axonal damage and asterisks indicate areas with extensive decrease in density of myelinated axons. AI values of these two animals shown in this figure are shown in **Supplementary Table 1**. Au, auditory cortex; cc, corpus callosum; CP, caudate putamen; ec, external capsule; ic, internal capsule; l-m, stratum-lacunosum moleculare; VB, ventrobasal complex. Scale bars: 50 μm **(B,B',D,D'–G,G')**, 150 μm **(H,H')**, and 250 μm **(C,C')**.

alterations in mTBI animals when compared to sham-operated rats: axonal alterations shown as dark accumulation of staining (arrowheads in **Figure 2**) and decreased axonal density (asterisks in **Figure 2**). Axonal alterations are associated to axonal injury and/or myelin damage, which were consistently found in all areas exhibiting group differences, in all the animals. We observed wide-spread axonal alterations rostrally in the brain, such as in the caudate putamen (arrowheads in **Figure 2B'**), which appeared more numerous and closer to the epicenter of the primary lesion, as in the internal capsule (**Figure 2C'**), external capsule (**Figure 2D'**), cortex (**Figure 2E'**), and ventrobasal complex (**Figure 2H'**). Decrease in axonal density was found in the internal capsule (**Figure 2C'**), external capsule (**Figure 2D'**), auditory cortex (**Figure 2E'**), and stratum-lacunosum moleculare (**Figure 2G'**). In the corpus callosum, we observed axonal alterations along the structure ipsi- and contralaterally, and a decrease in axonal density (**Figure 2F'**); however, not so prominent as in other areas. We also observed the thinning of fiber bundles in the internal capsule at the level of the caudate putamen (arrow in **Figure 2C'**).

Figure 3 shows representative photomicrographs of Nissl-stained sections from a sham-operated and mTBI rat 35 days after the sham-operation or injury. We found a wide-spread increase in cell density, associated to gliosis, rostrally in the brain as in the caudate putamen (**Figure 3B'**). Gliosis was more evident closer to the epicenter of the primary lesion, as in the internal capsule (**Figure 3C'**), external capsule (**Figure 3D'**), cortex (**Figure 3E'**), corpus callosum (**Figure 3F'**), and ventrobasal complex (**Figure 3H'**). We observed a decrease in cell density in the stratum-lacunosum moleculare (**Figure 3G'**) along with the loss of fiber bundles in the layer (asterisk in **Figure 2G'**).

We performed an ROI analysis of specific brain regions on MRI maps at the perilesional and epicenter sites; −1.80 and −3.50 mm from bregma, respectively (**Figures 4–6**). We found significant decrease in FA ipsilaterally in mTBI rats when comparing within mTBI animals and/or between sham-operated and mTBI rats at −3.50 mm from bregma (**Figure 4A**). AD decreased ipsilaterally in the mTBI rats in the corpus callosum and internal capsule at the epicenter (**Figure 4B**). On the contrary, RD (**Figure 4C**) and MD (**Figure 4D**) increased at −1.80 mm in the corpus callosum and/or at −3.50 mm in the internal capsule. It is worth noting that sham-operated rats ipsilaterally showed significant differences as compared to the contralateral side in the ROI analysis, such as FA and AD in the external capsule (**Figures 4A,B**), MD in the corpus callosum and external capsule at −1.80 mm, or internal capsule (**Figure 4D**).

We did not find significant differences in dispersion values in any of the brain areas (**Figure 5A**). Peak FOD amplitudes showed a significant decrease ipsi- and/or contralaterally, when comparing sham-operated and mTBI rats or hemispheres within

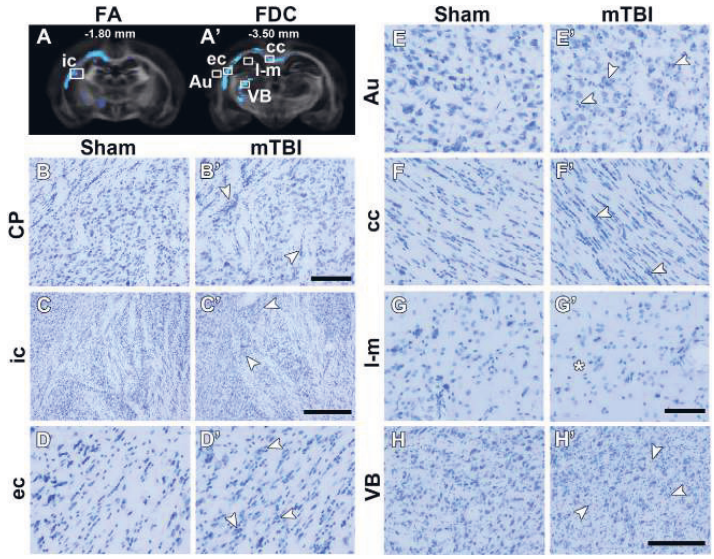

FIGURE 3 | FA **(A)** and FDC **(A')** at –1.80 and –3.50 mm from bregma, respectively, from the group analyses. White squares indicate the location of the photomicrographs shown in **(B–H)**. Representative photomicrographs of Nissl-stained sections of a sham-operated and a mTBI rat from the caudate putamen **(B,B')** from –0.90 mm (not shown in **A**), internal capsule **(C,C')** from –1.80 mm, and external capsule **(D,D')**, auditory cortex **(E,E')**, corpus callosum **(F,F')**, stratum-lacunosum moleculare **(G,G')**, and ventrobasal complex **(H,H')** from –3.50 mm from bregma. White arrowheads point at gliosis alterations associated with axonal damage and asterisk indicates less cell density. CD values of these two animals shown in this figure are shown in **Supplementary Table 1**. Au, auditory cortex; cc, corpus callosum; CP, caudate putamen; ec, external capsule; ic, internal capsule; l-m, stratum-lacunosum moleculare; VB, ventrobasal complex. Scale bars: 50 μm **(B,B',D,D'–G,G')**, 150 μm **(H,H')**, and 250 μm **(C,C')**.

mTBI rats (**Figure 5B**). FD, FC, and FDC showed decreased values ipsilaterally in almost all the brain areas in mTBI rats; specially in those at the level of the epicenter of the primary lesion at −3.50 mm (**Figures 5C–E**). Also, a decrease was obtained ipsilaterally in the sham-operated animals, such as in FD and FDC in the external capsule (**Figures 5C,E**) or in FC in the internal capsule (**Figure 5D**).

We found significant increases in ODI values in the corpus callosum, external capsule and internal capsule at −3.50 mm (**Figure 6A**). FWF showed a significant increase in the internal capsule, when comparing when comparing ipsi- and contralateral hemispheres in mTBI rats, and also in the sham-operated rats in the corpus callosum, external and internal capsule (**Figure 6B**). NDI showed an increase in the corpus callosum at −3.50 mm, and a decrease in the internal capsule when comparing ipsi- and contralateral hemispheres in mTBI rats (**Figure 6C**).

Histological analysis showed that anisotropy index significantly decreased in the external and internal capsule at −3.50 mm (**Figure 7A**), where we found increased cellularity (**Figure 7B**).

Table 1 shows the correlation results when comparing MRI and histology metrics from the ROI analyses. In the corpus callosum at −3.50 mm, AI showed a negative correlation with RD ($R = -0.544$; $q = 0.014$) (**Supplementary Figure 1A**). In the external capsule, we found that cellularity correlated positively with RD ($R = 0.474$; $q = 0.044$) at −1.80 mm from bregma (**Supplementary Figure 1B**). At −3.50 mm, the external capsule showed the most robust correlations. AI positively correlated with FA ($R = 0.737$; $q = 9.623 \times 10^{-5}$), peak FOD amplitude ($R = 0.781$; $q = 1.558 \times 10^{-5}$), FD ($R = 0.473$; $q = 0.044$), and FDC ($R = 0.492$; $q = 0.034$), and negatively with ODI ($R = -0.753$; $q = 4.780 \times 10^{-5}$) (**Supplementary Figures 1C,E,G,I,K**). Also, cell density correlated negatively with FA ($R = -0.712$; $q = 2.235 \times 10^{-4}$), peak FOD amplitude ($R = -0.695$; $q = 3.656 \times 10^{-4}$), FD ($R = -0.491$; $q = 0.034$) and FDC ($R = -0.505$; $q = 0.027$), and positively with ODI ($R = 0.709$; $q = 2.100 \times 10^{-4}$) (**Supplementary Figures 1D,F,H,J,L**). The internal capsule showed correlations between CD and FD ($R = -0.571$; $q = 0.008$), and FDC ($R = -0.580$; $q = 0.007$) (**Supplementary Figures 1M,N**). The ventrobasal complex showed a negative correlation between CD and FC ($R = -0.467$; $q = 0.048$) (**Supplementary Figure 1O**).

DISCUSSION

In this study, we used DTI, FBA, and NODDI to investigate microstructural changes in the mildly injured brain *ex vivo*. Whole-brain analyses revealed significant differences throughout the rat brain when comparing sham-operated and mTBI brains. FA, FD, and FDC showed a similar pattern of microstructural changes in the brain in the voxel-based analysis; however,

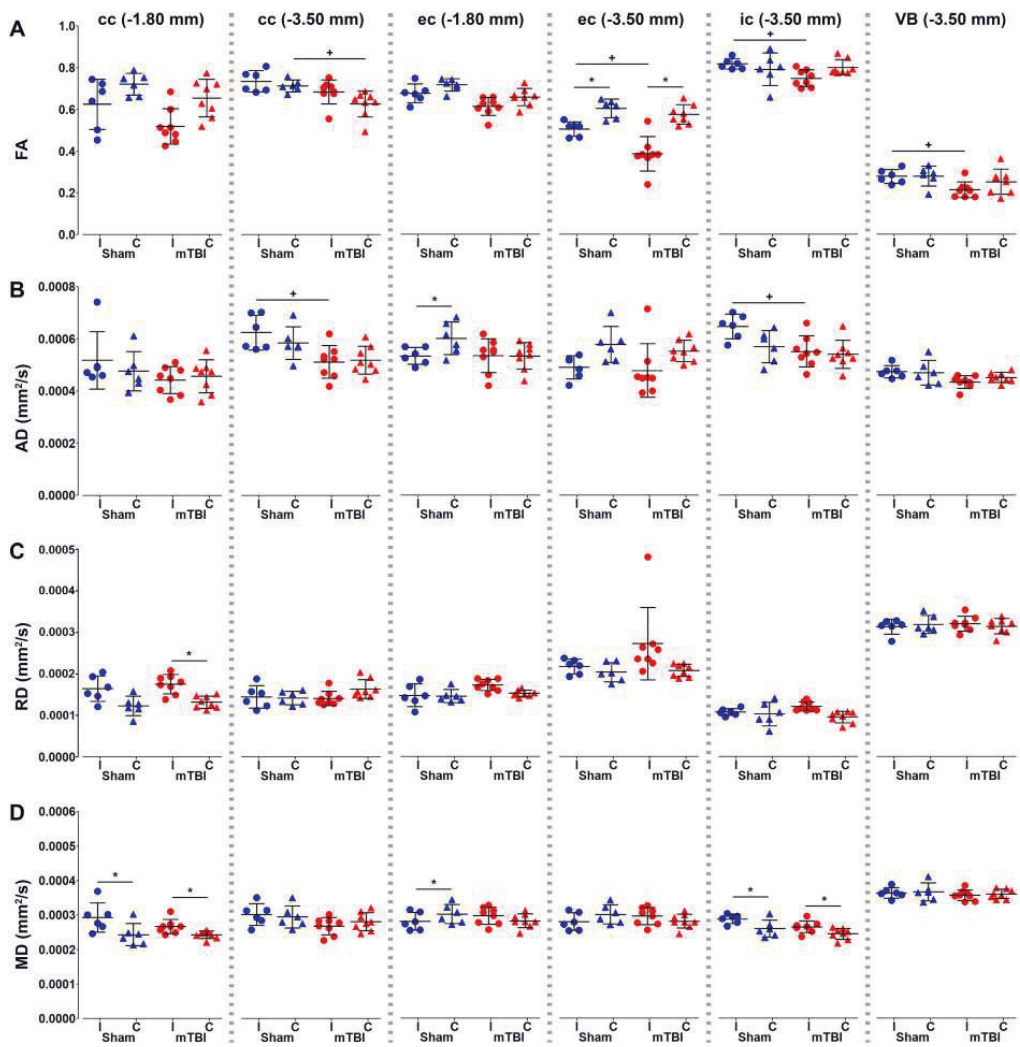

FIGURE 4 | Diffusion tensor imaging (DTI) metrics, fractional anisotropy **(A)**, and axial **(B)**, radial **(C)**, and mean **(D)** diffusivities, were analyzed in the corpus callosum and external capsule at –1.80 and –3.50 mm, and the internal capsule and ventrobasal complex at –3.50 mm from bregma. Sham-operated animals are indicated in blue and mTBI in red, while ipsi- and contralateral hemispheres are represented by circles and triangles, respectively. Results are shown as mean and standard deviation, and paired (*) *t*-test comparing ipsi- and contralateral sides within animals ($^{*}q < 0.05$) or unpaired (+) *t*-test comparing the same hemisphere between sham-operated and mTBI rats ($^{+}q < 0.05$), both FDR-corrected. AD, axial diffusivity; cc, corpus callosum; ec, external capsule; FA, fractional anisotropy; MD, mean diffusivity; RD, radial diffusivity; ic, internal capsule; VB, ventrobasal complex.

FBA metrics showed more significant fixels in white matter, FA also detected changes in gray matter, while ODI mainly detected areas closest to the primary lesion. Myelin- and Nissl-stained sections of the same brains revealed axonal alterations and increased cellularity in white and gray matter areas. Quantitative histological analyses of selected brain areas revealed that alterations in myelinated axons and increased cellularity correlated to changes in MRI metrics after mTBI.

Our study demonstrates that DTI provides a good sensitivity to detect microstructural-associated changes associated to mTBI in both white and gray matter (Bennett et al., 2012; Hylin et al., 2013; Stemper et al., 2015; Herrera et al., 2017; Hutchinson et al., 2018). Previous studies demonstrated the presence of axonal damage and increased cellularity due to gliosis using histology analysis (Mac Donald et al., 2007a,b; Hylin et al., 2013; San Martín Molina et al., 2020). More specifically, decreased

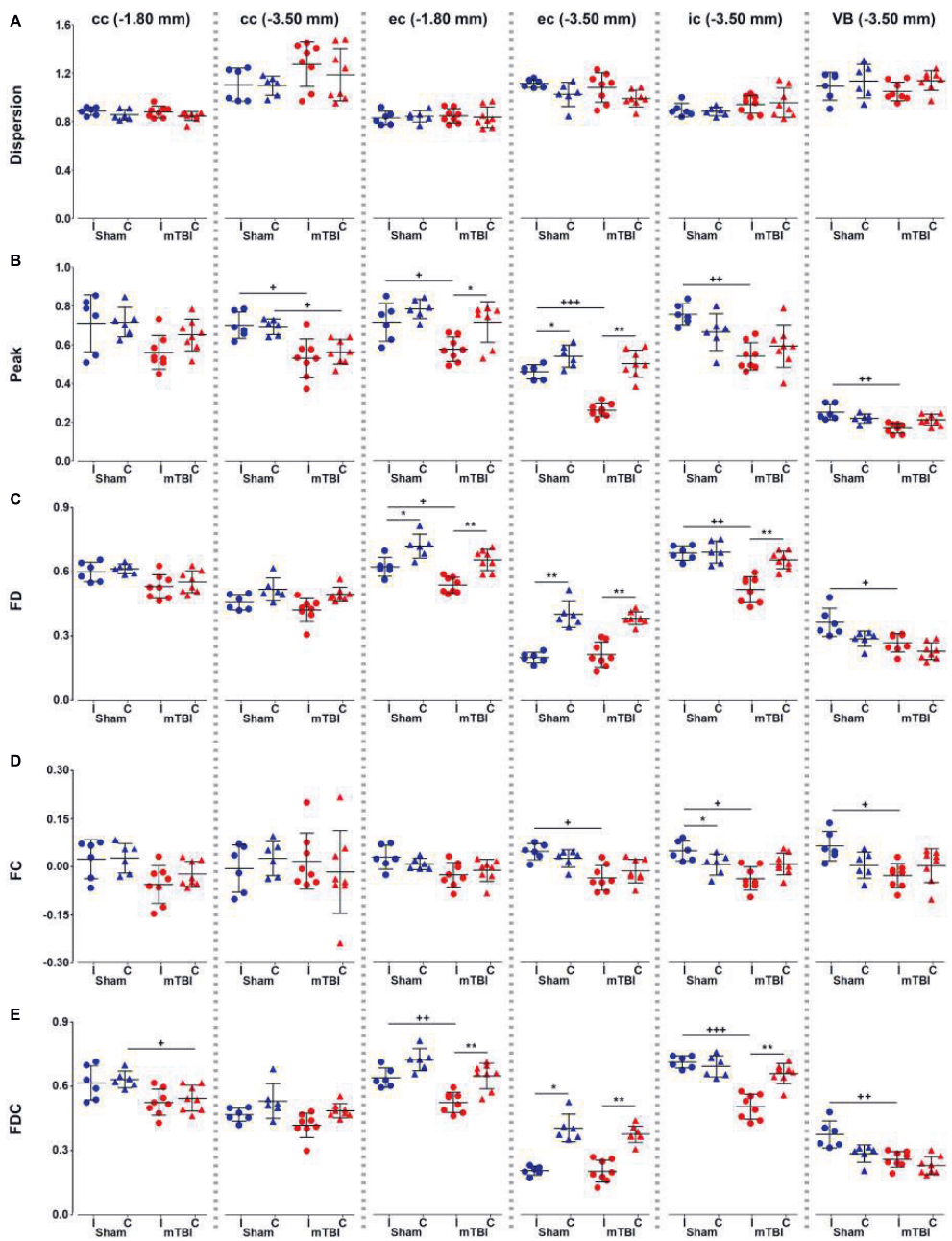

FIGURE 5 | Fixel-based metrics, dispersion **(A)**, peak FOD amplitudes **(B)**, FD **(C)**, FC **(D)**, and FDC **(E)**, were analyzed in the corpus callosum and external capsule at –1.80 and –3.50 mm, and the internal capsule and ventrobasal complex at –3.50 mm from bregma. Sham-operated animals are indicated in blue and mTBI in red, while ipsi- and contralateral hemispheres are represented by circles and triangles, respectively. Results are shown as mean and standard deviation, and paired (*) *t*-test comparing ipsi- and contralateral sides within animals (*$q < 0.05$, **$q < 0.01$) or unpaired (+) *t*-test comparing the same hemisphere between sham-operated and mTBI rats ($^{+}q < 0.05$, $^{++}q < 0.01$, $^{+++}q < 0.001$), both FDR-corrected. cc, corpus callosum; ec, external capsule; FC, fiber bundle cross-section; FD, fiber density; FDC, fiber density and fiber bundle cross-section; ic, internal capsule; VB, ventrobasal complex.

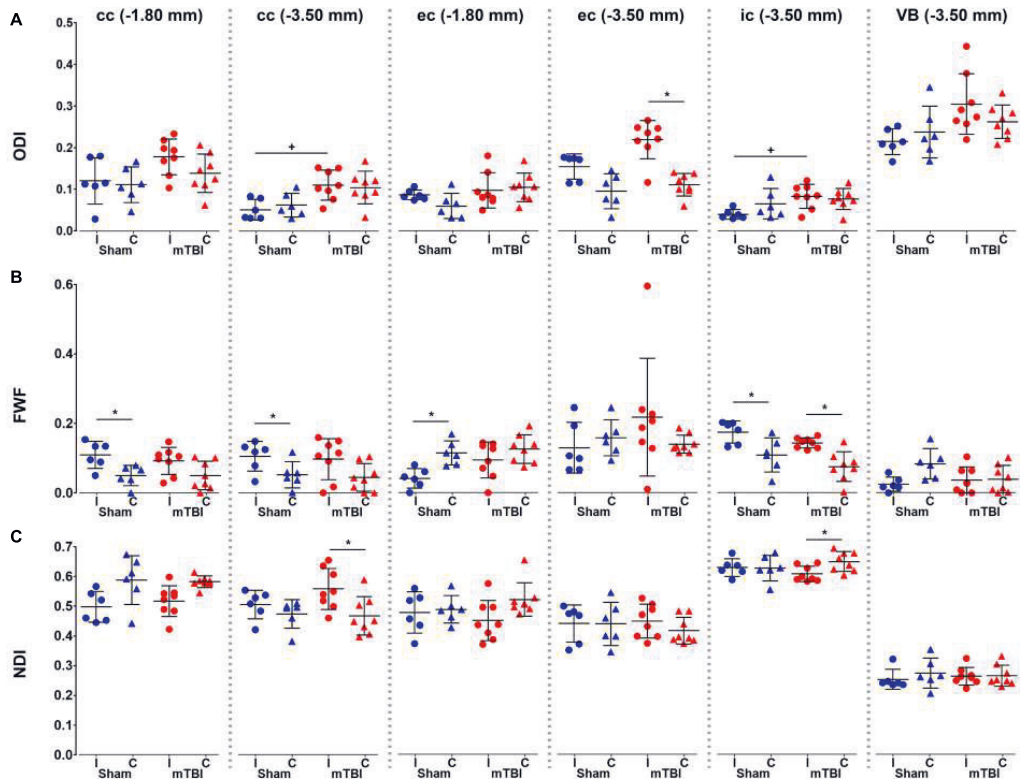

FIGURE 6 | NODDI metrics, ODI **(A)**, FWF **(B)**, and NDI **(C)**, were analyzed in the corpus callosum and external capsule at –1.80 and –3.50 mm, and the internal capsule and ventrobasal complex at –3.50 mm from bregma. Sham-operated animals are indicated in blue and mTBI in red, while ipsi- and contralateral hemispheres are represented by circles and triangles, respectively. Results are shown as mean and standard deviation, and paired (*) *t*-test comparing ipsi- and contralateral sides within animals (*$q < 0.05$) or unpaired (+) *t*-test comparing the same hemisphere between sham-operated and mTBI rats ($^{+}q < 0.05$), both FDR-corrected. cc, corpus callosum;ec, external capsule; ic, internal capsule; FWF, free water fraction; NDI, neurite density index; ODI, orientation dispersion index; VB, ventrobasal complex.

FA and AD due to axonal damage, and increased RD have been associated to gliosis. In our study, the positive association observed between FA, AD and AI in the corpus callosum and external capsule were indicative of axonal damage and/or axonal loss, while the negative association observed between FA and CD in the external capsule was associated to axonal damage in conjunction with a marked increase in cellularity. This was further indicated by the inverse relationship between RD and AI, and the positive association between RD and CD in both the corpus callosum and external capsule. With regards to CSD-derived metrics, the positive association observed in the external capsule between peak FOD amplitudes, FD and FD, and AI, and their negative relationship with CD, could be attributed a reduction in intact healthy fiber bundles and gliosis in those areas. Interestingly, the positive relationship observed between dispersion and AI in the ventrobasal complex was contrary to that observed in the white matter. As the ventrobasal complex is a region comprising of multiple fiber bundle populations; we hypothesize that the situation could result either from a reduction in densities of the primary fiber bundle or an increase in the densities of the secondary fibers (Riffert et al., 2014; Grazioplene et al., 2018). The NODDI analysis provided information of the microstructural compartment contributions, which has shown promising results in clinical research (Kamiya et al., 2020). Our voxel-based analysis only showed statistical differences in ODI in areas showing decreased FA, as suggested in previous studies (Jespersen et al., 2012; Zhang et al., 2012). Based on histology, we expected to also obtain differences in both NDI and FWF; however, it has been described that the reproducibility of NODDI in rat brain at 9.4 T was lower for FWF than ODI and NDI, which might require a considerably larger number of animals to observe biological changes in those parameters after mild TBI (McCunn et al., 2021).

Previous studies in animal models have shown the potential of DTI to detect the effect of mild injury in the brain. Wright et al. (2017) showed that FBA detected more voxels in the rat brain after severe injury than DTI *in vivo*. These authors found reduced FD predominantly in the ipsilateral corticospinal

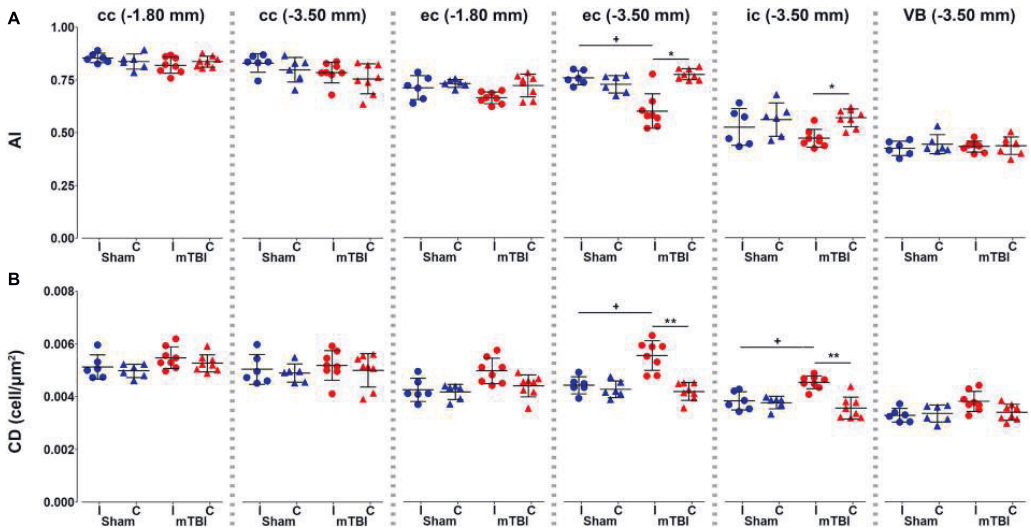

FIGURE 7 | Histology metrics, anisotropy index **(A)** and cellular density **(B)**, were analyzed in the corpus callosum and external capsule at –1.80 and –3.50 mm, and the internal capsule and ventrobasal complex at –3.50 mm from bregma. Sham-operated animals are indicated in blue and mTBI in red, while ipsi- and contralateral hemispheres are represented by circles and triangles, respectively. Results are shown as mean and standard deviation, and paired (*) *t*-test comparing ipsi- and contralateral sides within animals (*$q < 0.05$, **$q < 0.01$) or unpaired (+) *t*-test comparing the same hemisphere between sham-operated and mTBI rats (+$q < 0.05$), both FDR-corrected. AI, anisotropy index; cc, corpus callosum; CD, cellular density; ec, external capsule; ic, internal capsule; VB, ventrobasal complex.

tract, external capsule, fimbria, and corpus callosum, which also extended along the corpus callosum from the ipsilateral to contralateral hemisphere after severe TBI in rats. Additionally, these authors performed track-weighted imaging measurements revealing significantly fewer streamlines, shorter and straighter trajectories in the ipsilateral corpus callosum, fimbria, and internal capsule in TBI rats as compared to sham-operated ones. In accordance with our study, fixel-based metrics showed more significant voxels in the white matter as compared to FA. However, FA showed more significant voxels in the gray matter as compared to fixel-based metrics. Our results indicate that fixel- and DTI-based analyses may offer complementary information of tissue changes after mTBI as already shown in a previous study on adolescents with moderate-to-severe TBI (Verhelst et al., 2019). Our study also showed that ODI mainly detected changes in areas closed to the primary lesion. NODDI has demonstrated to be sensitive to early acute microstructural changes following a single closed head controlled cortical impact in rats, not detectable by DTI (McCunn et al., 2021). Another study using a closed-skull impact in mice showed greater sensitivity using NODDI than DTI to microstructural changes in white matter associated to astrocyte and microglia (Gazdzinski et al., 2020). Human studies suggested that the combination of DTI and NODDI significantly enhances our understanding of white matter microstructural alterations in subacute and chronic TBI (Muller et al., 2021; Oehr et al., 2021). In summary, our study suggests that the combination of dMRI parameters may provide more complete information of changes in tissue microstructure after brain injury, and therefore, an evaluation including different approaches could provide better understanding of the tissue damage after brain injury.

Different sensitivity of DTI- and fixel-based analyses could potentially result from poor fixel correspondence in complex brain areas, such as crossing fibers or gray matter, thereby resulting in large intra-group variances. Conventional DTI studies are typically based on lower diffusion weightings resulting in decreased angular contrast (Soares et al., 2013). The FBA framework, which is conditionally valid in the high *b*-value regime ($\geq$3,000 s/mm^2) (Raffelt et al., 2012; Genc et al., 2020), provides an improved resolution of crossing fiber bundle populations (Tournier et al., 2013). As, the diffusion-weighted signal originating from a restricted compartment is nearly fully preserved (Hall and Alexander, 2006; Yeh et al., 2010), and high *b*-values attenuate the signal from the extracellular water, the diffusion-weighted signal which is assumed to be restricted in the radial direction (Stanisz et al., 1997; Assaf and Basser, 2005; Alexander, 2008; Assaf et al., 2008; Barazany et al., 2009; Alexander et al., 2010) corresponds to the intra-axonal water-content (Raffelt et al., 2012). Moreover, as the FOD amplitude is relatively equal to the total radial diffusion-weighted signal, it provides an approximate measure of the intra-axonal volume of the corresponding fiber bundle (Raffelt et al., 2012). Therefore, the estimated FD metric is largely derived from the anisotropic WM component of the diffusion MRI signal and, is thereby highly specific to changes in axonal density (Tournier et al., 2004, 2007; Raffelt et al., 2012). Moreover, we also demonstrated the use of CSD-derived metrics for providing

a better understanding of the tissue-specific sources underlying the microstructural alterations post mTBI. Our findings were consistent with previous literature, as changes in conventional DTI-based metrics can be influenced by several pathological events, not just decreased density, such as axonal injury, gliosis, edema, or increased membrane permeability (Mac Donald et al., 2007a; Budde et al., 2011; Bennett et al., 2012; Salo et al., 2017). Future studies may benefit by the incorporation of signal fractions representative of tissue-specific microstructure (Khan et al., 2020; Mito et al., 2020). It is worth mentioning that advanced methodologies come at the cost of more complex data processing; however, these methods can provide more specific information on tissue microstructure and pathological alterations in the context of brain diseases, disorders, and injuries, and specially with a more comprehensive histological validation.

We used higher *b*-value than typically used *in vivo*, as it has been shown that diffusivity values *ex vivo* are decreased 2-3-fold as compared to *in vivo* due to changes in (1) temperature and (2) tissue microstructural properties following chemical fixation (Sun et al., 2003; Rane and Duong, 2011; Wu et al., 2013; Wang et al., 2018). As opposed to *in vivo* conditions, wherein the extra-axonal water signal attenuates with increasing *b*-value, the presence of immobile water confined in bodies of glial cells and other minute compartments such as vesicles, has been postulated in the extra-axonal space *ex vivo* (Stanisz et al., 1997; Veraart et al., 2019). Therefore, despite studies using high *b*-values enable a more direct comparison with *in vivo* results, further *in vivo* studies of mTBI using advanced dMRI are needed to provide more insights into the potential of these imaging methods (Wright et al., 2017; San Martín Molina et al., 2020; Pham et al., 2021).

While we have used CFE to correct for multiple comparisons, CFE applies on each measure separately that may give rise to false positives over the nominal alpha-threshold due to testing several parameters per a fixel or a voxel (Smith et al., 2021). However, given the complexity of CFE correction, it is challenging to decide what is the best approach to strike balance between Type I and Type II errors in the analysis. As a mitigation approach in this work, we used histology to verify the findings of DTI, FBA, and NODDI analyses. We also note that the statistically significant differences in the maps were in locations where we would expect to see differences based on previous experiments on how the tissue damage expands from the cortical primary lesion to connected areas as secondary damage. We used FWE correction

TABLE 1 | Coefficient (R) and *q*-values (q) from the Pearson's correlations between dMRI and histological metrics.

		cc (−1.80 mm)		cc (−3.50 mm)		ec (−1.80 mm)		ec (−3.50 mm)		ic (−3.50 mm)		VB (−3.50 mm)	
		AI	**CD**	**AI**	**CD**	**AI**	**CD**	**AI**	**CD**	**AI**	**CD**	**AI**	**CD**
FA	***R***	0.086	−0.061	0.429	−0.016	0.237	−0.333	**0.737**	**−0.712**	0.013	−0.344	0.045	−0.333
	q	0.809	0.877	0.075	0.961	0.401	0.187	**9.623×10^{-5}*****	**2.235×10^{-4}*****	0.962	0.172	0.915	0.187
AD	***R***	0.156	0.166	0.018	−0.165	0.026	0.051	0.436	−0.357	−0.033	−0.098	0.350	−0.348
	q	0.643	0.616	0.961	0.621	0.951	0.898	0.070	0.154	0.926	0.775	0.164	0.166
RD	***R***	−0.017	0.150	**−0.544**	−0.040	−0.228	**0.474**	−0.410	0.434	−0.076	0.347	0.188	0.119
	q	0.961	0.660	**0.014***	0.924	0.426	**0.044***	0.093	0.071	0.835	0.168	0.554	0.738
MD	***R***	0.199	0.258	−0.251	−0.167	−0.121	0.282	−0.040	0.086	−0.099	0.057	0.360	−0.057
	q	0.523	0.350	0.367	0.616	0.735	0.287	0.924	0.809	0.775	0.882	0.149	0.882
Disp	***R***	0.039	0.153	−0.248	−0.058	−0.082	−0.172	−0.175	0.049	−0.055	−0.115	0.459	−0.026
	q	0.926	0.651	0.373	0.882	0.818	0.603	0.591	0.903	0.887	0.744	0.053	0.951
Peak	***R***	0.151	0.079	0.329	0.036	0.231	−0.181	**0.781**	**−0.695**	0.072	−0.189	0.193	−0.383
	q	0.657	0.829	0.193	0.926	0.417	0.573	**1.558×10^{-5}*****	**3.656×10^{-4}*****	0.846	0.551	0.540	0.123
FD	***R***	0.084	−0.089	0.105	−0.122	0.257	−0.423	**0.473**	**−0.491**	0.443	**−0.571**	0.038	−0.302
	q	0.813	0.805	0.768	0.734	0.354	0.081	**0.044***	**0.034***	0.066	**0.008****	0.926	0.248
FC	***R***	0.102	−0.277	−0.125	−0.461	0.149	−0.147	0.324	−0.261	0.125	−0.416	0.103	**−0.467**
	q	0.770	0.299	0.725	0.051	0.660	0.660	0.201	0.342	0.725	0.087	0.769	**0.048***
FDC	***R***	0.093	−0.103	0.177	−0.139	0.266	−0.413	**0.492**	**−0.505**	0.419	**−0.580**	0.018	−0.374
	q	0.792	0.769	0.588	0.687	0.330	0.090	**0.034***	**0.027***	0.084	**0.007****	0.961	0.133
ODI	***R***	−0.167	−0.001	−0.089	0.190	-3.290×10^{-4}	−0.042	**−0.753**	**0.709**	0.028	0.200	−0.150	0.434
	q	0.598	0.997	0.791	0.537	0.999	0.912	**4.780×10^{-5}*****	**2.100×10^{-4}*****	0.947	0.515	0.633	0.071
FWF	***R***	0.355	0.416	0.161	0.190	0.103	0.026	−0.321	0.371	−0.202	0.209	0.313	0.148
	q	0.160	0.088	0.611	0.537	0.761	0.948	0.215	0.138	0.511	0.490	0.230	0.635
NDI	***R***	0.002	−0.078	0.435	0.301	0.218	−0.421	−0.230	0.292	0.030	−0.308	−0.164	0.095
	q	0.995	0.818	0.071	0.255	0.462	0.083	0.425	0.272	0.941	0.243	0.603	0.775

*Numbers in bold indicate the correlations significantly different from zero: *q < 0.05; **q < 0.01; ***q < 0.001. AD, axial diffusivity; AI, anisotropy index; cc, corpus callosum; CD, cellular density; Disp, dispersion; ec, external capsule; FA, fractional anisotropy; FC, fiber bundle cross-section; FD, fiber density; FDC, fiber density and fiber bundle cross-section; FWF, free water fraction; ic, internal capsule; MD, mean diffusivity; NDI, neurite density index; ODI, orientation dispersion index; RD, radial diffusivity; VB, ventrobasal complex.*

when performing (potentially highly correlated) voxel- and fixel-based analyses as there exist a potentially large number of false positives that arise with data-informed clustering, such as TFCE. However, in the ROI-based analysis, where the ROIs were defined based on the brain anatomy, we used FDR that is more liberal than FWE. Our reason for using FDR with ROIs is that it controls the number of false positives effectively, while simultaneously having a considerably lower number of false negatives than FWE. This balancing act, in turn, may lead to better reproducibility than strict control for false positives as argued by Geerligs and Maris (2021).

Our study included animals in the subacute stage, 35 days after the injury, which were subset of our previous *in vivo* study (San Martín Molina et al., 2020). This subgroup of animals showed, at day 3, hyperintensity associated to edema in the somatosensory cortex on *in vivo* T2-weighted images in four out of eight mTBI rats and hypointensity related to parenchymal bleeding in one of these four rats. After 28 days, three out of eight rats showed persistent but less pronounced cortical edema as compared to the acute time point, even two out of those three rats still showed signs of bleeding. The complex cortical patterns at the level of the primary injury associated to the secondary injury, and more importantly, to pathological outcomes warrant future studies. Despite of cortical damage in T2-weighted MRI, all the animals presented a consistent pattern of secondary tissue damage throughout the brain based on histology. Although the dura of the sham-operated and mTBI animals remained intact and no brain tissue damage was inflicted during the craniotomy, differences between ipsi- and contralateral hemispheres in sham-operated animals were reported. Histologically, the sham-operated rats did not present any tissue damage or cellular alteration. However, the sham-operation involving craniotomy might cause effects, e.g., swelling, that could affect the measurements at acute and/or subacute stages. Future studies should consider including a group of naïve rats to discern between minor sham-operation alterations and tissue damage associated to the injury.

Human histopathological studies are very scarce, and the low mortality after mTBI does not allow histopathological examination to correlate with MRI experiments in mTBI patients. Preclinical experiments including histology provide an opportunity to understand the mTBI pathogenesis (Bennett et al., 2012; Hylin et al., 2013; Stemper et al., 2015; Haber et al., 2017; Yu et al., 2017; San Martín Molina et al., 2020; Sinke et al., 2021). In our study, there were axonal alterations observed in all the areas highlighted in dMRI analyses, which were consistent across all the mTBI animals. These findings demonstrate that significant differences between sham-operated and mTBI rats in dMRI analyses reflected ongoing microstructural alterations after injury.

CONCLUSION

This study reveals the potential of the dMRI framework to detect microstructural alterations when comparing sham-operated and rats post mTBI. The combination of dMRI-based analyses could provide a more complete insight into the detection of microstructural alterations in white and gray matter after mild injuries. Advanced methodologies in combination with histopathological characterization of the same subjects can open new avenues into the improvement of our understanding of dMRI, which can directly enhance the diagnosis and prognosis of the mildly injured brain.

DATA AVAILABILITY STATEMENT

The raw data supporting the conclusions of this article will be made available by the authors, without undue reservation.

ETHICS STATEMENT

The animal study was reviewed and approved by the Animal Ethics Committee of the Provincial Government of Southern Finland and in accordance with the guidelines of the European Community Council Directives 86/609/EREC.

AUTHOR CONTRIBUTIONS

KC, OG, and AS contributed to study concept and design. KC, ON, RS, IS, JT, and MA contributed to data acquisition and analyses. All authors contributed to interpretation of the data, drafting, and reviewing the manuscript, and provided final approval for publication.

FUNDING

This work was supported by the Academy of Finland (AS #275453, #284544, #312686, and #323385; JT #316258 and OG #298007) and National Institutes of Health (MA R21NS096249 and R01AG057991).

ACKNOWLEDGMENTS

The authors would like to thank Maarit Pulkkinen for her help with the animal handling and Alonso Ramírez for his helpful comments and suggestions on the manuscript.

SUPPLEMENTARY MATERIAL

The Supplementary Material for this article can be found online at: https://www.frontiersin.org/articles/10.3389/fnins.2021.746214/full#supplementary-material

Supplementary Figure 1 | Pearson's correlations between dMRI and histological metrics statistically significant in **Table 1**, for the corpus callosum **(A)**, external capsule **(B–L)**, internal capsule **(M,N)** and ventrobasal complex **(O)**. Sham-operated animals are indicated in blue and mTBI in red, while ipsi- and contralateral hemispheres are represented by circles and triangles, respectively. AI, anisotropy index; cc, corpus callosum; ec, external capsule; FA, fractional anisotropy; FD, fiber density; FDC, fiber density and fiber bundle cross-section; ic, internal capsule; ODI, orientation dispersion index; RD, radial diffusivity; VB, ventrobasal complex.

REFERENCES

Aggarwal, M., Mori, S., Shimogori, T., Blackshaw, S., and Zhang, J. (2010). Three-dimensional diffusion tensor microimaging for anatomical characterization of the mouse brain. *Magn. Reson. Med.* 64, 249–261. doi: 10.1002/mrm.22426

Alexander, D. C. (2008). A general framework for experiment design in diffusion MRI and its application in measuring direct tissue-microstructure features. *Magn. Reson. Med.* 60, 439–448. doi: 10.1002/mrm.21646

Alexander, D. C., Hubbard, P. L., Hall, M. G., Moore, E. A., Ptito, M., Parker, G. J. M., et al. (2010). Orientationally invariant indices of axon diameter and density from diffusion MRI. *Neuroimage* 52, 1374–1389. doi: 10.1016/j.neuroimage.2010.05.043

Asken, B. M., DeKosky, S. T., Clugston, J. R., Jaffee, M. S., and Bauer, R. M. (2018). Diffusion tensor imaging (DTI) findings in adult civilian, military, and sport-related mild traumatic brain injury (mTBI): a systematic critical review. *Brain Imaging Behav.* 12, 585–612. doi: 10.1007/s11682-017-9708-9

Assaf, Y., and Basser, P. J. (2005). Composite hindered and restricted model of diffusion (CHARMED) MR imaging of the human brain. *Neuroimage* 27, 48–58. doi: 10.1016/j.neuroimage.2005.03.042

Assaf, Y., Blumenfeld-Katzir, T., Yovel, Y., and Basser, P. J. (2008). AxCaliber: a method for measuring axon diameter distribution from diffusion MRI. *Magn. Reson. Med.* 59, 1347–1354. doi: 10.1002/mrm.21577

Avants, B. B., Tustison, N. J., Stauffer, M., Song, G., Wu, B., and Gee, J. C. (2014). The Insight ToolKit image registration framework. *Front. Neuroinform.* 8:44. doi: 10.3389/fninf.2014.00044

Barazany, D., Basser, P. J., and Assaf, Y. (2009). In vivo measurement of axon diameter distribution in the corpus callosum of rat brain. *Brain* 132, 1210–1220. doi: 10.1093/brain/awp042

Basser, P. J., Mattiello, J., and LeBihan, D. (1994). MR diffusion tensor spectroscopy and imaging. *Biophys. J.* 66, 259–267. doi: 10.1016/S0006-3495(94)80775-1

Benjamini, Y., and Hochberg, Y. (1995). Controlling the false discovery rate: a practical and powerful approach to multiple testing. *J. R. Stat. Soc. Ser. B* 57, 289–300. doi: 10.1111/j.2517-6161.1995.tb02031.x

Bennett, R. E., Mac Donald, C. L., and Brody, D. L. (2012). Diffusion tensor imaging detects axonal injury in a mouse model of repetitive closed-skull traumatic brain injury. *Neurosci. Lett.* 513, 160–165. doi: 10.1016/j.neulet.2012.02.024

Budde, M. D., Janes, L., Gold, E., Turtzo, L. C., and Frank, J. A. (2011). The contribution of gliosis to diffusion tensor anisotropy and tractography following traumatic brain injury: validation in the rat using Fourier analysis of stained tissue sections. *Brain* 134, 2248–2260. doi: 10.1093/brain/awr161

Chary, K., Nissi, M. J., Nykänen, O., Manninen, E., Rey, R. I., Shmueli, K., et al. (2021). Quantitative susceptibility mapping of the rat brain after traumatic brain injury. *NMR Biomed.* 34:e4438. doi: 10.1002/nbm.4438

Churchill, N. W., Caverzasi, E., Graham, S. J., Hutchison, M. G., and Schweizer, T. A. (2019). White matter during concussion recovery: comparing diffusion tensor imaging (DTI) and neurite orientation dispersion and density imaging (NODDI). *Hum. Brain Mapp.* 40, 1908–1918. doi: 10.1002/hbm.24500

Cole, W. R., and Bailie, J. M. (2016). "Neurocognitive and psychiatric symptoms following mild traumatic brain injury," in *Translational Research in Traumatic Brain Injury*, (Boca Raton, FL: CRC Press/Taylor & Francis Group), 379–394.

Cordero-Grande, L., Christiaens, D., Hutter, J., Price, A. N., and Hajnal, J. V. (2019). Complex diffusion-weighted image estimation via matrix recovery under general noise models. *Neuroimage* 200, 391–404. doi: 10.1016/j.neuroimage.2019.06.039

Dhollander, T., and Connelly, A. (2016). "A novel iterative approach to reap the benefits of multi-tissue CSD from just single-shell (+b=0) diffusion MRI data," in *Proceeding of the International Society of Magnetic Resonance in Medicine*, (Singapore), 3010–3010.

Duhaime, A. C., Gean, A. D., Haacke, E. M., Hicks, R., Wintermark, M., Mukherjee, P., et al. (2010). Common data elements in radiologic imaging of traumatic brain injury. *Arch. Phys. Med. Rehabil.* 91, 1661–1666. doi: 10.1016/j.apmr.2010.07.238

Gazdzinski, L. M., Mellerup, M., Wang, T., Adel, S. A. A., Lerch, J. P., Sled, J. G., et al. (2020). White matter changes caused by mild traumatic brain injury in mice evaluated using neurite orientation dispersion and density imaging. *J. Neurotrauma* 37, 1818–1828. doi: 10.1089/neu.2020.6992

Geerligs, L., and Maris, E. (2021). Improving the sensitivity of cluster-based statistics for functional magnetic resonance imaging data. *Hum. Brain Mapp.* 42, 2746–2765. doi: 10.1002/hbm.25399

Genc, S., Tax, C. M. W., Raven, E. P., Chamberland, M., Parker, G. D., and Jones, D. K. (2020). Impact of b-value on estimates of apparent fibre density. *Hum. Brain Mapp.* 41, 2583–2595. doi: 10.1002/hbm.24964

Grazioplene, R. G., Bearden, C. E., Subotnik, K. L., Ventura, J., Haut, K., Nuechterlein, K. H., et al. (2018). Connectivity-enhanced diffusion analysis reveals white matter density disruptions in first episode and chronic schizophrenia. *NeuroImage Clin.* 18, 608–616. doi: 10.1016/j.nicl.2018.02.015

Haber, M., Hutchinson, E. B., Sadeghi, N., Cheng, W. H., Namjoshi, D., Cripton, P., et al. (2017). Defining an analytic framework to evaluate quantitative MRI markers of traumatic axonal injury: preliminary results in a mouse closed head injury model. *eNeuro* 4, ENEURO.164–ENEURO.117. doi: 10.1523/ENEURO.0164-17.2017

Hall, M. G., and Alexander, D. C. (2006). Finite pulse widths improve fibre orientation estimates in diffusion tensor MRI. *Proc. Intl. Soc. Mag. Reson. Med.* 1076–1076.

Herrera, J. J., Bockhorst, K., Kondraganti, S., Stertz, L., Quevedo, J., and Narayana, P. A. (2017). Acute white matter tract damage after frontal mild traumatic brain injury. *J. Neurotrauma* 34, 291–299. doi: 10.1089/neu.2016.4407

Hughes, D. G., Jackson, A., Mason, D. L., Berry, E., Hollis, S., and Yates, D. W. (2004). Abnormalities on magnetic resonance imaging seen acutely following mild traumatic brain injury: correlation with neuropsychological tests and delayed recovery. *Neuroradiology* 46, 550–558. doi: 10.1007/s00234-004-1227-x

Hutchinson, E. B., Schwerin, S. C., Radomski, K. L., Sadeghi, N., Komlosh, M. E., Irfanoglu, M. O., et al. (2018). Detection and distinction of mild brain injury effects in a ferret model using diffusion tensor MRI (DTI) and DTI-driven tensor-based morphometry (D-TBM). *Front. Neurosci.* 12:573. doi: 10.3389/fnins.2018.00573

Hylin, M. J., Orsi, S. A., Zhao, J., Bockhorst, K., Perez, A., Moore, A. N., et al. (2013). Behavioral and histopathological alterations resulting from mild fluid percussion injury. *J. Neurotrauma* 30, 702–715. doi: 10.1089/neu.2012.2630

Inglese, M., Makani, S., Johnson, G., Cohen, B. A., Silver, J. A., Gonen, O., et al. (2005). Diffuse axonal injury in mild traumatic brain injury: a diffusion tensor imaging study. *J. Neurosurg.* 103, 298–303. doi: 10.3171/jns.2005.103.2.0298

Iverson, G. L., Lovell, M. R., Smith, S., and Franzen, M. D. (2000). Prevalence of abnormal CT-scans following mild head injury. *Brain Inj.* 14, 1057–1061. doi: 10.1080/02699050050203559

Jansons, K. M., and Alexander, D. C. (2003). Persistent angular structure: new insights from diffusion MRI data. Dummy version. *Inf. Process Med. Imaging* 18, 672–683. doi: 10.1007/978-3-540-45087-0_56

Jespersen, S. N., Leigland, L. A., Cornea, A., and Kroenke, C. D. (2012). Determination of axonal and dendritic orientation distributions within the developing cerebral cortex by diffusion tensor imaging. *IEEE Trans. Med. Imaging* 31, 16–32. doi: 10.1109/TMI.2011.2162099

Jeurissen, B., Leemans, A., Tournier, J. D., Jones, D. K., and Sijbers, J. (2013). Investigating the prevalence of complex fiber configurations in white matter tissue with diffusion magnetic resonance imaging. *Hum. Brain Mapp.* 34, 2747–2766. doi: 10.1002/hbm.22099

Jeurissen, B., Tournier, J. D., Dhollander, T., Connelly, A., and Sijbers, J. (2014). Multi-tissue constrained spherical deconvolution for improved analysis of multi-shell diffusion MRI data. *Neuroimage* 103, 411–426. doi: 10.1016/j.neuroimage.2014.07.061

Jones, D. K., Knösche, T. R., and Turner, R. (2013). White matter integrity, fiber count, and other fallacies: the do's and don'ts of diffusion MRI. *Neuroimage* 73, 239–254. doi: 10.1016/j.neuroimage.2012.06.081

Kamiya, K., Hori, M., and Aoki, S. (2020). NODDI in clinical research. *J. Neurosci. Methods* 346:108908. doi: 10.1016/j.jneumeth.2020.108908

Katz, D. I., Cohen, S. I., and Alexander, M. P. (2015). "Mild traumatic brain injury," in *Handbook of Clinical Neurology*, eds J. Grafman and A. M. Salazar (Amsterdam: Elsevier), 131–156.

Kellner, E., Dhital, B., Kiselev, V. G., and Reisert, M. (2016). Gibbs-ringing artifact removal based on local subvoxel-shifts. *Magn. Reson. Med.* 76, 1574–1581. doi: 10.1002/mrm.26054

Khan, W., Egorova, N., Khlif, M. S., Mito, R., Dhollander, T., and Brodtmann, A. (2020). Three-tissue compositional analysis reveals in-vivo microstructural

heterogeneity of white matter hyperintensities following stroke. *Neuroimage* 218:116869. doi: 10.1016/j.neuroimage.2020.116869

Laitinen, T., Sierra, A., Pitkänen, A., and Gröhn, O. (2010). Diffusion tensor MRI of axonal plasticity in the rat hippocampus. *Neuroimage* 51, 521–530. doi: 10.1016/j.neuroimage.2010.02.077

Laitinen, T., Sierra López, A., Bolkvadze, T., Pitkänen, A., and Gröhn, O. (2015). Diffusion tensor imaging detects chronic microstructural changes in white and grey matter after traumatic brain injury in rat. *Front. Neurosci.* 9:128. doi: 10.3389/fnins.2015.00128

Ling, H., Hardy, J., and Zetterberg, H. (2015). Neurological consequences of traumatic brain injuries in sports. *Mol. Cell. Neurosci.* 66, 114–122. doi: 10.1016/j.mcn.2015.03.012

Mac Donald, C. L., Dikranian, K., Bayly, P., Holtzman, D., and Brody, D. (2007a). Diffusion tensor imaging reliably detects experimental traumatic axonal injury and indicates approximate time of injury. *J. Neurosci.* 27, 11869–11876. doi: 10.1523/JNEUROSCI.3647-07.2007

Mac Donald, C. L., Dikranian, K., Song, S. K., Bayly, P. V., Holtzman, D. M., and Brody, D. L. (2007b). Detection of traumatic axonal injury with diffusion tensor imaging in a mouse model of traumatic brain injury. *Exp. Neurol.* 205, 116–131. doi: 10.1016/j.expneurol.2007.01.035

McCunn, P., Xu, X., Moszczynski, A., Li, A., Brown, A., and Bartha, R. (2021). Neurite orientation dispersion and density imaging in a rodent model of acute mild traumatic brain injury. *J. Neuroimaging* 31, 879–892. doi: 10.1111/jon.12917

Mechtler, L. L., Shastri, K. K., and Crutchfield, K. E. (2014). Advanced neuroimaging of mild traumatic brain injury. *Neurol. Clin.* 32, 31–58. doi: 10.1016/j.ncl.2013.08.002

Mito, R., Dhollander, T., Xia, Y., Raffelt, D., Salvado, O., Churilov, L., et al. (2020). In vivo microstructural heterogeneity of white matter lesions in healthy elderly and Alzheimer's disease participants using tissue compositional analysis of diffusion MRI data. *NeuroImage Clin.* 28:102479. doi: 10.1016/j.nicl.2020.102479

Mittl, R. L., Grossman, R. I., Hiehle, J. F., Hurst, R. W., Kauder, D. R., Gennarelli, T. A., et al. (1994). Prevalence of MR evidence of diffuse axonal injury in patients with mild head injury and normal head CT findings. *AJNR. Am. J. Neuroradiol.* 15, 1583–1589.

Muller, J., Middleton, D., Alizadeh, M., Zabrecky, G., Wintering, N., Bazzan, A. J., et al. (2021). Hybrid diffusion imaging reveals altered white matter tract integrity and associations with symptoms and cognitive dysfunction in chronic traumatic brain injury. *NeuroImage Clin.* 30:102681. doi: 10.1016/j.nicl.2021.102681

Oehr, L. E., Yang, J. Y.-M., Chen, J., Maller, J. J., Seal, M. L., and Anderson, J. F. I. (2021). Investigating white matter tract microstructural changes at six–twelve weeks following mild traumatic brain injury: a combined diffusion tensor imaging and neurite orientation dispersion and density imaging study. *J. Neurotrauma* 38, 2255–2263. doi: 10.1089/neu.2020.7310

Palacios, E. M., Owen, J. P., Yuh, E. L., Wang, M. B., Vassar, M. J., Ferguson, A. R., et al. (2020). The evolution of white matter microstructural changes after mild traumatic brain injury: a longitudinal DTI and NODDI study. *Sci. Adv.* 6:eaaz6892. doi: 10.1126/sciadv.aaz6892

Pervez, M., Kitagawa, R. S., and Chang, T. R. (2018). Definition of traumatic brain injury, neurosurgery, trauma orthopedics, neuroimaging, psychology, and psychiatry in mild traumatic brain injury. *Neuroimaging Clin. N. Am.* 28, 1–13. doi: 10.1016/j.nic.2017.09.010

Pham, L., Wright, D. K., O'Brien, W. T., Bain, J., Huang, C., Sun, M., et al. (2021). Behavioral, axonal, and proteomic alterations following repeated mild traumatic brain injury: novel insights using a clinically relevant rat model. *Neurobiol. Dis.* 148:105151. doi: 10.1016/j.nbd.2020.105151

Raffelt, D., Tournier, J. D., Rose, S., Ridgway, G. R., Henderson, R., Crozier, S., et al. (2012). Apparent Fibre Density: a novel measure for the analysis of diffusion-weighted magnetic resonance images. *Neuroimage* 59, 3976–3994. doi: 10.1016/j.neuroimage.2011.10.045

Raffelt, D. A., Smith, R. E., Ridgway, G. R., Tournier, J. D., Vaughan, D. N., Rose, S., et al. (2015). Connectivity-based fixel enhancement: whole-brain statistical analysis of diffusion MRI measures in the presence of crossing fibres. *Neuroimage* 117, 40–55. doi: 10.1016/j.neuroimage.2015.05.039

Raffelt, D. A., Tournier, J. D., Smith, R. E., Vaughan, D. N., Jackson, G., Ridgway, G. R., et al. (2017). Investigating white matter fibre density and morphology using fixel-based analysis. *Neuroimage* 144, 58–73. doi: 10.1016/j.neuroimage.2016.09.029

Rane, S., and Duong, T. Q. (2011). Comparison of in vivo and ex vivo diffusion tensor imaging in rhesus macaques at short and long diffusion times. *Open Neuroimag J.* 5, 172–178. doi: 10.2174/1874440001105010172

Riffert, T. W., Schreiber, J., Anwander, A., and Knösche, T. R. (2014). Beyond fractional anisotropy: extraction of bundle-specific structural metrics from crossing fiber models. *Neuroimage* 100, 176–191. doi: 10.1016/j.neuroimage.2014.06.015

Salo, R. A., Miettinen, T., Laitinen, T., Gröhn, O., and Sierra, A. (2017). Diffusion tensor MRI shows progressive changes in the hippocampus and dentate gyrus after status epilepticus in rat – histological validation with Fourier-based analysis. *Neuroimage* 152, 221–236. doi: 10.1016/j.neuroimage.2017.03.003

San Martín Molina, I., Salo, R. A., Abdollahzadeh, A., Tohka, J., Gröhn, O., and Sierra, A. (2020). In vivo diffusion tensor imaging in acute and subacute phases of mild traumatic brain injury in rats. *eNeuro* 7, 1–18. doi: 10.1523/ENEURO.0476-19.2020

Scheid, R., Preul, C., Gruber, O., Wiggins, C., and Von Cramon, D. Y. (2003). Diffuse axonal injury associated with chronic traumatic brain injury: evidence from T2*-weighted Gradient-echo imaging at 3 T. *Am. J. Neuroradiol.* 24, 1049–1056.

Sinke, M. R. T., Otte, W. M., Meerwaldt, A. E., Franx, B. A. A., Ali, M. H. M., Rakib, F., et al. (2021). Imaging markers for the characterization of gray and white matter changes from acute to chronic stages after experimental traumatic brain injury. *J. Neurotrauma* 38, 1662–1669. doi: 10.1089/neu.2020.7151

Smith, R., Christiaens, D., Jeurissen, B., Pietsch, M., Vaughan, D., Jackson, G., et al. (2021). "On false positive control in Fixel-Based Analysis," in *Proceeding of the 27th International Society of Magnetic Resonance in Medicine ISMRM*, (Montréal), 4289.

Smith, R. E., Tournier, J. D., Calamante, F., and Connelly, A. (2013). SIFT: spherical-deconvolution informed filtering of tractograms. *Neuroimage* 67, 298–312. doi: 10.1016/j.neuroimage.2012.11.049

Smith, S. M., and Nichols, T. E. (2009). Threshold-free cluster enhancement: addressing problems of smoothing, threshold dependence and localisation in cluster inference. *Neuroimage* 44, 83–98. doi: 10.1016/j.neuroimage.2008.03.061

Soares, J. M., Marques, P., Alves, V., and Sousa, N. (2013). A hitchhiker's guide to diffusion tensor imaging. *Front. Neurosci.* 7:31. doi: 10.3389/fnins.2013.00031

Stanisz, G. J., Szafer, A., Wright, G. A., and Henkelman, R. M. (1997). An analytical model of restricted diffusion in bovine optic nerve. *Magn. Reson. Med.* 37, 103–111. doi: 10.1002/mrm.1910370115

Stemper, B. D., Shah, A. S., Pintar, F. A., McCrea, M., Kurpad, S. N., Glavaski-Joksimovic, A., et al. (2015). Head rotational acceleration characteristics influence behavioral and diffusion tensor imaging outcomes following concussion. *Ann. Biomed. Eng.* 43, 1071–1088. doi: 10.1007/s10439-014-1171-9

Sun, S. W., Neil, J. J., and Song, S. K. (2003). Relative indices of water diffusion anisotropy are equivalent in live and formalin-fixed mouse brains. *Magn. Reson. Med.* 50, 743–748. doi: 10.1002/mrm.10605

Tournier, J. D., Calamante, F., and Connelly, A. (2007). Robust determination of the fibre orientation distribution in diffusion MRI: non-negativity constrained super-resolved spherical deconvolution. *Neuroimage* 35, 1459–1472. doi: 10.1016/j.neuroimage.2007.02.016

Tournier, J. D., Calamante, F., and Connelly, A. (2013). Determination of the appropriate b value and number of gradient directions for high-angular-resolution diffusion-weighted imaging. *NMR Biomed.* 26, 1775–1786. doi: 10.1002/nbm.3017

Tournier, J. D., Calamante, F., Gadian, D. G., and Connelly, A. (2004). Direct estimation of the fiber orientation density function from diffusion-weighted MRI data using spherical deconvolution. *Neuroimage* 23, 1176–1185. doi: 10.1016/j.neuroimage.2004.07.037

Tournier, J. D., Smith, R., Raffelt, D., Tabbara, R., Dhollander, T., Pietsch, M., et al. (2019). MRtrix3: a fast, flexible and open software framework for medical image processing and visualisation. *Neuroimage* 202:116137. doi: 10.1016/j.neuroimage.2019.116137

Tuch, D. S. (2004). Q-ball imaging. *Magn. Reson. Med.* 52, 1358–1372. doi: 10.1002/mrm.20279

Tuch, D. S., Reese, T. G., Wiegell, M. R., Makris, N., Belliveau, J. W., and Van Wedeen, J. (2002). High angular resolution diffusion imaging reveals intravoxel white matter fiber heterogeneity. *Magn. Reson. Med.* 48, 577–582. doi: 10.1002/mrm.10268

Tustison, N. J., Avants, B. B., Cook, P. A., Zheng, Y., Egan, A., Yushkevich, P. A., et al. (2010). N4ITK: improved N3 bias correction. *IEEE Trans. Med. Imaging* 29, 1310–1320. doi: 10.1109/TMI.2010.2046908

van der Naalt, J., Timmerman, M. E., de Koning, M. E., van der Horn, H. J., Scheenen, M. E., Jacobs, B., et al. (2017). Early predictors of outcome after mild traumatic brain injury (UPFRONT): an observational cohort study. *Lancet Neurol.* 16, 532–540. doi: 10.1016/S1474-4422(17)30117-5

Veraart, J., Fieremans, E., and Novikov, D. S. (2019). On the scaling behavior of water diffusion in human brain white matter. *Neuroimage* 185, 379–387. doi: 10.1016/j.neuroimage.2018.09.075

Veraart, J., Sijbers, J., Sunaert, S., Leemans, A., and Jeurissen, B. (2013). Weighted linear least squares estimation of diffusion MRI parameters: strengths, limitations, and pitfalls. *Neuroimage* 81, 335–346. doi: 10.1016/j.neuroimage.2013.05.028

Verhelst, H., Giraldo, D., Vander Linden, C., Vingerhoets, G., Jeurissen, B., and Caeyenberghs, K. (2019). Cognitive training in young patients with traumatic brain injury: a fixel-based analysis. *Neurorehabil. Neural Repair* 33, 813–824. doi: 10.1177/1545968319868720

Wallace, E. J., Mathias, J. L., and Ward, L. (2018). The relationship between diffusion tensor imaging findings and cognitive outcomes following adult traumatic brain injury: a meta-analysis. *Neurosci. Biobehav. Rev.* 92, 93–103. doi: 10.1016/j.neubiorev.2018.05.023

Wallace, E. J., Mathias, J. L., Ward, L., Fripp, J., Rose, S., and Pannek, K. (2020). A fixel-based analysis of micro- and macro-structural changes to white matter following adult traumatic brain injury. *Hum. Brain Mapp.* 41, 2187–2197.

Wang, C., Song, L., Zhang, R., and Gao, F. (2018). Impact of fixation, coil, and number of excitations on diffusion tensor imaging of rat brains at 7.0 T. *Eur. Radiol. Exp.* 2:25. doi: 10.1186/s41747-018-0057-2

Wright, D. K., Johnston, L. A., Kershaw, J., Ordidge, R., O'Brien, T. J., and Shultz, S. R. (2017). Changes in apparent fiber density and track-weighted imaging metrics in white matter following experimental traumatic brain injury. *J. Neurotrauma* 34, 2109–2118. doi: 10.1089/neu.2016.4730

Wu, D., Xu, J., McMahon, M. T., van Zijl, P. C. M., Mori, S., Northington, F. J., et al. (2013). In vivo high-resolution diffusion tensor imaging of the mouse brain. *Neuroimage* 83, 18–26. doi: 10.1016/j.neuroimage.2013.06.012

Yeh, C. H., Tournier, J. D., Cho, K. H., Lin, C. P., Calamante, F., and Connelly, A. (2010). The effect of finite diffusion gradient pulse duration on fibre orientation estimation in diffusion MRI. *Neuroimage* 51, 743–751. doi: 10.1016/j.neuroimage.2010.02.041

Yin, B., Li, D. D., Huang, H., Gu, C. H., Bai, G. H., Hu, L. X., et al. (2019). Longitudinal changes in diffusion tensor imaging following mild traumatic brain injury and correlation with outcome. *Front. Neural Circuits* 13:28. doi: 10.3389/fncir.2019.00028

Yu, F., Shukla, D. K., Armstrong, R. C., Marion, C. M., Radomski, K. L., Selwyn, R. G., et al. (2017). Repetitive model of mild traumatic brain injury produces cortical abnormalities detectable by magnetic resonance diffusion imaging, histopathology, and behavior. *J. Neurotrauma* 34, 1364–1381. doi: 10.1089/neu.2016.4569

Yuh, E. L., Cooper, S. R., Mukherjee, P., Yue, J. K., Lingsma, H. F., Gordon, W. A., et al. (2014). Diffusion tensor imaging for outcome prediction in mild traumatic brain injury: a TRACK-TBI study. *J. Neurotrauma* 31, 1457–1477. doi: 10.1089/neu.2013.3171

Zhang, H., Schneider, T., Wheeler-Kingshott, C. A., and Alexander, D. C. (2012). NODDI: practical in vivo neurite orientation dispersion and density imaging of the human brain. *Neuroimage* 61, 1000–1016. doi: 10.1016/j.neuroimage.2012.03.072

Conflict of Interest: The authors declare that the research was conducted in the absence of any commercial or financial relationships that could be construed as a potential conflict of interest.

Publisher's Note: All claims expressed in this article are solely those of the authors and do not necessarily represent those of their affiliated organizations, or those of the publisher, the editors and the reviewers. Any product that may be evaluated in this article, or claim that may be made by its manufacturer, is not guaranteed or endorsed by the publisher.

Supplementary Material

Supplementary Table 1: Anisotropy index (AI) and cellular density (CD) values obtained from the histological analyses from the ipsilateral hemisphere of the sham-operated and mTBI animals shown in Figure 2 and 3, respectively.

	Animal	AI	CD
cc (-1.80 mm)	**Sham**	0.856	0.00597
	mTBI	0.814	0.00556
cc (-3.50 mm)	**Sham**	0.745	0.00544
	mTBI	0.783	0.00546
ec (-1.80 mm)	**Sham**	0.722	0.00409
	mTBI	0.621	0.00450
ec (-3.50 mm)	**Sham**	0.752	0.00492
	mTBI	0.649	0.00553
ic (-3.50 mm)	**Sham**	0.641	0.00384
	mTBI	0.425	0.00448
VB (-3.50 mm)	**Sham**	0.456	0.00301
	mTBI	0.444	0.00429

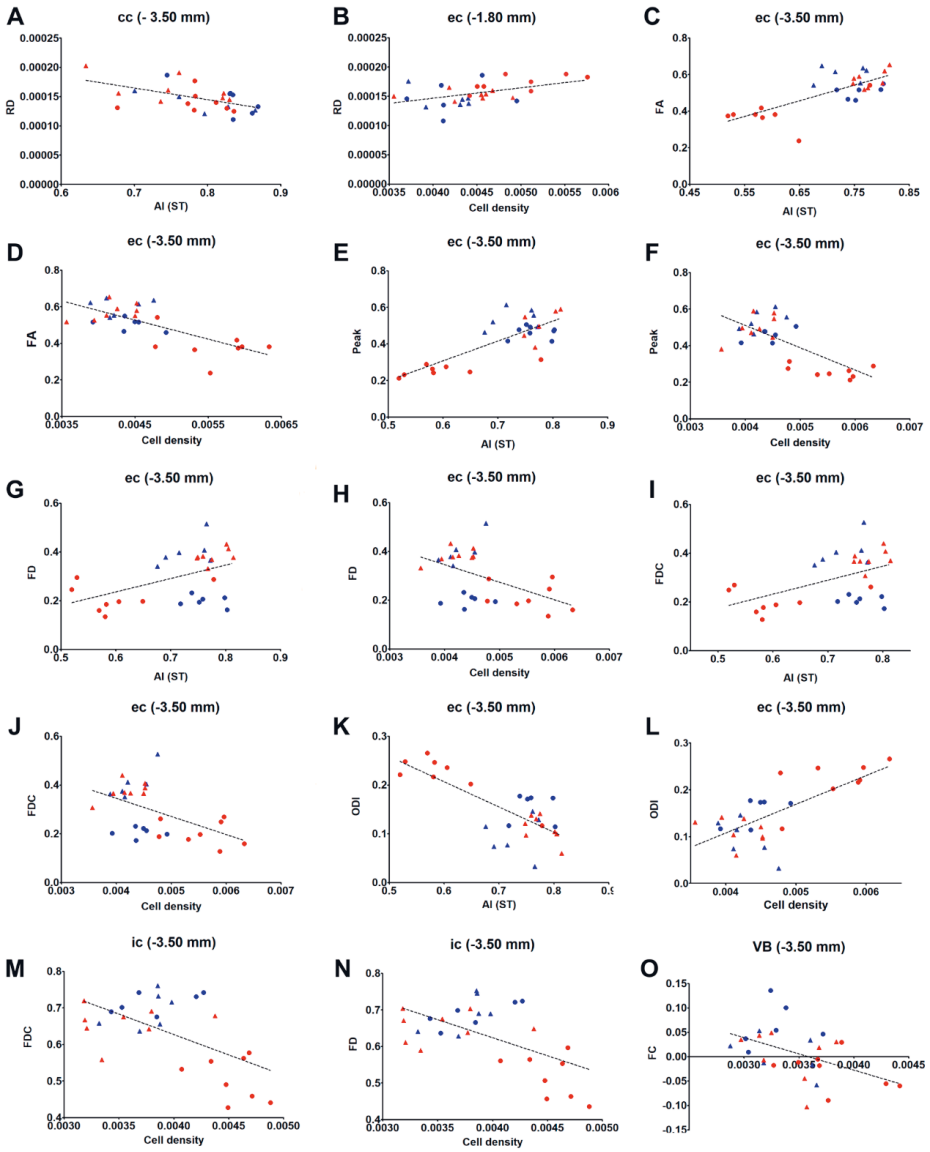

Supplementary Figure 1: Pearson's correlations between dMRI and histological metrics statistically significant in **Table 1**, for the corpus callosum **(A)**, external capsule **(B–L)**, internal capsule **(M,N)** and ventrobasal complex **(O)**. Sham-operated animals are indicated in blue and mTBI in red, while ipsi- and contralateral hemispheres are represented by circles and triangles, respectively. AI, anisotropy index; cc, corpus callosum; ec, external capsule; FA, fractional anisotropy; FD, fiber density; FDC, fiber density and fiber bundle cross-section; ic, internal capsule; ODI, orientation dispersion index; RD, radial diffusivity; VB, ventrobasal complex.

III

Diffusion MRI approaches for investigating microstructural complexity in a rat model of traumatic brain injury

Chary K, Manninen E, Claessens J, Ramirez-Manzanares A, Gröhn O and Sierra A

Submitted, 2022

KARTHIK SAMPATH KUMAR CHARY

Conventional quantitative MRI techniques often lack sensitivity or specificity for detecting complex secondary tissue changes after traumatic brain injury (TBI). Using an experimental TBI model, this thesis presents new knowledge on the potential of advanced quantitative MRI approaches for improved characterization of secondary tissue damage and disseminates the effectiveness and limitations of these quantitative MRI approaches.

UNIVERSITY OF
EASTERN FINLAND

uef.fi

**PUBLICATIONS OF
THE UNIVERSITY OF EASTERN FINLAND**
Dissertations in Health Sciences

ISBN 978-952-61-4738-3
ISSN 1798-5668